ALMA MATER STUDIORUM
UNIVERSITÀ DI BOLOGNA

DOTTORATO DI RICERCA IN

NANOSCIENZE PER LA MEDICINA E PER L'AMBIENTE

Ciclo 37

Settore Concorsuale: 03/A1 - CHIMICA ANALITICA

Settore Scientifico Disciplinare: CHIM/01 - CHIMICA ANALITICA

AF4 AS A PASSEPARTOUT TECHNIQUE FOR THE CHARACTERIZATION OF NANOSYSTEMS OF MEDICAL INTEREST

Presentata da: Stefano Giordani

Coordinatore Dottorato

Matteo Calvaresi

Supervisore

Pierluigi Reschiglian

Co-supervisore

Valentina Marassi

Esame finale anno 2025

Index

Abstract

Nanomedicines (NMs) are therapeutic or diagnostic medicines with dimensions typically between 1 and 1000 nm. NMs have drawn attention due to their ability to improve therapeutic efficacy and reduce toxicity compared to traditional drugs. Despite progress, many NMs struggle to transition from development to clinical use due to challenges like carrier toxicity, instability, and complex quality control (QC). The diverse nature of NMs makes difficult to establish universal analytical methods. Asymmetrical Flow Field-Flow Fractionation (AF4) is a promising technique for separating and characterizing nanoparticles (NPs), polymers, and macromolecules in a wide array of analytical conditions. This research aims to explore the potential of AF4 as a *passepartout* technique in characterizing NMs during the various stages of their development. Chapter 1 provides an overview of the topic.

Chapter 2 focuses on Polydopamine (PDA) nanosystems, widely used in fields like drug delivery due to their biocompatibility and degradability although its structural diversity remains poorly understood. A miniaturized form of AF4, combined with multiple detectors, identified two distinct species formed during PDA synthesis. This breakthrough highlighted the ability of the technique to select optimal PDA nanoforms for clinical use.

Chapter 3 discusses antimicrobial NPs. Nanosilver-based antimicrobials, combined with PDA, show potential in combating bacterial resistance. AF4, in conjunction with light scattering and spectrophotometric detection, streamlined the synthesis, purification, and characterization of these NPs, therefore acting as an eco-friendly multi-purpose tool.

Chapter 4 examines the behavior of magnetic NPs in biological environments, focusing on stability and protein binding. AF4 allowed to study real-time interactions between MNPs and human serum albumin, addressing key safety concerns.

Chapter 5 finally focuses on peptide-based drugs and their aggregation states. AF4 was crucial in assessing stability of liraglutide to aggregation, providing accurate insights into potential aggregation phenomena, which is a vital factor for regulatory approval of its various formulations.

Chapter 1. Introduction

1.1 An overview on nanomedicine

NMs are typically defined as medicines that utilize nanotechnology for therapeutic or diagnostic purposes, with dimensions controlled within the nanoscale range (1–1000 nm) [1]. In the field of pharmaceutical sciences, NMs refer to the application of nanotechnologies in the production of APIs as nanoscale particles or in combination with suitable nanomaterials to form nanoscale particles, which are then further formulated into versatile dosage forms [2].

NPs are key components of nanomedicine and, currently, a large variety of NP types exist. Examples are inorganic materials such as mesoporous silica NPs (MSNP) [3], superparamagnetic iron oxide NPs (SPIONs) [4] quantum dots (QDs) [5], plasmonic NPs [6], gold nanoclusters (GNCS) [7], silver NPs [8] upconverting NPs (UCNPs) [9], and many more. Organic based NPs are also highly involved in nanomedicine. Within this class, the main subclasses include lipid micelles [10], different polymeric nanostructures [11] protein constructs [12] ribonucleic acid NPs (RNPs) [13], carbon dots (C-dots) [14], nanodiamonds (NDs) [15], carbon nanotubes (CNTs) [16] and graphene [17].

Although their inclusion in the nanomedicine field is controversial, peptides can be considered part of NMs when engineered to self-assemble or conjugated/encapsulated within nanocarriers turning them into peptide-based NMs for drug delivery or therapeutic purposes [18]. Additionally, some of these peptides are on the nanoscale on their own, and therefore are subjected to some of the common problems of the classical nanomedical devices (e.g. aggregation). Altogether, their treatment should not be considered completely detached from the nanomedical field.

NPs are used in disease treatment, functioning as delivery vehicles for drugs, as bioactive materials, or as components in implants [19]. NP-based systems are particularly effective at crossing biological barriers. In tumors, they enter through the leaky vasculature and are retained due to poor lymphatic drainage, a phenomenon known as the enhanced permeation and retention (EPR) effect [20]. There is ongoing debate regarding the effectiveness of active targeting (ligand/receptor-mediated) versus passive targeting, but in all cases, carriers must first reach the target site before

binding to cell receptors or being retained by other mechanisms [21]. Currently the drug delivery field dominates nanomedicine market [2].

Smart NPs are also designed to provide contrast in the target area and report information about the local environment after being introduced into the body. This information aids in imaging the fine structures of organs, labeling tissues with specific markers, and allows local detection of molecules of interest, which is crucial for analyzing diseases inside the body. Additionally, NPs are key components in high-throughput diagnostic machines used to analyze extracted samples (e.g., blood, tissue) outside the body, helping to rapidly detect biomarkers and molecular changes. Multifunctional or theragnostic NPs that can both diagnose and treat while monitoring therapeutic efficacy are also being developed [22].

Finally, nanomedicine is not limited to colloidal materials and the technologies used to evaluate them for *in vivo* applications [23]: it also encompass the design of scaffolds and surfaces for engineering sensors, implantable systems, and electronics to support tissue regeneration (e.g., regenerative medicine) [24].

Despite flourishing research, the majority of nanoformulations under investigation fail to progress into commercial products due to one or more challenges, such as carrier toxicity, poor manufacturability, instability, and difficulties in QC.

Given the wide array of application, four macro areas can be identified: (1) *in vivo* therapeutics, (2) *in vivo* diagnostics, (3) *in vitro* diagnostics, (4) implantable nanomaterials, which were extensively covered in the titanic work of Pelaz et al. [24].

This section will briefly summarize the main applications and systems exploited in nanomedicine for *in vivo* therapeutics which represent the most relevant area of nanomedicine both in terms of systems studied in this work as well in terms of the current market. Further and specific information on the nanomedical systems studied in this work can be found in the dedicated chapters.

1.1.1 Nanomedicine for *in vivo* therapeutics

Delivery systems

Nanosystems showed success as delivery systems (either by uptake or encapsulation) as well as in other applications due to several advantages over traditional methods:

Selective targeting and crossing of biological barriers. According to EPR effect [21], NMs exhibit many beneficial features for targeted cancer therapy, in contrast to those of conventional small molecular anti-cancer drugs, which tend to spread indiscriminately in normal tissues and organs, thus leading to systemic adverse effects [25], [26]. Additionally, nanosystems can be engineered to specifically target diseased cells, such as cancer cells, by recognizing unique surface markers. This targeted approach minimizes damage to healthy tissues and improves drug efficacy. Furthermore, NPs can cross biological barriers such as the blood-brain barrier, allowing drugs to reach otherwise inaccessible areas of the body, such as the brain [27].

Improved drug bioavailability, and reduction of its side effects. Drug loading on/into NPs can improve drug bioavailability in two ways: (1) by enabling the solubility and stability of drugs that are poorly soluble in water, allowing for better absorption and distribution in the body [28]; (2) by protecting drugs from degradation in the body (e.g., in the stomach or bloodstream), ensuring that they reach their target site intact [29]. Additionally, since a lot of drugs, especially anti-cancer drugs such as doxorubicin, have strong side effects, encapsulation in nanodevices represents a way to bypass/reduce them [30].

Multifunctionality. Nanosystems can be loaded with multiple drugs or imaging agents, enabling simultaneous therapy and diagnosis (theranostics) [31].

Controlled Release. Nanosystems can be designed to release drugs in a controlled manner over time, ensuring a sustained therapeutic effect and reducing the frequency of dosing [32].

The main application is the drug delivery of anti-cancer molecules, and among the various nanosystems, liposomes have been the most successful in this field [28] (Table 1.1).

Drug Name	Platform	API	Year of first approval
SMANCS	Polymer conjugate	Neocarzinostatin	1993, Japan
Doxil®	Liposome	Doxorubicin	1995, USA
DaunoXome®	Liposome	Doxorubicin	1996, USA
Ontak®	Fusion protein	Diphtheria toxin	1999, USA
Myocet®	Liposome	Doxorubicin	2000, Europe
Zevalin®	Anti-CD20 antibody	Yttrium-90	2002, USA
Abraxane®	Albumin bound NP	Paclitaxel	2005, USA
Genexol-PM®	Polymeric micelle	Paclitaxel	2005, Korea
Marqibo®	Liposome	Vincristine	2012, USA
Onivyde®	Liposome	Irinotecan	2015, USA
Vyxeon®	Liposome	Daunorubicin and cytarabine	2017, USA
Mylotarg®	Anti-CD33 antibody	Calicheamicin	2017, USA
Hensify®	Nanoparticle	Hafnium oxide	2019, USA

Table 1.1. Examples of market-approved anti-cancers NMs. Adapted from [33].

Other delivery-related applications are gene therapy, vaccine productions and immunotherapy. Gene therapy is a therapeutic practice which revolves around making site-specific alterations to achieve therapeutic treatment. During this procedure, the patient genome can be partially altered through the replacement, insertion, or deletion of genetic material [34]. Since viruses are designed to insert their own genetic information into host cells, they have become the most utilized gene-delivery vehicles. However, gene therapy using viruses may induce severe clinical adverse effects. In response to these concerns, researchers are focusing on creating fully synthetic non-viral carriers. NPs have shown enormous promise as non-viral carriers for the targeted delivery of genetic material. In particular the most exploited NPs for such applications are gold NPs [35], iron oxide NPs [36], polymers [37, 38], and lipid-based NPs [39-41]. Nevertheless, the US Food and Drug Administration (FDA) has not yet approved gene treatments based on NPs.

Traditionally, vaccines have been developed using whole killed or live attenuated pathogens. However, current research is focused on creating subunit vaccines that are more precisely defined, easier to produce, and safer. Additionally, particulate vaccines provide enhanced protection of antigens from enzymatic degradation and enable the simultaneous delivery of molecular adjuvants alongside the antigen to antigen-presenting cells (APCs), thereby enhancing both cellular and humoral immune responses [42]. In this regard, liposomes, along with other lipid-based structures, have emerged as the leading carriers of choice [43]. The first study demonstrating the ability of

liposomes to induce immune responses when used as vaccine adjuvants or combined with antigens was published in the 1970s [44]. Since then, liposome-based vaccines for hepatitis A (Epaxal®), influenza (Inflexal®), malaria (Mosquirix™), shingles, and post-herpetic neuralgia (Shingrix®) have become well established in the market [45]. Arguably the most groundbreaking application of liposome technology in vaccines is the development of mRNA vaccines against COVID-19 by Pfizer/BioNTech and Moderna [46].

The objective of immunotherapy is to harness the host immune response to achieve a long-lasting therapeutic effect. However, management of the severe side effects of immune-therapeutics remains challenging, as they may trigger autoimmune reactions and non-specific inflammation [47]. Through the use of NMs and biomaterials, it is becoming increasingly feasible to achieve targeted delivery of immunomodulatory agents to specific sites while providing enhanced pharmacokinetics, improved therapeutic efficacy, and reduced dose-dependent systemic toxicity [47, 48]. Although most of these advances remain in the preclinical phase, some have received FDA approval and are currently undergoing clinical trials [33]. Liposomes, polymer NPs, and PEG-drug conjugates are among the NP-based therapies currently approved for treating various immunological disorders [49].

Despite the growing interest in NP-based immunotherapy, major problems remain in the clinical translation of these immunostimulatory NPs. Especially when studying the toxicity of those nanosystems it is particularly difficult to evaluate how NPs interact with biomolecules and to assess if the device can alter also other intracellular signaling pathways. This has led to the withdrawal of several nano-formulations from the market, even after receiving FDA approval [33].

Photodynamic therapy

Despite advancements in tumor treatments, challenges like non-specificity, drug resistance, low response rates, and toxicity-related side effects persist [50]. Photodynamic therapy (PDT) provides a non-invasive, targeted alternative where light-activated photosensitizers generate reactive oxygen species (ROS) to destroy tumor cells [51]. However, the clinical translation of PDT is hindered by its traditional lack of tumor selectivity, which is limiting its clinical use [52]. Nano photosensitizers (NanoPS) can overcome these obstacles, utilizing the EPR effect for targeted

tumor delivery that improves PDT efficacy and specificity [53]. NanoPSs can also be functionalized with ligands or antibodies, enhancing tumor cell recognition and binding. Moreover, their optical properties can also be tuned to controlling particle size and structure to enable optimal absorption of photosensitizers at specific wavelengths, which improves PDT precision and efficiency [54]. Overall NanoPSs improve therapy outcomes while reducing harm to normal tissues. An overview of the main systems exploited in this field is reported in Table 1.2.

Mechanism	Nanosystems exploited
PDT	PNPSs
	Nanoliposomes
	Nanohydrogel particles
	MNPSs
	CNPSs
	QDPSs
	UCNPs
	Organic frameworks

Table 1.2. Overview of the nanodevices used in photodynamic therapy. Adapted from [33]. Abbreviations: polymer-modified nanophotosensitizers (PNPSs); metal nanoclusters-based photosensitizers (MNPSs); carbon nanophotosensitizers (CNPSs); quantum dot photosensitizer (QDPSs); upconversion NPs (UCNPs).

Despite significant progress, the widespread clinical use of NanoPS-mediated PDT still faces several challenges in terms of biocompatibility, long-term safety, standardization of synthesis methods, and regulatory approvals. Currently, only a few NanoPSs are approved for clinical use, with most remaining at the basic research or clinical trial stage [33].

Antimicrobial Agents

In recent years, microbial infections have posed a global health burden due to the emergence of resistant strains of viruses [55], bacteria [56], pathogenic fungi [57], and protozoa [58], against which conventional therapies offer only limited effectiveness.

The development of biomedical nanomaterials has led to the emergence of new antimicrobial agents, either as novel treatments or augmenting current conventional antimicrobials. This progress is driven by the vast physicochemical properties and functionalization potential (ligand attachment) of NPs [59-61]. The antimicrobial mechanisms of NPs include the destruction of cell

membranes, enzyme pathway blockage, alteration of microbial cell walls, and disruption of nucleic materials [55]. Within this framework, metal NPs, especially Ag-based NPs, have found a wide range of applications [61]. Additionally, since drug encapsulation enhances the efficacy of antibacterial drugs, liposomes have been used to develop formulations capable of targeting even highly drug-resistant structures. For instance, Arikayce®, a liposome-encapsulated amikacin formulation, was introduced to the market in 2018 [62].

1.2 Delivering NMs

For decades, the field of nanomedicine has promised to revolutionize treatment outcomes for millions of patients. Whether this field of research has actually fulfilled the expectations or rather keeps "lofty promises" is debatable [63]. In fact, an argument is that the potential of the field has somehow been overestimated, and that the field has been overly funded and overly focused on cancer therapy [64]. On the other hand, NM enthusiasts and NM-related agencies comprehensively defend the field highlighting the number of NMs approved for clinical use (currently more than 50) [65-67]. Additionally, they point out the superior estimated total success rate from phase 1 to approval of 6%; compared to the 3.4% of the traditional ones [68, 69].

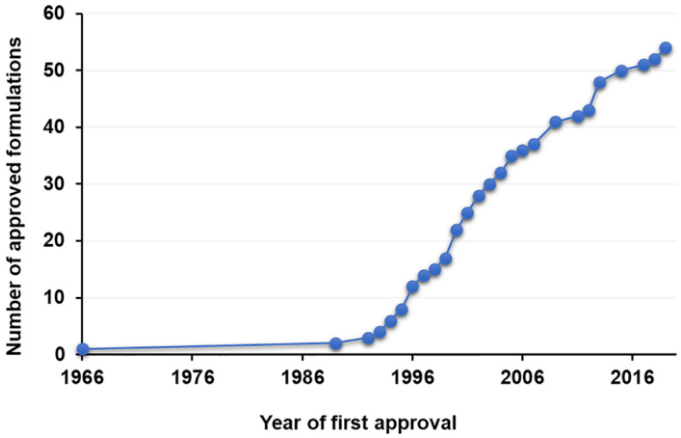

Figure 1.1. Evolution of the approved nanomedicine formulations (cumulative number/year). First year of approval reported for formulations approved by multiple agencies (e.g. EMA and FDA). Adapted from [70].

Regardless of individual opinions, some difficulties in clinical translation of NMs honestly emerge [71], such as:

(i) Lack of education in business management, especially at the academic level.
(ii) Difficulties in performing the pre-clinical characterization and safety assessment from early stages, due to the lack of protocols and uniformity.
(iii) Difficulties in scale-up and Good Manufacturing Practice (GMP).
(iv) Uncertainty and fragmentation in the regulatory framework.

As the readers can see, the issues are complex and multidisciplinary, the solution for which are up to both nano-scientists and analytical chemists, as it will be further discussed.

1.2.1 Difficulties and approaches in the characterization of nanomedical formulations for clinical development

The complexity of nanomedical (NML) formulations often does not allow for a straightforward characterization approach. NML formulations may vary in size, composition, surface coating, charge, drug load, and many other properties, all affecting their behavior. This variability causes difficulties in developing robust analytical methods that can be universally applied to such a wide and diverse array of systems [72]. As a result, a wide range of different techniques, approaches, and methodologies are being used, generating results of variable quality and making them difficult to compare. Consequently, the development of standardized and regulatory-accepted methodologies is extremely important for the optimization of the regulatory process and for the acceleration of clinical of NMs while reducing potential risks to patients. Currently, published regulatory documents can be divided into two types: (1) Type 1, guidance-like documents that offer an overview of different methods and identify a series of critical quality attributes (CQAs) important for market approval; and (2) Type 2 documents, which include specific test methods and guidelines that address in a more detailed and practical way the procedures for determining certain CQAs.

The main physicochemical CQAs that should be defined/known to submit a nano-based drug for market approval, along with the most common approaches used to assess them, are shown in Table

1.3. In the following subsections, the main physicochemical CQAs to be assessed for market approval will be individually discussed in a concise and practical manner.

Physicochemical parameter	Main available related technologies	Standard method for certain CQA?
Chemical composition, structure, impurities	HPLC-Multidetection (MS, UV, dRI, ELSD, CAD), GC-MS, ^{1}H- ^{13}C- and ^{31}P-NMR, Raman Spectroscopy	YES
Particle size distribution and concentration	TEM, DLS, NTA, TRIPS, SEC/FFF-Multidetection (UV, dRI, DLS, MALS)	YES
Surface properties (e.g. zeta potential, hydrophobicity, surface area, surface coating)	zeta potential: DLS, EPR, Fluorescence labelling Hydrophobicity: Dark-field microscopy Surface Area: NMR Surface coating: Chromatography approaches	YES (z-potential only)
Drug loading	HPLC- (MS, UV), CE, AF4	YES (Partially standardized)
Drug release (In vitro/in vivo/in physiologically-clinically relevant media)	API separation: filtration, UF, UC, dialysis bags API quantification: LC-MS Standalone techniques: HPLC-MS, CE-ICP-MS, AF4 (dRI, UV, MALS)	YES (Partially standardized)
Chemical and physical stability, degradation paths and relative kinetics	Size/PDI: DLS, SEC, AF4, FLD assays, DCS Composition: HPLC (CAD, ELSD, MS) API stability: HPLC-MS, SAXS, SANS	YES (Partially standardized)

Table 1.3. Summary of the main physicochemical CQAs that should be defined/known for a NM to be considered for market approval and most common approaches used to assess such CQAs. "Partially standardized" refers to methods which only partially meet the requirements for a proper standardization (e.g. lack of the evaluation of intra-laboratory variability and/or the existence of formal standards). Table from [28].

Chemical composition

Information indicating components of the nano system, their relative abundance, their degradation products and impurities are required for market approval. When synthetic and/or partially synthetic components are being used, results obtained from the application of the same procedures to reference material should be correlated. When new methods are being used, the product manufacturer should anyway provide the standardization procedure method following the rule of ICH guidelines [73]. The techniques exploited for the analysis of this QCA are resumed in Table 1.3. One of the most common analytical approaches is based on the rupture of the nanodevice and

its analysis with chromatographic techniques coupled with a suitable array of detectors [28]. NMR and Raman spectroscopy have also been exploited [74, 75].

Particle size distribution (PSD) and polydispersity index (PDI)

The properties of nanosized materials, such as their ability to penetrate biological barriers and the clearance velocity, are greatly affected by their dimension and morphology. Consequently, PSD and PDI are extremely important CQAs to evaluate in the context of regulatory approval.

Particle morphology and size can be directly visualized by several transmission electron microscopy (TEM) techniques, such as negative stain [76], freeze structure [77], and cryogenic microscopy [78]. Negative-stain TEM has the drawback of requiring sample drying before the staining process, which may cause sample shrinkage, collapse, or aggregation. In contrast, the other two variants do not require drying; moreover, cryo-TEM has the advantage of requiring the minimum amount of work for sample preparation. Scanning electron microscopy (SEM), although applicable, is not often exploited for lipid NPs due to its disruptive nature. However, in recent years, environmental scanning electron microscopy (ESEM) has been developed to image liposomes in their hydrated state and to investigate their changes in different environments [79].

Overall, although microscopy is extremely powerful for morphological studies, it suffers from several major drawbacks, such as being slow and expensive. Moreover, it is not particularly suited for accurately calculating PDI or even PSD, as the results can be affected by operator bias.

The PDI of a dispersion and its mean hydrodynamic radius (Rh or r_h) can be accurately measured using dynamic light scattering (DLS) [80], nanoparticle tracking analysis (NTA) [81], and tunable resistive pulse sensing (TRPS) [82]. These single-particle sizing techniques have the advantages of being fast, simple to use (DLS), and relatively inexpensive, making them recommended for fast screening of polydisperse samples or for QC of samples with relatively low dispersity. Since these systems usually operate in batch mode, a drawback is their low reliability in measuring complex or non-homogeneous samples. Although DLS remains the most widely used technique due to historical reasons, comparative studies have shown that NTA and TRPS resolve multimodal nanoparticle mixtures significantly better than batch-mode DLS [83].

To obtain reliable PDI and PS results from complex samples, a separation technique such as Size Exclusion Chromatography (SEC) or AF4 coupled with an array of concentration (UV, dRI) and size measuring (DLS, MALS) detectors is required. SEC separates NPs (free and drug-loaded) based on their hydrodynamic radius in the range of 1-100 nm, and is by far the most used technique for the separation and characterization of NML devices such as liposomes [84]. However, the technique is characterized by a series of drawbacks that limit its application (see section 1.3). The presence of a stationary phase can induce aggregation of the sample and imposes limitations on the mobile phase composition, which must be compatible with the column, thereby limiting the possibility of studies under native conditions. Moreover, adsorption and/or dissociation processes caused by interaction with the stationary phase may be observed [85]. These problems are solved by AF4 [86, 87]. Table 1.4. resumes the methods and procedures for PSD and PDI determination using the techniques discussed above.

Characterization technique	Standardized methods
TEM	ISO/WD 21363 ISO/TS10797:2012
Cryo-TEM	ASTM WK54615 ASTM E3143 - 18b
SEM	ISO/WD 19749
DLS	ASTM WK54872 ISO 22412:2017 ASTM E2490-09(2021)
NTA	ISO 19430:2016 ASTM E2834-12(2022)
SEC multidetection	ISO 16014 (2019)
FFF (AF4) multidetection	CEN ISO/DTS 21362:2021
Analytical UC	EUNCL (PCC-24)
SMLS	ISO/TS 21357:2022

Table 1.4. Summary of the Type 2 documents addressing particle size distribution (PSD) and polydispersity index (PDI) determination classified based on the technique exploited. Adapted from [28].

Morphology and Lamellarity

Although information on morphology and lamellarity can be obtained from AF4 platforms, other approaches such as microscopy (TEM, SEM) are more commonly used, and regulated methodologies are available [77, 78, 88]. At present 3 documents disciplining the morphological evaluation of nano systems through microscopy have been published. However, none of them specifically focuses on biomedical nano systems (Table 1.5).

Characterization technique	Advantages
TEM	• ISO/WD 21363:2020 • ISO/TS10797:2012
TEM, EDX	• ISO/WD 21363:2020

Table 1.5. Summary of the Type 2 documents addressing particle morphology classified based on the technique exploited. Table from [28].

Surface properties: zeta potential, surface area, hydrophobicity, and surface coating.

The zeta potential (or ζ-potential or z-potential) is a parameter associated to the surface charge of the NPs which is vital to estimate the stability of the technology, the in vivo performance and the biological fate of colloidal systems. Since charge on the surface of NPs governs their mobility, which affects the intensity of the scattered light, DLS instrument are commonly used to estimate the zeta potential by monitoring changes in the intensity of the scattered light originated by a changing electric field applied on the particles [88]. This technique is also commonly referred as Phase Analysis Light Scattering (PALS) or Electrophoretic Light Scattering (ELS). Alternatively, the surface potential of NML devices such as liposomes can be measured by several techniques including fluorescence labeling [89], electron paramagnetic resonance [90], and the second harmonic generation from optical analyses [91].

Since zeta potential of NPs significantly depends on pH, temperature, ionic strength, drug loading and external environment [92, 93], it is important to regulate its measurement procedure to obtain reliable, homogenous and comparable results. At present, only two documents regulating zeta potential determination have been published (Table 1.6).

Characterization technique	Standardized methods/guides
Video microscopy and electrophoretic light-scattering	ISO 13099-1:2012, -2:2012, -3:2014
General standardized guide	ASTM E2865-12(2022)

Table 1.6. Summary of the Type 2 documents addressing zeta-potential determination classified based on the technique exploited. Table from [28].

Drug loading

Drug loading evaluation methods typically involve a series of common steps. Initially, the non-encapsulated free drug is separated from the nanocarriers using ultrafiltration, ultracentrifugation, dialysis, or solid-phase extraction. The free drug amount is then quantified and compared to the total drug amount. To ensure fair comparison between different formulations, it is important to report information regarding the initial ratios between the active pharmaceutical ingredient (API) and the nanocarrier, as well as the loading capacity (%) of the formulations. High-Performance Liquid Chromatography (HPLC), coupled with a variety of detectors such as UV/Vis tandem molecular mass spectrometry (LC-MS/MS), or Inductively Coupled Plasma Mass Spectrometry (ICP-MS), is the most used platform for API identification. Due to the specific nature of these techniques, they are highly API-specific and cannot be generally standardized. However, some Type 2 guidelines have been published (Table 1.7).

Capillary electrophoresis (CE) has been used to separate and quantify both loaded and non-loaded APIs [94]. Similarly, AF4 has been employed as a separation technique, followed by API determination via HPLC [95, 96]. AF4, as a standalone technique, can also be used as a fast and cost-effective pre-screening method to qualitatively observe and estimate API distribution in different NPs [97]. However, no standardized method involving solely AF4 has been established to date.

Characterization technique	Parameter	Protocol	Notes
LC-MS/MS	Drug loading	EUNCL (PCC-30)	• Measure of total drug loading • Fully qualified but no formal standard exists
Ultrafiltration + HPLC, LC-MS/MS	Drug loading	EUNCL (PCC-31)	• Measure of free drug fraction • Fully qualified but no formal standard exists
RP-HPLC–ICP-MS	Drug loading	NCI-NCL (PCC-14)	• Measure of free drug fraction • Applicable to gadolinium-based contrast agent • Commonly used but not officially validated
Ultrafiltration + HPLC, LC-MS/MS	Drug release	NCI-CL (PHA-1&2)	• Measure of drug release in plasma over time • The nanocarrier must be separable from the API trough UF and the latter must be detectable by MS. • Commonly used but not officially validated

Table 1.7. Summary of the Type 2 documents addressing drug loading/release classified based on the technique exploited. These methodologies, although routinely used in relevant R&D environment, are only "partially standardized" since lack the evaluation of intra-laboratory variability and/or the existence of formal standards. Table from [28].

Drug release in simple media, in vitro, in silico and in vivo

Drug release, like drug loading, can be seen as a two-step process: 1) separation of the encapsulated API from the medium with the free/released drug; 2) quantification. The separation method should neither disrupt carrier integrity nor alter the concentration balance between encapsulated and free drug. For drug release in simple media, standard bioanalytical purification methods like chromatography, liquid-liquid extraction, and equilibrium methods are used [98]. In vitro studies are grouped into four types based on how sample incubation and separation occur. (1) The simplest process involves separation of the sample from the media via ultracentrifugation, filtration, or SEC, followed by off-line API quantification [99, 100]. However, this can be inefficient for submicron NPs and may disrupt NMs, affecting results. (2) Dialysis sacks [101] simplify nano-system separation but require careful design to avoid aggregation or pore blockage, which can underestimate drug release. A reverse dialysis method [102] addresses some issues by placing the sample in the bulk release media and sampling it from the dialysis sack. (3) Methods combining dialysis sacks with media circulation have also been developed [103]. The United States Pharmacopeia (USP) recommends modifications to existing equipment or using USP I and USP IV to avoid equipment proliferation, as described by Solomon et al. [104]. (4) Multi-detection (MD) separative platforms can serve for both sample separation and API quantification, with

HPLC being the most common method, though CE [105] and AF4 [106, 107] are also used (Table 1.8). In vivo studies using mouse, rat, and pig models are recommended to assess nanodrug pharmacokinetics and distribution [108, 109]. The many challenges of in vitro and in vivo studies make universal methods difficult, leading to a reliance on mathematical models for predicting drug release mechanisms [110, 111]. However, these models still depend on in vitro and in vivo data and need further validation for regulatory use.

Approach to drug release	Advantages	Limitations
Separation (UC or UF) + offline detection	• High flexibility in terms of drug (UC) • Straightforward instrument setup • Uniform agitation or stirring	• Liposome's damage • Filter clogging/particle deformation • Low efficient separation • Sedimentation rate of the components
Dialysis/Reverse dialysis + API detection in the other compartment	• Economic/simple • Simultaneous separation and in situ monitoring of the released API • Easy changes of the release medium	• Underestimation of drug release caused by sample aggregation and obstruction of the sac pores
Dialysis (circulation of release media) + offline detection	• Better discrimination of drug release profiles (compared to standard dialysis) • Simultaneous separation and on-line monitoring of the released API • Easy changes of the release media	• High volume of release media • Two stage diffusion • Compatibility of the dialysis chamber with the apparatus
Flow separation platforms (HPLC, AF4, CE)	• Separation and contemporaneous powerful characterization/ API release evaluation	• Complex • Optimization of experimental conditions for every system studied

Table 1.8. Schematization of the advantages and limitations associated with the main approaches to drug release evaluation. Table from [28].

Physical and chemical stability

The main manifestations of physical instability are aggregation of the NPs and leakage of the loaded API. Since these phenomena greatly impact size and PDI, studies exploiting DLS [112], SEC [85] and AF4 [97] to evaluate NP stability have been reported. For organic-based NPs, instability can also be due to the hydrolysis/oxidation of particle components (ex. phospholipids for liposomes); the products of such processes are often separated and detected by several chromatographic approaches [28]. As far as regimentation is concerned, a series of Type 2 documents addressing specifically the monitoring of physical stability of nanomaterials exists (Table 1.9). Chemical stability studies involving highly specific chromatographic measurements for each NP/API combination are instead disciplined by well-established ICH ruling (Table 1.9)

Characterization technique	Parameter	Protocol	Notes
DLS	Physical stability (NPs size over time)	EUNCL (PCC-21)	Fully qualified but no formal standard exists.
NTA	Physical stability (NPs size over time)	EUNCL (PCC-23)	Commonly used but not officially validated.
Analytical UC	Physical stability (NPs size over time)	EUNCL (PCC-24)	Commonly used but not officially validated.
AF4-UV/VIS-MALS-DLS	Physical stability (NPs size over time)	EUNCL (PCC-22)	Must be adapted to the system studied. Fully qualified but no formal standard exists.
Chromatographic methods	Chemical stability (degradation products over time)	ICH-Q1	Has to be adapted to the system studied

Table 1.9. Summary of the Type 2 documents addressing physical and chemical stability of NPs classified based on the technique exploited. These methodologies, although routinely used in relevant R&D environment, are only "partially" standardized since they lack evaluation of intra-laboratory variability and/or the existence of formal standards. Table from [28].

1.3 AF4 and detection

1.3.1 Flow Field-Flow Fractionation (FFF) techniques

FFF techniques are separative and analytical platforms initially introduced by J. C. Giddings in the 1960s [113]. These techniques are used for separating and studying dispersions across a wide size range, from small peptides to particles larger than a micron, such as cells [93, 114]. FFF instrumentation is configured similarly to traditional HPLC systems, with pumps generating the eluent flow, followed by a sample injector, the separative element (the channel), and finally, the detectors. The distinct feature of FFF systems lies in their separative element, a capillary channel, often rectangular in shape. Unlike traditional chromatography, FFF operates without a stationary phase [115]. Instead, separation is achieved through the interaction of the laminar eluent flow (which has a parabolic velocity profile) along the channel axis and an external field applied perpendicularly to the flow, directed toward a channel wall known as the "accumulation wall". The sample components, or analytes, are separated based on differences in molar mass, size, or other physical properties, which cause them to move into different velocity regions within the parabolic flow profile [116].

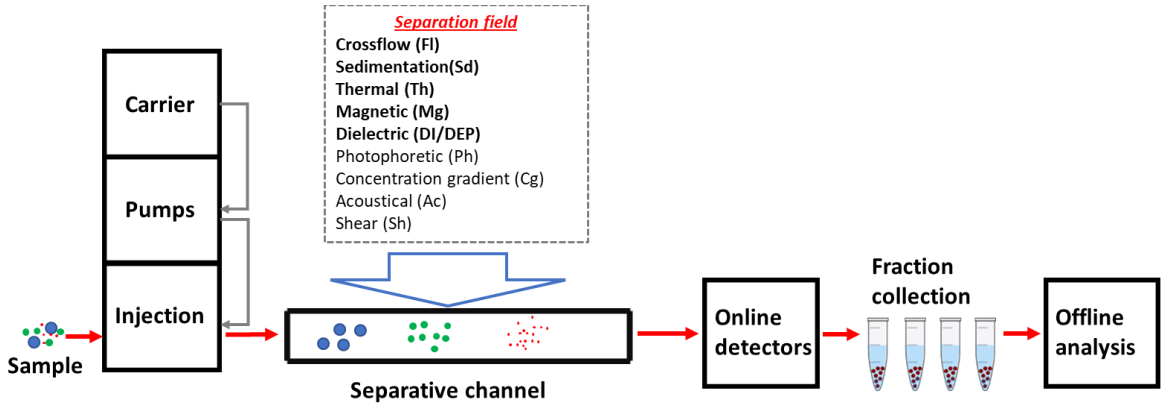

Figure 1.2. Schematic representation of an FFF platform. The separative channel is a schematization of the typical FFF channel. The dotted box reports the possible fields that have been theoretically studied to be exploited for separation in FFF. Only the fields in bold are nowadays significantly used. Image from [117].

The concentration distribution of analytes across the channel defines different operating modes in FFF [118, 119]. In *Normal mode*, analytes experience a balance between the drift velocity caused by the external field, which pushes them toward the accumulation wall, and their opposing diffusivity. Smaller analytes diffuse farther from the wall and are positioned closer to the center of the channel than larger ones. As a result, smaller analytes have shorter retention times. This mode is commonly used for the elution of macromolecules and NPs.

Reverse mode is typical for micron-sized particles, where diffusion away from the accumulation wall is negligible. In the ideal *Steric mode*, analytes of all sizes are pushed by the external force into contact with the accumulation wall. Larger analytes, which are subject to stronger flow vectors, are eluted faster than smaller ones, resulting in an elution order opposite to that in Normal mode. In practice, especially at high flow rates, *Hyperlayer mode* occurs. In this mode, lift forces generated by the flow push particles away from the wall, at a distance greater than their diameter. While the elution order remains reversed compared to Normal mode, retention now depends not only on particle size, but also on other physical properties such as shape, rigidity, density, and surface characteristics.

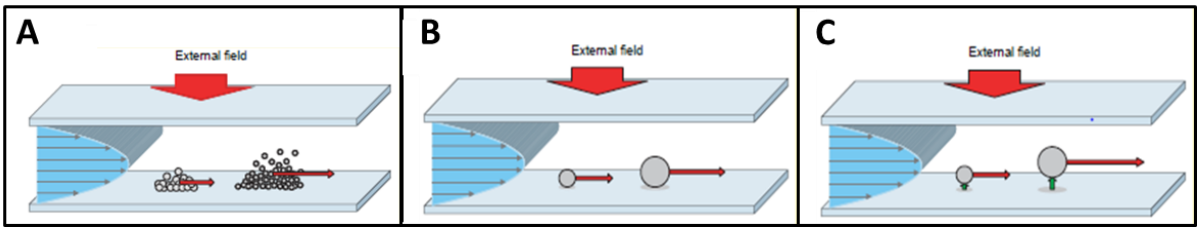

Figure 1.3. Schematization of the evolution modes in FFF. **A.** Normal mode **B.** Steric mode **C.** Hyperlayer mode. Image from [117].

The FFF separation range (about 15 orders of magnitude in mass, corresponding to a size range from few nanometers to about 100 µm) results from the possibility of changing the nature of the applied force field or gradient. Different FFF variants are thus distinguished based on different chemical-physical properties of the samples exploited for the separation.

Thermal FFF (ThFFF): This technique generates a temperature gradient between two highly thermally conductive blocks that form the channel walls. Separation is based on the analyte's Soret coefficient, which is the ratio between the thermal diffusion coefficient (D_T) and the hydrodynamic diffusion coefficient (D). ThFFF has been primarily used for polymer separation [120].

Flow FFF (FlFFF): In this widely used FFF variant, a perpendicular crossflow is applied to the main eluent flow, driving analytes towards the accumulation wall based on their diffusivity, which correlates with their hydrodynamic radius [121]; this allows for particle size characterization without the need of size standards (absolute method). There are three main variants of FlFFF:

- *Symmetrical FlFFF* (SF4): Here, the crossflow goes through the two channel walls, both of which are porous, and is generated by a separate pump from the elution flow. Although it has largely been replaced by other methods due to slower separation and lower resolution, it represents the original FlFFF format [122].
- *Asymmetrical FlFFF* (AF4): This variant features a single porous wall for crossflow and it is now the most widely adopted form of FlFFF. The flow splits into longitudinal and cross components, allowing for high-resolution separations [123]. Variants using hollow-fiber channels, frit-inlet channels, and thickness-tapered channels further refine the method, each addressing specific limitations or enhancing performance in steric and hyperlayer modes [124, 125].
- *Hollow-Fiber FlFFF* (HF5): This miniaturized version of F4 uses a porous tubular fiber as the channel. It offers greater detection efficiency and less sample dilution, making it ideal

for disposable use to avoid contamination [126]. Limitations of HF5 include reduced capacity for large sample quantities, though multi-module systems (MxHF5) can address throughput issues [127].

- *Electrical FFF* (ElFFF): This method applies an electric field generated by charged conductive walls (often graphite) to separate analytes based on electrophoretic mobility [128]. Pure ElFFF has been largely abandoned due to poor resolution and issues like interference from electrolysis [129]. However, a new variant, *Electrical Asymmetrical Flow FFF* (EAF4), combines ElFFF and AF4: this allows separation based on both size and charge, improving resolution for analytes with the same size but different charge [130].
- *Sedimentation FFF* (SdFFF): In SdFFF, the channel is rotated to create a centrifugal force perpendicular to the mobile phase flow. This technique separates analytes based on their mass, diameter, and density differences [131]. This technique is also known as *Centrifugal FFF* (CF3).
- *Gravitational FFF* (GrFFF): This cost-effective method uses Earth's gravity as the applied field and it is suitable for separating large analytes (1–100 μm), such as inorganic particles or biological entities like whole cells [132]. A sub-variant, SPLITT-GrFFF, allows for continuous binary separations on a preparative scale [133].
- *Magnetic FFF* (MgFFF): MgFFF separates magnetic NPs by exploiting their magnetic dipole moments. It can also be used for systems where the NPs are bound to other entities, such as antibodies or drugs for magnetic drug delivery. Various separative channels and magnetic fields have been developed for this purpose; however, no one is commercially available [134, 135].
- *Dielectrophoresis FFF* (DIFFF or DEPFFF): This technique uses a non-uniform electric field to induce dipoles in analytes, separating them based on their polarizability [136]. It has been used to fractionate colloidal NPs and isolate diseased from healthy cells.

Other FFF variants based on other fields have been theorized. Among them, only Acoustical FFF has been developed and tested [137]. Although it hasn’t imposed as a stand-alone FFF variant, it has recently been exploited to improve the resolution of GrFFF [138].

The main distinguishing features of the FFF sub-techniques available are listed in Table 1.10.

Technique	Separation based on analytes:	Tipical size range	Main Applications
FlFFF	Hydrodynamic diffusion coefficient	1 nm – 20 µm	Proteins, polysaccharides, lipids, NPs, micelles, vesicles, organelles, polymers
ElFFF	Electrophoretic mobility, size	1 nm – 1 µm	NPs, proteins viruses, bacteria
ThFFF	Thermal diffusivity, size	5 nm – 10 µm	Polymers, gels, NPs
GrFFF	Size, density	1 – 100 µm	Cells, bacteria, organelles
SdFFF	Size, density	10 nm – 50 µm	Cells, bacteria, organelles
DlFFF	Size, dielectric properties	1 – 20 µm	Cells

Table 1.10. Main features of the most common FFF techniques. Table from [117].

1.3.2 FFF and AF4 theory

As previously mentioned, AF4 represents the most successful and commonly exploited FFF variant. The technique allows to separate systems with size spanning 1 nm – 20 µm, according to their hydrodynamic diffusion coefficient. The typical channel consists of a filtration membrane made of an appropriate material (such as cellulose) with known porosity, on which a spacer is placed to define channel shape and size. The spacer typically has a thickness of 250-800 µm. Beneath the membrane, corresponding to the accumulation wall, there is a porous support made of ceramic or metallic material, known as the frit. The entire system is enclosed by two polymeric or metallic plates. As mentioned earlier, two flow components in AF4 are generated from the elution flow through a system of pumps and regulation valves.

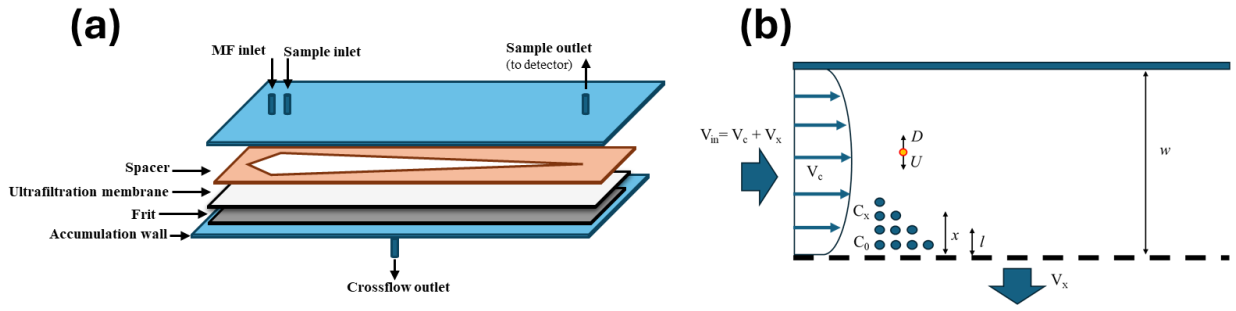

Figure 1.4. (a). Schematization of a typical AF4 channel. **(b)**. Cross section of the AF4 channel. Adapted from [139].

The classical FFF retention model establishes a link between particle retention time and a physical property of the analyte, based on four key assumptions:

1. *Operating Mode and Channel Geometry*: Particles undergo Brownian motion, and the channel can be modeled as two infinite, uniform, parallel plates.
2. *Stationarity of the Migration Process*: The applied field strength on the analyte remains constant across the entire channel.
3. *Cross-sectional Concentration Distribution*: Steric effects and interactions between particles, as well as between particles and the channel walls, are negligible compared to the field strength (particles are treated as points).
4. *Cross-sectional Velocity Distribution*: The elution flow is laminar, and particles move at the same speed as the streamline in which they are located (no temperature effects).

If the four assumptions are respected, under Normal elution conditions, the applied field compresses the analytes towards the accumulation wall, where they arrange with a distribution determined by the field-induced transport towards the wall and the diffusion away from the wall to lower concentration regions. When these two opposing transport processes are in equilibrium there is no net flux of material, and the concentration profile has an exponential distribution as described by (Equation 1):

$$c(x) = c_0 e^{-\frac{U}{D}x}$$

Equation 1. Analyte distribution in the channel. $c(x)$: analyte concentration at the distance *x* from the accumulation wall. c_0: analyte concentration at the accumulation wall (x = 0). *U*: particle velocity induced by the field force. *D*: diffusion coefficient.

Brownian diffusion can be expressed by the Nernst–Einstein equation (Equation 2).

$$D = \frac{kT}{f}$$

Equation 2. Nernst -Einstein equation. *k*: Boltzmann constant. *T*: temperature. *f:* friction factor

The particle velocity induced by the field force in a host medium (*U*) is related to the field force (*F*) as described in Equation 3.

$$U = \frac{F}{f}$$

Equation 3. *F*: field force applied.

Combining Equation 2. and Equation 3. the diffusion coefficient can be expressed as:

$$D = kt\frac{U}{F}$$

Equation 4.

A mean layer thickness (l) of the sample can be defined as the distance from the accumulation wall to the center of mass of the sample zone. It is expressed as the ratio of thermal energy to the applied force:

$$l = \frac{kT}{F} = \frac{D}{U}$$

Equation 5. l: mean layer thickness.

A dimensionless zone thickness (λ), known also as the retention parameter, can be defined as

$$\lambda = \frac{l}{w} = \frac{kT}{wF} = \frac{D}{UW}$$

Equation 6. λ: dimensionless zone thickness. w: channel height.

λ represents a measure of the extent of interaction between the field force and the sample components, which is independent from the channel height. The parameter assumes different forms according to the different separation force considered (different terms are substituted for F depending on the type of field applied).

In the case of an AF4 separation, the generic form of λ is expressed as in Equation 7 and D, given the approximation of considering the particles as solid homogeneous spheres, is described by the Stokes-Einstein equation (Equation 8).

$$\lambda = \frac{DV^0}{V_c w^2}$$

Equation 7. V^0: channel volume. V_c: the volumetric crossflow rate.

$$D = \frac{kT}{3\pi\eta d_h}$$

Equation 8. Stokes -Einstein equation. η: Solvent viscosity. d_h: hydrodynamic diameter.

The parabolic flow velocity profile is described by Eq 9.

$$v(x) = 6\langle v\rangle\left[\left(\frac{x}{w}\right) - \left(\frac{x}{w}\right)^2\right]$$

Equation 9. $v(x)$*:* parabolic flow velocity. $\langle v\rangle$: average velocity of the carrier.

The retention of the analytes can be expressed by the retention ratio (*R*), defined as the ratio between the average migration speed of the analyte *x* compared to the average migration speed of the carrier (Equation 10).

$$R = \frac{v_{zone}}{\langle v\rangle} = \frac{\langle c(x)\, v(x)\rangle}{\langle c(x)\rangle\langle v(x)\rangle} = \frac{t_0}{t_r} = \frac{V_0}{V_r}$$

Equation 10. *R:* retention ratio. v_{zone}: average velocity of the analyte zone. $\langle v\rangle$: average velocity of the carrier. t_0, t_r, dead and retention time. V_0, V_r: dead and retention volume.

By combining Equation 1, Equation 7 and Equation 10 it is possible to obtain Equation 11, which generalizes the relationship between *R* and λ for the majority of FFF techniques.

$$R = 6\lambda\left[\coth\left(\frac{1}{2\lambda} - 2\lambda\right)\right] \approx 6\lambda \;\; (if\ \lambda < 0.02)$$

Equation 11.

The relationship highlights the fundamental principle behind FFF separations in Normal mode: the higher the interaction of the analytes with the external field, the higher their retention times.

By substituting in Equation 11 the appropriate expression of λ according to the external field applied, it is possible to correlate the retention time to the physical properties based on which the analytes are separated. In the case of AF4, however, this approach provides only an approximate expression of *R* since it does not take into account the drop of V_c along the channel due to the

splitting of the channel inlet flow and the lack of crossflow at the upper nonporous wall [140]. Therefore, after proper resolution of Equation 10, which takes into account those phenomena and the proper expression of *D*, Equation 12 is obtained.

$$t_r = \frac{\pi\eta}{kT} r_h w^2 \ln\left(1 + \frac{V_x}{V_{out}}\right)$$

Equation 12. r_h*:* hydrodynamic radius. V_x*:* volumetric velocity of the crossflow. V_{out}*:* volumetric velocity along the channel

The latter equation highlights the fundamental relationship between t_r and r_h in AF4 Normal mode separation, which allows particle size calculation in absolute mode.

In the Steric/Hyperlayer mode of FlFFF, the retention ratio is instead expressed as

$$R = \frac{t_0}{t_r} = \frac{3\gamma d_h}{w}$$

Equation 13. γ*:* steric correction factor.

The steric correction factor (γ) is influenced by the field strength, migration flow velocity, and particle diameter [141]. Due to the complex nature of hydrodynamic lift forces, this factor has not been fully resolved, making it difficult to theoretically predict retention in the Steric/Hyperlayer mode [142]. As a result, a calibration is typically used to determine particle size based on retention time [143].

1.3.3 HF5

In both SF4 and AF4, interactions between sample components and the membrane or the frits that form the channel walls can lead to run-to-run sample carry-over due to incomplete sample recovery in FlFFF. Additionally, typical FlFFF channel volumes are around 1 mL, resulting in significant sample dilution at the outlet, despite partial improvements introduced with AF4. These factors can

impact reproducibility, sensitivity, and accuracy, especially when further characterization of fractionated analytes is required by coupling FlFFF with orthogonal analytical methods. For biological samples, contamination of fractionated analytes may also occur, potentially affecting their viability or functionality. To address some of these issues, tubular hollow-fiber (HF) filtration membranes, made from polymers or ceramics, have been utilized as potentially disposable, micro-volume channels for FlFFF, addressing some of these issues. In a typical HF5 setup, an HF is connected to a pump that drives a longitudinal flow of liquid (F_{in}) through the HF channel. A pressure drop is created between the inner and outer walls of the HF, either by a second pump drawing liquid across the HF or by applying backpressure at the longitudinal outlet of the HF. This pressure difference also generates a radial flow (F_{rad}) through the HF.

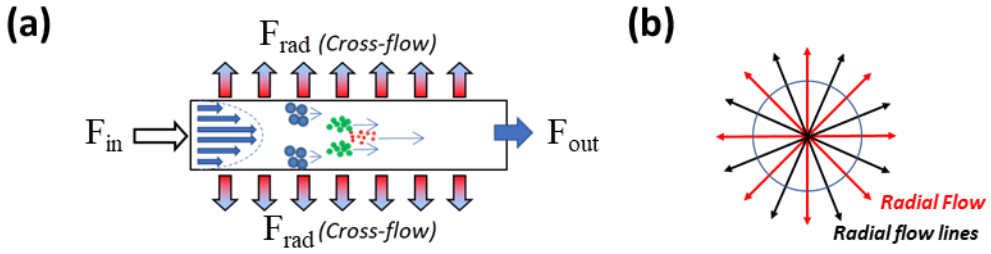

Figure 1.5. (a). Schematization of a typical HF5 channel. **(b)**. Cross section of the HF5 channel. Adapted from [144].

From a separative point of view the HF5 set up can be considered as a miniaturized AF4 system characterized also by a different channel geometry (cylindrical instead of trapezoidal). Therefore, the mathematical approach to the evaluation of the retention theory follows the same main steps illustrated in the previous sections taking of course in account the different channel geometry [145]. HF5 retention theory in in Normal and Steric/Hyperlayer mode is described by Equation 14 and Equation 15 respectively [146, 147].

$$t_r = \frac{3R_f^2 \pi \eta d_h}{8kT} \ln\left[\frac{F_{in} - \left(\frac{L_0}{L}\right) F_{rad}}{F_{out}}\right]$$

Equation 14. Normal mode elution in HF5. R_f: fiber radius. L: channel lenght. L_0: Focusing position inside the channel. F_{in}, F_{rad}, F_{out}: volumetric velocity along at the channel inlet, of the crossflow and at the channel outlet respectively.

$$t_r = \frac{t_0}{2\gamma}\frac{R_f}{d_h}$$

Equation 15. Steric/Hyperlayer elution in HF5.

In this work, when referring to both techniques, the acronym HF5 will be sometimes replaced by the more general AF4.

1.3.4 AF4 set up, operating modes and analysis optimization

As mentioned at the beginning of the section, FFF instrumentation is configured similarly to traditional HPLC systems with the main differences being represented by the separative channel (already described), and the employment of an additional element for splitting and control the fluxes going through the channel during the various phases of the experiment. Since the latter and its functioning may vary a lot between the different producers of AF4 instrumentation, in this section we give only a generic description of the possible experimental modes in AF4 and how the fluidics changes in the channel regardless the commercial device. The same description can be extended to HF5 keeping in mind the radial geometry of the device.

While working with a traditional AF4 system it is possible to operate in three different experimental modes:

- Separative Injection (SI)
- Flow Injection Analysis (FIA)
- Focus Flow Injection Analysis (FFIA)

Separative injection (SI)

The goal of this procedure is to separate the sample components as good as possible to maximize the information obtained from the detectors. The experiment consists of two main phases: *Focus injection* and *Elution*.

Focus injection: This phase begins by injecting the sample into the channel through a longitudinal flow of the mobile phase, while simultaneously introducing a second mobile phase flow from the opposing direction. When the sample is not injected with the longitudinal flow, the process is simply called Focus. The exact location of the focusing point depends on the relationship between the two flow rates. As the two flows meet, they push the mobile phase toward the accumulation wall, creating a third, transverse flow known as the focus flow, which exits through the crossflow tube. This focus flow generates a hydrodynamic field that pushes the analytes toward the accumulation wall, where they arrange themselves in a specific distribution (Equation 1) and reach an equilibrium state called *relaxation*. This phase is extremely important to let all the injected sample start the elution from the same point in the channel and therefore to improve the separation and resolution achievable by the device [148]. It is also worth noticing that during this step all the sample components smaller than the membrane pores will be filtered out form the channel and will not reach the detectors.

Elution: A single longitudinal flow of the mobile phase is generated by the pump and enters the channel. Inside the channel, this flow is split into two components: one, the crossflow, creates a hydrodynamic field that pushes the analytes toward the accumulation wall based on their size and mass, allowing for their separation. The other one, the longitudinal flow, carries the analytes toward the channel exit, each at its own speed and, consequently, with its own retention time.

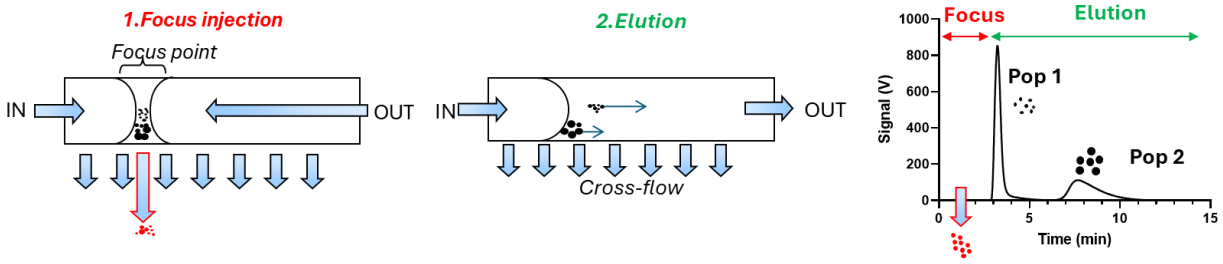

Figure 1.6. Schematization of the steps of a separative injection and of their connection to the analytical output.

FIA

FIA is a non-separative analysis characterized by the absence of a focusing step and a separative force. Here, the sample is injected in flow during the elution step and carried quantitatively to the detectors. The signal is associated to the whole sample content.

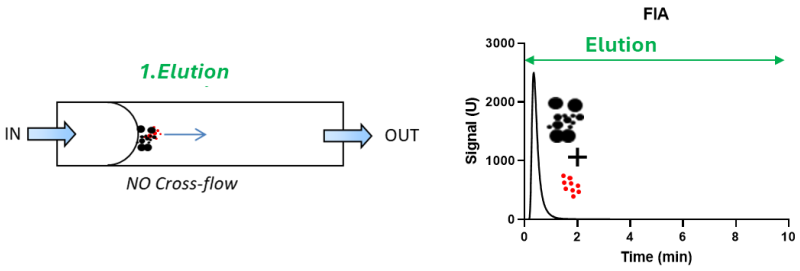

Figure 1.7. Schematization of a FIA injection and its analytical output.

FFIA

FFIA is a non-separative analysis analogous to a FIA but characterized by an initial focusing of the sample, which acts as filtration step for the species smaller than the membrane cut-off. The analysis minimizes the interactions of the sample with the membrane while providing filtration of the smaller species. The resulting signal is associated to the colloidal content of the sample, which is bigger than the membrane cut-off and did not permanently interact with the membrane during the focusing step.

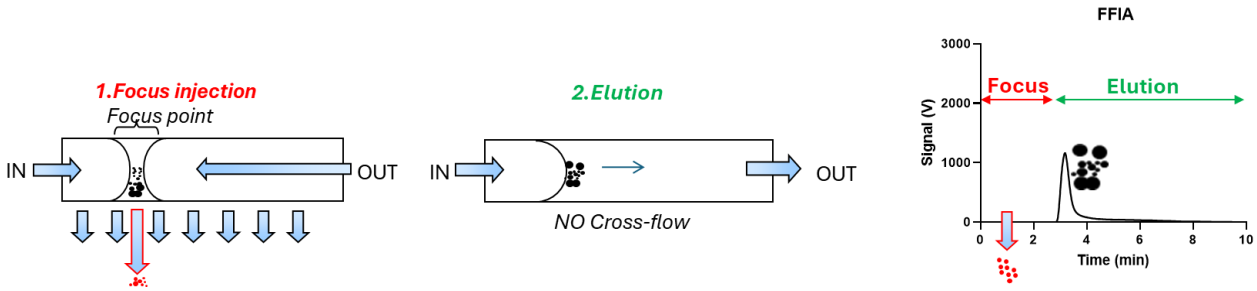

Figure 1.8. Schematization of the steps of a FFIA injection and of their connection to the analytical output.

Analysis optimization

The outstanding flexibility of AF4 platforms comes with an intrinsic disadvantage: the necessity to optimize multiple parameters to achieve a good, reliable and reproducible separation on the sample components. In the following paragraphs some of the main aspects which need to be considered and optimized during the method development will be discussed.

Membrane. The membrane choice should consider two key aspects: pore size (or cutoff) and the membrane material. The pore size defines the smallest species that will be retained in the channel during the focusing phase. Meanwhile, the material of the membrane directly impacts the stability of the sample within the separation channel. Selecting the correct membrane is essential, as different materials exhibit varying surface charges, which affect sample interactions, retention time, and size evaluation. Common materials include regenerated cellulose (RC), cellulose triacetate (TCA), and polyether sulfone (PES), with RC and PES being the most frequently used, providing molecular weight cutoffs (MWCO) ranging from 3 to 100 kDa. The ideal membrane for an experiment should be stable with respect to the mobile phase, minimize interactions with the sample to avoid adhesion to the channel, and have sufficiently small pores to ensure retention of the species of interest. The sample recovery rate serves as a key criterion when selecting the membrane (as well the mobile phase), as sample loss during the focus/injection and elution phases is inevitable. The parameter is conventionally expressed as:

$$R_{\%} = \frac{A_{SI}}{A_{FIA}} \times 100$$

Equation 16. $R_{\%}$: Recovery. A: Integration area of the concentration signal (often stemming from an UV detector) associated to a SI and FIA injection of the same amount of sample.

The current ISO guideline (ISO/TS 21362:2018) requires a $R_{\%} \geq 70\%$ for method validation. During method development $R_{\%}$ can also be rapidly estimated as the ratio between the FFIA and FIA signal.

Mobile phase composition. AF4 offers great flexibility in mobile phase composition, allowing researchers to match the mobile phase closely to the sample matrix or target environments. This approach enables the analysis to take place under native-like conditions, producing results that are as representative as possible of the real sample. The mobile phase should reflect the composition of the sample environment to avoid sample alterations and obtain representative results. However, this approach is not always directly applicable, particularly when studying samples in environments where they may be unstable (e.g., biological fluids). In such cases, compromise conditions in terms of ionic strength and pH are often required. These factors directly affect sample-membrane interactions, retention time, and sample stability in the channel. For example,

higher ionic strength compresses the electrical double-layer (EDL) which may lead to NP adhesion to the membrane and reduced recovery. On the other hand, low ionic strengths maximize the electrostatic repulsion which could cause early elution and loss of separation (Figure 1.9). Careful adjustment of these parameters ensures a balance of electrostatic repulsion and therefore the possibility to achieve optimal recoveries and separation extent.

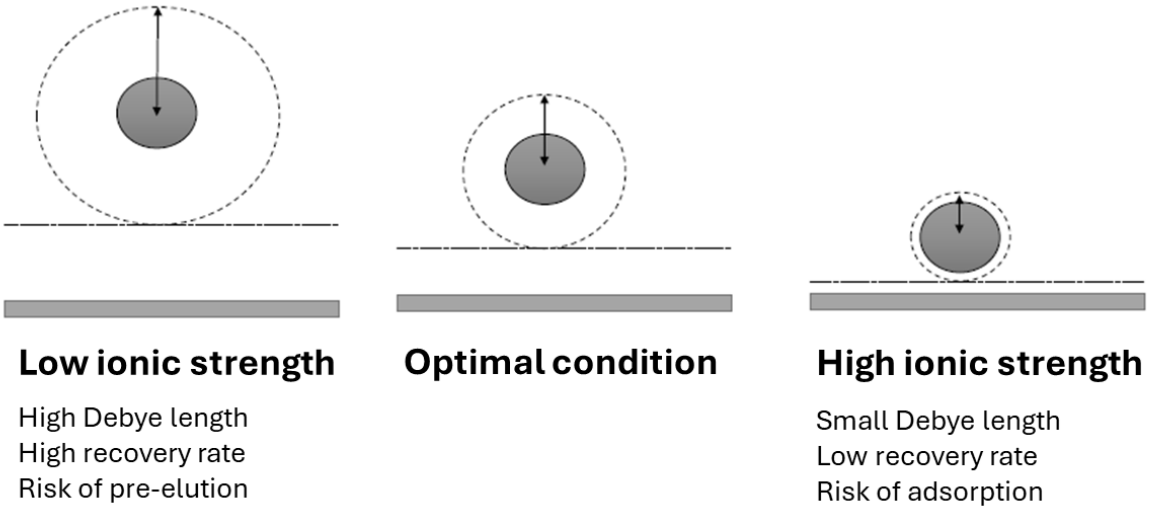

Figure 1.9. Schematization of the impact of the ionic strength on the AF4 separation.

If ionic strength or pH adjustments do not yield optimal separation and recovery, surfactants like SDS or Tween can improve efficiency, especially for mixed nanoparticle samples. Antibacterial agents, such as sodium azide, may also be introduced in biological samples to prevent contamination. Typically, electrolyte systems are chosen to maintain appropriate pH and ionic strength, with additives used as needed to ensure accuracy and stability, although at cost of reduced method "nativeness" and sustainability.

Spacer length, height (w) and crossflow program. Channel length usually varies between 70 and 300 mm. Shorter channel provide shorter analysis time, better LoD but worse fractionation [149]. The channel thickness greatly influences particle retention time, as discussed in Table 1.11.

High channel thickness	Small channel thickness
- Higher sample dilution	- Less sample dilution
- Higher peak broadening	- Thinner peak width
- Better fractionation/resolution	- Reduced selectivity
- Increase the time of analysis	- Reduced analysis time

Table 1.11. Schematization of the effect of channel thickness on AF4 separation.

Collective experimental knowledge has empirically let emerge a 350μm-thick spacer as the optimal and therefore more widely used spacer for the analysis of nano-objects. The impact of the channel flow and crossflow on the sample separation is easily understandable from the previous sections. In general, the crossflow intensity is modulated during the analysis to optimize analysis time, peak resolution (R_s) and sample recovery. The current ISO guideline (ISO/TS 21362:2018) requires a $R_s > 1.5$ for method validation.

Focusing time. Focusing time is a key parameter in AF4 optimization. If it is too short, the sample equilibrium layer spreads too widely, leading to some elution within the void peak. If it is too long, increased interactions can cause aggregation and excessive retention. Focusing time is influenced by the sample diffusion coefficient (D) and channel height (w). Thicker channels or low-D samples benefit from longer times for better equilibration. For dilute samples, extended focusing improves detection by allowing the injection of higher sample volume. Researchers typically adjust focusing time experimentally to balance resolution, separation efficiency, and recovery. Moon et al. [150] have proposed a relationship for the minimal relaxation time associated to the focusing step (Equation 17)

$$\tau = 1.2\frac{V^0}{V_c}$$

Equation 17. τ: minimal relaxation time (min). V^0: channel volume (mL). V_c: the volumetric crossflow rate (mL/min).

1.3.5 Online detection

The true potential of an AF4 platform lies not only in its separation capabilities and being an absolute method but also in its ability to be coupled with various detectors that provide multiparametric information on the separated species. Table 1.12 provides a brief overview of the most common detectors that can be coupled online with an AF4 platform. The detectors exploited in this work will be discussed more deeply below.

Detector	Features
UV/Vis; DAD	• Spectroscopical characterization • Concentration detector • Studies on evolving system (drug loading and releasing, conjugation…) • Versatile signal (aspecific)
FLD	• Spectroscopical characterization • Studies on evolving system (drug loading and releasing, conjugation…) • Very selective signal (quite specific) • Stable signal less prone to drifts and interference
Raman micro-spectroscopy	• Spectroscopic characterization • Extremely selective signal • No quantitative information • Low detection threshold
dRI	• Concentration detector • Unstable signal significantly affected by pressure changes • Universal signal
MALS	• Requires concentration signal • Accurate determination of molecular weight/molar mass, radius of gyration (Rg) and fractal radius (δ) • Information on the aggregation rate of nanosystems • Information of the shape of NPs (conformation plot) • Working size range(1 nm-100 μm)
DLS	• Determination of hydrodynamic radius (R_h) • Estimation of the shape factor (Rg/R_h) • Working size range (1 nm-100 μm)
ICP-MS	• Studies on evolving system by monitoring elemental composition • Low detection limit (ng/L)
High-Resolution MS	• Accurate information on molar mass of molecules and complex • Evaluation of loading processes inside nanosystems (e.g. Liposomal carriers)

Table 1.12. Main features provided by the most common detectors online coupled with FFF techniques. Adapted from [117].

UV and DAD

The most used detector in FFF systems is the UV/Vis spectrophotometer due to its simplicity, availability, and low cost. These spectrophotometers are typically designed as absorption detectors for chromatographic systems, featuring very low internal volumes to minimize band broadening. Basic models operate at a single wavelength, while more advanced instruments allow for the detection wavelength to be adjusted to match analyte spectral properties. The detection wavelength is generally selected to maximize sensitivity to the analyte while avoiding interferences, such as absorption by the carrier liquid. Diode array detector (DAD) can capture the entire UV/Vis spectrum of eluting samples, which is useful when the chemical composition of the sample changes during separation or to confirm its consistency. These spectra can also detect changes in some physical properties of the sample [151]. For dissolved samples with uniform chemical composition, absorption is directly proportional to concentration. However, for particulate material, corrections may be required to account for the effect of particle size on the detector signal [152]. Since these instruments are not optimized for particulate samples, the signal they produce is a combination of light scattering and absorption, making particle quantification more challenging. The UV signal often reflects a turbidimetric measure [153], and sensitivity to forward-scattered light may lead to an underestimation of larger particles, especially when their size is comparable to the incident wavelength.

dRI

This detector operates by continuously measuring the difference in refractive index (n) between the sample passing through a flow cell and the eluant in a reference cell. If dn/dc is known for the analyte in the experimental environment (usually determined through calibration), dRI signal can be directly linked to sample concentration. In a typical FFF-multidetector platform, this detector is used as a "concentration" information source for MALS calculations, either with or without a UV/Vis detector. Compared to UV/Vis detectors, dRI detector is more challenging to handle due to its lower sensitivity and greater susceptibility to signal fluctuations caused by flow and temperature changes. However, unlike the extinction coefficient, dn/dc remains relatively constant across different wavelengths and sample of the same “nature” (e.g. proteins typically have dn/dc raging between 0.185-0.195 mL/g). The dRI detector is typically preferred for substances like

polysaccharides, which absorb UV/Vis light weakly and whose response can be significantly affected by light scattering [154].

Fluorescence detector (FLD)

FLD is another commonly used detector. Its high selectivity, based on the excitation and emission process at specific wavelengths, makes it ideal for detecting certain organic compounds. Additionally, the FLD offers high sensitivity, which can be adjusted by regulating the excitation intensity, and strong stability, making it resistant to drifts caused by pressure or flow changes. When coupled online with AF4, the FLD can be used to detect fluorescent components in samples, ranging from proteins to fluorescent dyes for targeted recognition [155].

Multi Angle Light Scattering (MALS)

Scattering is an optical phenomenon in which part of the radiation deviates from its path when it encounters a discontinuity in the propagation medium. In a colloidal system, NPs in suspension can be considered as discontinuities (and thus scattering elements) relative to the medium in which they are immersed and through which the light propagates. Models that describe scattering can be divided into three categories based on the relationship between the wavelength of the radiation and the size of the particles. Specifically, a parameter $\alpha = \pi d_p/\lambda$ is defined, where d_p represents the particle diameter and λ the wavelength of the incident radiation. The ideal model to describe a given scattering phenomenon depends on the value of α:

- $\alpha < 1$: Rayleigh scattering (particles much smaller than the wavelength)
- $\alpha \approx 1$: Mie scattering (particles of similar size to the wavelength)
- $\alpha > 1$: Geometrical scattering/diffraction (particles larger than the wavelength)

Light scattering (LS) techniques, such as MALS and DLS, are non-destructive methods for characterizing macromolecules and a wide range of particles in dispersion. These techniques are considered absolute because they do not require external calibration standards. However, their accuracy may be limited when dealing with samples that have complex, multimodal size distributions. Coupling light scattering techniques with size-based separation methods, like AF4, can improve size analysis of complex samples. This is because size-separation reduces sample complexity before analysis, enabling more precise sizing of narrowly distributed sample fractions.

MALS is a characterization technique that determines Mass (M), Gyration Radius (Rg or r_g) and PSD of the analytes by collecting light scattered by particles in suspension at different angles. If sample concentration and specific refractive index increment (dn/dc) are measured or known, MALS can measure MW without reference to calibration [156]. Since the knowledge of dn/dc and concentration of the sample are required for the determination of Rg and M respectively, a typical experiment involving AF4, and MALS see the platform often coupled also to a dRI or UV detector. MALS detection is applicable in a size range from 1 nm to over 1 μm, but its sensitivity decreases with decreasing particle size.

When a wave encounters a scattering element (a macromolecule, a particle ecc.), part of the wave energy is deflected in various directions through a process of absorption and emission, resulting from the interaction between the radiation and the oscillating dipole moment of the scattering element (SE). Most of the emitted radiation retains the same energy as the incident wave (elastic scattering), and this component is recorded by the MALS detector and used to calculate the relevant parameters. Structurally, the detector consists of a polarized, isotropic radiation source (a laser) that strikes the sample, generating the scattering phenomenon. The intensity of the scattered light is measured by a series of detectors positioned at precisely defined angles. The intensity of the scattered light is proportional to the SE concentration and its refractive index (n), which is related to polarizability (Equation 18.).

$$I_s \propto c\left(\frac{dn}{dc}\right)^2$$

Equation 18. I_s: Intensity of the scattered light. c: concentration of SE.

If the scattering elements (SEs) are not independent of each other (for example, when particles are composed of multiple SEs or when SEs are subjected to a force field that influences particle movement), it can be shown [157] that *Is* also depends on the mass of the scattering species (Equation 19)

$$I_s \propto cM\left(\frac{dn}{dc}\right)^2$$

Equation 19. M: mass of the scattering species

When α << 1 the SE can be considered point-like. For those particles, scattered light intensity is independent from the observation angle θ (isotropic scattering).

In the case of scattering of larger particle ($\lambda/20 < r_g < 400$ nm…1μm, depending on structure), the particle can be assumed to consist of multiple independent SEs based on the Rayleigh-Gans-Debye (RGD) theory [157]. If the distance between these SEs is comparable to the wavelength (λ), phase interactions will vary at different angles. This leads to constructive and destructive interference, resulting in a scattering profile that depends on the angle (θ), with the maximum occurring at θ=0. Mathematically, the relationship between θ and the scattered intensity (Is) is described by the attenuation factor P(θ) (Equation 20).

$$I_s \propto cM\left(\frac{dn}{dc}\right)^2 P(\theta)$$

Equation 20. *P(θ)*: attenuation factor

From RGD theory it is possible to obtain the fundamental equation (Equation 21) according to which MALS instrumentations operate:

$$\frac{k^* c}{R(\theta)} = \frac{1}{MP(\theta)} + 2A_2 c$$

Equation 21.

Were

- *R(θ)*: Rayleigh ratio, the ratio between the intensities of diffused and incident light
- *c:* particle concentration
- A_2: hydrodynamic terms which considers the solvent-solute interactions
- $k^* = \frac{4\pi^2 n_0^2}{N_A \lambda_0^4}\left(\frac{dn}{dc}\right)^2$
- $P(\theta) = 1 - \frac{16\pi^2 n_0^2}{3\lambda_0^2}\sin^2\left(\frac{\theta}{2}\right)\langle r_g^2\rangle + \cdots$
- n_0: refractive index of the solvent
- N_A: Avogadro number
- λ_0: wavelength of the incident radiation

- $k^* = \frac{4\pi^2 n_0^2}{N_A \lambda_0^4}\left(\frac{dn}{dc}\right)^2$
- $\langle r_g \rangle$: root mean square (RMS) radius, the measure of size weighted by the mass distribution about the center of mass, often called "radius of gyration" or *Rg*. However, radius of gyration is a misnomer, since it describes a kinematic measure of a molecule rotating about a particular axis in space.
- $\langle r_g^2 \rangle = \frac{\sum r_i^2 m_i}{m}$

By substituting each term in Equation 21 and considering the term A_2 negligible (low sample concentration), it is possible to obtain the explicit form of the equation for dilute systems (Equation 22.):

$$\frac{k^* c}{R(\theta)} = \frac{1}{M} + \frac{16\pi^2 n_0^2}{3M\lambda_0^4}\sin^2\left(\frac{\theta}{2}\right)\langle r_g^2 \rangle$$

Equation 22.

A straightforward solution of the equation is not possible since it is not experimentally possible to measure the scattered light intensity neither at θ=0° (because of the presence of transmitted light) nor at c=0, because light intensity depends on particle concentration. Therefore, *Rg* and *M* are determined by extrapolation from the measures of the intensities of the scattered light at different angles and for different particle concentrations. The commercial software used to elaborate data offers different algorithms by which one can estimate the molar mass values. Each algorithm corresponds to a different mode of solving Equation 20. Some of the most common algorithms are reported below:

- Debye fitting: it builds a plot $\frac{R(\theta)}{k^* c}$ vs $\sin^2\left(\frac{\theta}{2}\right)$, and it calculates a polynomial regression at a chosen order; it has good results for a wide range of *M*.

- Zimm fitting: it builds a plot $\frac{k^* c}{R(\theta)}$ vs $\sin^2\left(\frac{\theta}{2}\right)$, and it calculates a polynomial regression at a chosen order; it is the most common fitting algorithm.

- Berry fitting: it builds a plot $\sqrt{\frac{k^* c}{R(\theta)}}$ vs $\sin^2\left(\frac{\theta}{2}\right)$, and it calculates a polynomial regression at a chosen order; it is the most indicated for the determination of high molar mass values.

When the term A_2 is not negligible it is still possible to evaluate *Rg* and *M* as well as A_2 using fitting strategies characterized by different approximation of Equation 20.

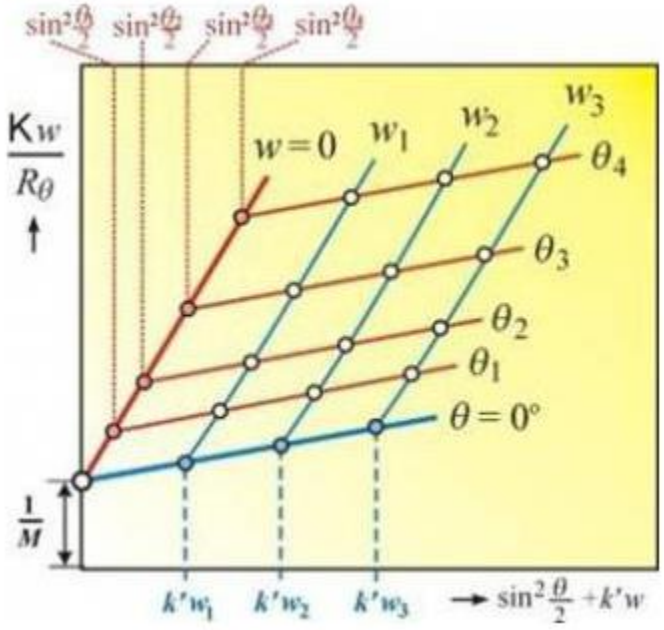

Figure 1.10. General graphical representation of a Zimm plot.

M and *Rg*, in addition to their intrinsic significance when they are considered individually, can offer further insights when analyzed together. By plotting log *Rg* vs. log *M* distributions a *conformation plot* is obtained. It helps in the understanding of the structural organization of the particles, e.g. if they are compact, elongated, or branched. The slope "v" (v-value) in fact provides information about the shape of the particles. For a solid sphere, the v-value is approximately 0.33, while higher values represent elongated or deformed structures (e.g., a rod has a v-value around 1, and a random coil around 0.7). Lower values indicate a denser core with a softer shell.

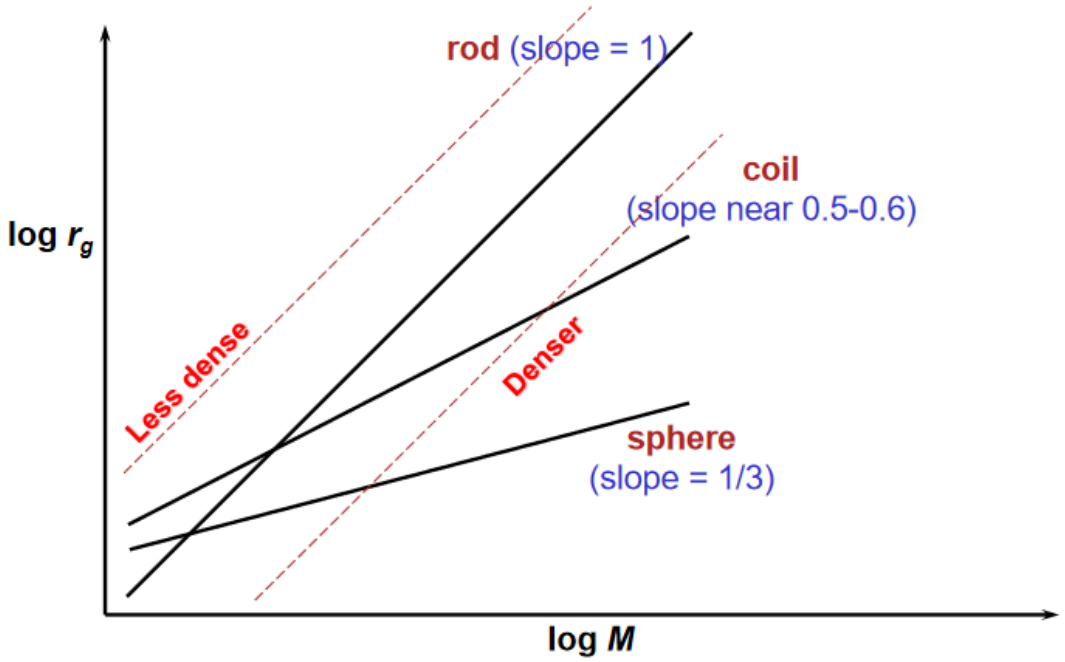

Figure 1.11. Schematization of a conformation plot and characteristic slopes for certain nanoparticle geometries.

1.3.6 Offline detection

Online coupling of detectors with AF4 instrumentation offers the fastest and most straightforward approach for multiparametric analysis after the AF4 separation. However, to achieve a more detailed characterization of complex samples, offline techniques are often necessary in addition/complement to online characterization. The workflow typically involves collecting the separated sample fractions, which may need additional pretreatment steps (such as concentration) before analysis. Figure 1.12 illustrates the operational phases of these platforms, and it lists most common offline techniques used with AF4.

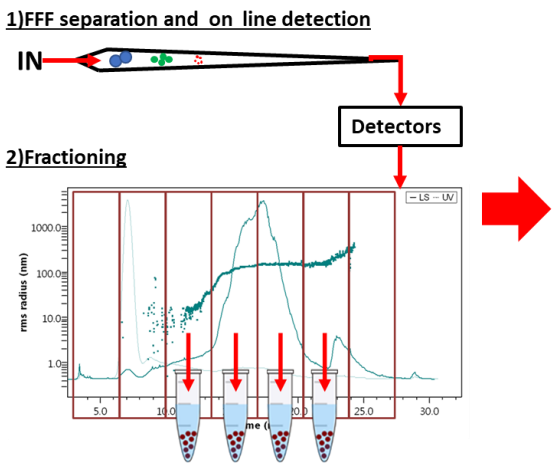

3)Off line detection

Technique	Why?
TEM/SEM imaging	Further size/shape characterization
Zetasizer	Conductivity, electrophoretic mobility, static light scattering, and dynamic light scattering studies
NTA	Further size characterization (hydrodynamic size)
SDS-PAGE	Control of separation reproducibility, protein separation
Western Blot	Targeted recognition of certain proteins trough antibody recognition
mUHPLC-ESI-MS/MS	Protein, lipid, N-glican, lipoprotein and nucleic material fractions profiling
DLS	Further size characterization (hydrodynamic size)

Figure 1.12. Schematization of a typical workflow involving the offline coupling of an FFF platform to other techniques. The sample is firstly separated in the FFF channel, the separated species are collected in fractions at the end of the device and sent to offline analysis. Image from [117].

A second FFF separation of the fractions collected from an initial analysis can also be considered as a specialized type of offline coupling used to enhance the separation of complex samples[158]. This process is labour-intensive, often requiring a reconcentration step before the second run. The HF5 system is particularly suited for this purpose because its small channel volume and low flow rates minimize dilution and reduce the volume of collected fractions. Additionally, the focus step helps to reconcentrate the injected species therefore minimizing the increase of sample dilution between the first and the second separation.

The main offline detectors used in the studies covered in this work, either following AF4 or as complementary techniques, will be discussed in more detail below.

SEM and energy-dispersive X-ray spectroscopy (EDX)

In SEM, a fine beam of medium-energy electrons (5-50 keV) is scanned across the sample in a series of parallel tracks. These electrons interact with the sample, producing secondary electron emission (SEE), back-scattered electrons (BSE), cathodoluminescence, and X-rays. The generated signals, collected by specific detectors, provide different types of information about the sample [159]. For example:

SEE. These electrons are emitted when a primary electron beam strikes the sample, causing low-energy electrons to be released from the surface. They enable the acquisition of high-resolution images of the surface morphology.

BSE. Back-scattered electrons have an energy like the primary beam and are generated when the beam electrons are deflected backward by the atomic nuclei of the sample. BSE images highlight differences in the chemical composition of the sample, as elements with a higher atomic number deflect more electrons, producing brighter areas in the image.

Light Cathodoluminescence. Cathodoluminescence occurs when the electron beam excites electrons in the material, which then release energy as visible light. These images provide information about the optical properties and structural defects of the materials, particularly in minerals and semiconductors.

X-rays (for EDX). X-rays are generated when beam electrons eject inner-shell electrons from the atoms of the sample, and outer-shell electrons fall to fill the vacancies. X-ray analysis, known as X-ray microanalysis or energy-dispersive EDX, provides information about the elemental composition of the sample.

The signals collected by the detectors are converted into electrical signals representing the intensity of the generated signal at each scanning point. The SEM image is constructed point by point, like the functioning of an old cathode-ray tube (CRT). As the electron beam scans across the sample, a surface map is produced based on the intensity of the emitted signals. The final image is displayed on a grayscale screen, where the brightness of each point corresponds to the signal intensity collected at that specific point on the sample. SEM images have very high resolution (down to a few nanometers), allowing the observation of fine surface details of the sample.

TEM

TEM involves an high-energy electron beam (typically 100-300 keV) which, focused through appropriate magnetic lenses, hits a thin layer of sample (about 100 nm or less in thickness) [160]. The electrons interact with the atoms of the sample, resulting in scattering. After passing through the sample, the unscattered and scattered electrons form an image on a detector, such as a phosphor screen or a CCD camera. The image is formed based on electron density and phase contrast, giving extremely high-resolution images. TEM provides detailed internal structures with very high

resolution (down to about 0.1 nm or less). This is because the wavelength of the electron beam is much shorter than that of visible light. Unlike SEM, which is used to study the surface morphology, TEM is used to visualize the internal microstructure if the samples. High-Angle Annular Dark Field Scanning TEM (HAADF-STEM) is a variant which generates images particularly sensitive to the atomic number of the elements present (Z contrast), with heavier atoms appearing brighter.

DLS

The DLS technique allows for the evaluation of dynamics and dimensionality of a nanoparticle system in solution. The system uses a polarized and monochromatic light source (laser) and evaluates over time how the interference pattern changes as a result of the Brownian motion of particles [161]. This evaluation is done through an autocorrelation function that can be defined in its most general form as follows:

$$G_2(\tau) = A(1 + Be^{-2\Gamma\tau})$$

Equation 23.

Where:

- $G_2(\tau)$: autocorrelation factor.
- τ: time interval from the first evaluation of the scattering profile (which serves as a reference for the autocorrelation).
- *A* and *B*: experimental constants dependent on the nature of the sample, the instrument and the used wavelength.
- Γ: time constant of autocorrelation decay. The larger this constant, the faster the system loses autocorrelation. This is because nanoparticle have faster diffusion due a smaller hydrodynamic radius (see Stokes-Einstein equation). Γ is defined as follows $\Gamma = Dq^2$
- *D*: hydrodynamic diffusion coefficient as described by the Stokes-Einstein equation.
- *q:* vector of the scattering module. q is defined as follow: $q = \frac{4\pi n^2}{\lambda_0} \sin\left(\frac{\theta}{2}\right)$

The instrumental device, following scattering measurements at the preset angle θ, returns the autocorrelation function (Equation 23.) and, through an analysis using the cumulant coefficient method, allows to obtain the hydrodynamic diameter via *D*.

Typically, DLS does not provide direct information about the shape of NPs, as it indeed returns an equivalent diameter corresponding to the size of a sphere that behaves identically to the sample under examination. For non-spherical NPs, their actual size is therefore significantly different from Rh: this makes a preliminary shape evaluation important. Moreover, due to the high dependence of scattering intensity on size, sample size information is usually biased toward larger particles: this is the reason for which DLS size information is usually larger than that provided by TEM and Atomic Force Microscopy (AFM) [161]. Additionally, considering the batch nature of the technique, high sample purity and low polydispersity are required to obtain accurate results. Electrophoretic light scattering (ELS) can be combined to measure the velocity of particles in an applied electric field, thus monitoring the z-potential, which provides more surface modification information [162].

X-ray diffraction (XRD)

XRD is a key non-destructive technique for analyzing crystalline materials. It reveals structural information like crystal phases, orientations, grain size, crystallinity, and defects. Peaks in XRD patterns arise from the constructive interference of monochromatic X-rays scattered by lattice planes at specific angles. The pattern reflects the atomic arrangement, serving as a material "fingerprint." The method relies on constructive interference between monochromatic X-rays and a crystal sample. X-rays are generated in a cathode ray tube, filtered, collimated, and directed at the sample. When Bragg's Law is satisfied (Equation 24.), constructive interference occurs, producing a diffracted beam.

$$n\lambda = 2d \sin\theta$$

Equation 24. n: an integer. λ: X-ray wavelength. d: lattice spacing. θ: diffraction angle.

A detector records the intensity and angle of the diffracted X-rays. X-ray diffractometers have three main components: an X-ray tube, a sample holder, and a detector [163]. In a typical X-ray diffractometer, the sample rotates in the X-ray beam path at an angle θ, while the detector rotates at 2θ, collecting the intensity of the reflected X-rays. This instrument, known as a goniometer, ensures precise angle measurements during the scanning process. When Bragg Law is met, constructive interference results an increase in intensity (graphically represented by a peak in the

XRD diffractogram of the species). Materials are identified, typically through comparison of signals with the diffractogram of reference crystalline patterns.

Fourier-transform infrared spectroscopy (FT-IR)

When a sample is placed in the optical path of an interferometer in FT-IR, the interference pattern changes due to the selective absorption of specific infrared frequencies. The Fourier transform converts these frequencies into corresponding light intensities, producing a complete infrared spectrum, which provides detailed information about the functional groups of the sample. This allows for the identification of unknown substances, determination of chemical structures, and purity analysis [164]. FT-IR is thus a powerful tool for characterizing the surface functionalization of NPs.

1.3.6 FFF and SEC complementarity

SEC in the most common separation technique for size-based separation of biological nanosystems [165, 166].

SEC separates biomolecules based on their hydrodynamic radius. The stationary phase consists of porous particles with controlled pore size, allowing molecules/particles to diffuse through, depending on size, thanks to a carrier fluid. Unlike separations based on chemical properties, SEC is an entropically driven process, separating molecules by size [167].

In SEC, the thermodynamic retention factor is expressed by Equation 25.

$$\ln K_D = -\frac{\Delta S_0}{R}$$

Equation 25. K_D: thermodynamic retention factor. ΔS_0: the entropy change. R: gas constant.

Temperature indirectly influences elution time by affecting sample conformation and carrier viscosity. The thermodynamic retention factor differs from other chromatographic methods; here, it is the fraction of pore volume accessible to the analyte [168].

Engelhardt suggested the retention factor k^* as the ratio between the sample probability of staying in the stagnant mobile phase within pores and the moving mobile phase between particles also called interstitial volume (Equation 26.) [169].

The maximum k^*_{max} value is determined by the ratio of pore volume (V_P) to interstitial volume (V_Z), or pore porosity (ε_P) to interstitial porosity (ε_Z) (Equation 27.):

$$k^* = \frac{V_{elu} - V_z}{V_z}$$

Equation 26. V_{elu}: total eluent volume

$$k^*_{max} = \frac{V_P}{V_Z} = \frac{\varepsilon_P}{\varepsilon_Z}$$

Equation 27.

This ratio limits the achievable retention range. Using state-of-the-art columns, the maximum retention factor k^*_{max} ~ 1.6–1.8. Increasing packing density or using larger pore volumes can adjust these parameters.

SEC separation enables calibration curves based on analytes with known molecular weights to estimate the weight of unknown samples. Calibration curves typically plot *logM* against retention volume, forming a third-order polynomial with a linear region in which the best resolution and accuracy are achieved [168]. Larger species, excluded from the pores, elute first, with smaller species following in a size order. However, sample shape (e.g., globular, rod-like) and non-ideal adsorption can introduce calibration errors [170-172].

The slope of the linear portion of the calibration curve measures selectivity:

$$log\ M = m \cdot K_D + b$$

Equation 28.

Reducing analysis time is a priority in modern SEC. The analysis time is mainly determined by the mobile phase flow rate since all the analytes are eluted before the total void volume [173]. Shorter column lengths and higher flow rates are effective strategies for fast SEC analysis [173], though shorter columns reduce theoretical plates. Popovici and Schoenmakers studied the impact of particle size, column length, and flow rate on SEC separation [174, 175]. Mass transfer between the interstitial and pore spaces is a challenge, particularly for large solutes [175]. Temperature increases mass transfer rate by reducing viscosity and improving analyte diffusivity. Park et al.

demonstrated fast SEC separations at 110°C [173]. Small particles, short columns, and high temperatures can significantly shorten the analysis time.

Today, particles of 3–20 μm with varying pore sizes are used [167], and most columns are 30 cm long with an internal diameter of 4.6–8 mm. Analysis time for conventional columns ranges between 15 and 50 min. For high-resolution separations, longer columns or multiple columns in series are required for complex samples.

A recurring theme in FFF studies is the replacement of SEC-MD with FFF-MD (especially AF4), due to the limitations of SEC and the benefits of FFF. SEC has a limited size resolution range (up to 10^7 Da, ~100 nm), and its stationary phase can cause sample aggregation and restrict mobile phase compatibility. Additionally, adsorption and/or dissociation can occur due to sample interaction with the stationary phase [176]. In contrast, FFF offers a wider dynamic range, and the absence of a stationary phase avoids these constraints: this allows to work in native conditions [123, 177].

1.4 Applications of AF4 in nanomedicine: state of the art

The previous sections of this work have outlined the features of AF4, its role in characterizing nanosystems, and its significance in determining CQAs for market approval. This paragraph aims to present examples of using AF4 for analyzing NPs of biomedical interest. To facilitate reading, nanosystems are categorized into Engineered NPs (ENPs) and Naturally Occurring NPs (NNPs). ENPs include metallic, metal-oxide, and polymeric NPs, while NNPs comprehend biopolymers, dissolved organic matter, and colloidal inorganic species.

ENPs. The standard configuration for characterizing ENPs, assessing their stability, and analyzing their behavior in complex media consists of an AF4 system coupled with a MALS and at least one concentration detector, though AF4-DLS platforms are also used [178]. This configuration is straightforward, non-destructive, and versatile, making it suitable for a broad range of ENPs, including gold and silver NPs [93, 179, 180], metal oxides (e.g., ZnO) [181], MOFs [182], fullerenes [183], quantum dots [184], nanoplastics [185, 186], and PDA nanosystems [187]. AF4-ICP-MS is frequently used for a more detailed characterization of these systems. Despite being

more expensive and destructive, this platform provides in-depth analysis by detecting even trace amounts (ppb) of metals, making it ideal for examining metal-based ENPs [188-192]. It also allows for evaluating the stoichiometry of metal-ligand complexes (e.g., peptides, immunoglobulins) [155, 193-195]. HF5 platforms have been employed to monitor ENP synthesis [187], size [196-198], stability [199], and interactions with other components [200, 201].

NNPs. AF4 studies are reported on common organic nanosystems such as poly(lactide) (PLA) and poly(lactide-co-glycolide) (PLGA) NPs [202, 203], dendrimers [204], and glycopolymers [205]. Nanogels, which are colloidal particles with solvated, crosslinked polymeric networks, represent an intriguing category of organic nanomaterials [206]. They are highly sensitive to stimuli and degradable. Nanogels typically undergo a deswelling transition near body temperature, making them suitable for potentially traceless drug delivery systems [207]. They also facilitate the triggered release of macromolecules [208]. Poly(N-isopropylacrylamide) (pNIPAM), a common nanogel, was first characterized using AF4 by Smith et al. [209], and Niezabitowska et al. investigated the impact of the synthesis protocol on its internal structure [210]. AF4 was also used to monitor pNIPAM degradation [209] and to separate the nanogel from its degradation products, demonstrating AF4 capability as a purification and QC step before clinical application [211, 212].

1.5 Overview of the research

This research seeks to explore the possibilities of AF4 combined with multi-detection to assist the characterization and monitoring of various NMs during the various stages of clinical development. To cover most of the possibilities of AF4 in the widespread and heterogeneous word of NMs characterization, this work contains four thematic chapters each one focusing on NMs of different nature and complexity as well highlighting distinct roles played by AF4 characterization during their development. Each section is based on a different scientific article that I have published during my three years of PhD studies. A brief overview of those chapters is reported below.

Chapter 2. AF4 as a tool to unveil the relationship between different nanoforms.

This study focused on a PDA nanosystems. PDA, a melanin-like biomimetic material, is increasingly employed in multiple fields such as photodynamic therapy and drug delivery, due to

its excellent biocompatibility, degradability, simple preparation, and efficient photothermal conversion. However, despite its widespread applications, the relationship between its properties and diverse chemical structures remains largely unexplored. Additionally, the simultaneous formation of multiple PDA species during synthesis is often overlooked hindering their full application in clinical settings. HF5 was used in combination with UV/Vis, FLD, and MALS. By monitoring the progression of a common PDA synthesis over time, we gained insights into the reaction kinetics and identified two distinct species formed independently at varying rates during dopamine oxidation and self-polymerization. Although these species exhibited similar UV absorption spectra, they displayed different emission characteristics. The first species (PDA-Ps), which eluted earlier, exhibited a coiled polymeric structure with lower molar mass and hydrodynamic radius compared to size standards under similar conditions. The second species consisted of monodisperse solid spherical NPs (PDA-NPs) with a molar mass of two orders of magnitude higher than the first species, forming a stable supramolecular system with a defined radius, while the first lacked 3D structural organization. These findings represent a significant breakthrough in understanding the relationship between different PDA nanoforms, as no prior experimental technique has been able to separate the various dopamine polymerization products in real time. The HF5 platform, with its rapid and unique capacity for detailed analysis therefore emerges as a highly effective tool for selecting the optimal PDA nanoforms for clinical development.

Reference article: Mavridi-Printezi, A., **Giordani, S**., Menichetti, A., Mordini, D., Zattoni, A., Roda, B., Ferrazzano, L., Reschiglian, P., Marassi, M., Montalti, M. & Montalti, M. (2024). The dual nature of biomimetic melanin. Nanoscale, 16(1), 299-308.

Chapter 3. AF4 as an *all-in-one* platform for synthesis monitoring, characterization and purification of antimicrobial NPs.

Advances in nanotechnology have created new opportunities in nanomedicine, particularly through the development of composite nanomaterials aimed at combating the growing issue of bacterial drug resistance. Among these, nanosilver-based antimicrobials show promise for treating bacterial infections. PDA is an attractive biocompatible carrier for nanosilver; however, the synthesis and functionalization of Ag-PDA NPs are complex, often requiring time-consuming purification processes. Post-synthesis treatments can compromise the stability and practicality of

the material, and traditional offline characterization methods are both slow and unrepresentative of real-world conditions. Preparation optimization, purification, and characterization of Ag-PDA is therefore essential for the safe and effective development of these nanomaterials. Building on previous research into PDA nanosystems, a comprehensive approach utilizing HF5, multi-angle light scattering, and spectrophotometric detection has been applied to improve the synthesis and QC of Ag-PDA NPs. This tailored method was able to monitor particle growth in a TLC-like manner, characterize the resulting species, and isolate purified Ag-PDA NPs. These NPs demonstrated biological activity as antibacterial agents while achieving fast analysis times and employing eco-friendly, cost-effective carriers such as water.

Reference article: Marassi, V., Casolari, S., Panzavolta, S., Bonvicini, F., Gentilomi, G. A., **Giordani, S.**, Zattoni, A., Reschiglian, P. & Roda, B. (2022). Synthesis Monitoring, Characterization and Cleanup of AgPolydopamine Nanoparticles Used as Antibacterial Agents with Field-Flow Fractionation. Antibiotics, 11(3), 358.

Chapter 4. AF4 as a tool to predict the behavior and stability of nanomedicines in biological environments.

The assessment of stability and toxicity of NMs in relevant environments is one of the most complex and critical steps on the path to commercial approval. Studies examining the stability of magnetic MNPs in biological matrices and the formation and evolution of the protein corona are typically conducted using batch sizing and imaging tools. While these methods can indicate if NPs undergo changes, they provide only averaged results, lacking the ability to track the evolution of individual populations. This is a significant limitation, given the complexity of the matrices and the fact that nanoparticle samples are not always as narrowly dispersed as presumed. This study focused on Fe_3O_4 MNPs coated with PEG/PLGA (PP-MNPs) for drug delivery applications. The stability and behavior of PP-MNPs were analyzed using an HF5 platform in the presence of increasing amounts of human serum albumin (HSA) to simulate the early stages of intravenous administration. In particular, after an initial characterization of the particles, changes in size and z-potential of the PP-MNPs were monitored by titration with HSA at four different concentrations. The experiment was then translated to a dynamic mode using a specially designed HF5 multi-detection method, which allowed us to observe the behavior of PP-MNPs as the HSA concentration increased, and thereby simulate the initial moments of administration. This platform enabled the separation of NPs-HSA conjugates from other components and provided simultaneous

characterization of each separated species using spectroscopy and laser scattering (molecular weight and gyration radius). Additionally, the calculation of v-values revealed valuable information about the morphologies of PP-MNPs and their conjugates, which elucidated the mechanisms by which HSA binds to PP-MNPs and addressed key safety concerns.

Reference article: Marassi, V., Zanoni, I., Ortelli, S., **Giordani, S**., Reschiglian, P., Roda, B., Zattoni, A., Ravagli, C., Cappiello, L., Baldi, G., Costa, A. L., & Blosi, M. (2022). Native study of the behaviour of magnetite NPs for hyperthermia treatment during the initial moments of intravenous administration. Pharmaceutics, 14(12), 2810.

Chapter 5. AF4 as a quality control (QC) system for the commercialization of peptide-based formulations

Aggregation is one of the most crucial factors influencing the pharmacological efficacy and safety profile of peptide-based Active Pharmaceutical Ingredients (APIs). Therefore, accurate determination of the aggregation state of peptide drugs is essential, especially when the API is formulated as a ready-to-use solution. To achieve this, it is vital to utilize non-destructive techniques that can effectively replicate the peptide natural environment for reliable analysis. The previous sections mainly described applications of AF4 to the analysis of NMs in the Research and Development (R&D) stage. However, nowadays the technique is also requested by regulatory bodies like FDA and European Medicines Agency (EMA) as an orthogonal approach, to complement SEC data as far as evaluation of the aggregation state of NMs is concerned. To be commercialized as "alternative drugs", newly developed formulation must exhibit the same properties (e.g. aggregation) of the referring drug already commercialized. The kind of study which focused on evaluating the existence of these relationships are called *Sameness studies.* In this study, an AF4 platform, coupled with UV, dRI, FLD, and MALS detectors, was used to comprehensively characterize the aggregation state of Liraglutide, a peptide API used to treat type 2 diabetes and chronic obesity. Previous research suggested that Liraglutide assembles into hexa-octamers in phosphate buffer, but no data on its behavior in the formulation medium had been provided. The flexibility of the AF4 platform allowed for the use of the formulation medium as mobile phase. This achieved truly representative results, excellent recoveries and detectability (LoQ/LoD). This approach distinguished between stable and degraded samples, and detected aggregates up to 10^8 Da when present. The native state of Liraglutide was found to consist of

pentamers with a non-spherical conformation. Complemented by benchmark SEC analyses, the study provided a comprehensive understanding of the aggregation process, including the identification of both covalent and non-covalent aggregates.

Reference article: Marassi, V., Macis, M., **Giordani, S**., Ferrazzano, L., Tolomelli, A., Roda, B., Zattoni, R., Ricci, A., Reschiglian, P. & Cabri, W. (2022). Application of af4-multidetectionto liraglutide in its formulation: Preserving and representing native aggregation. Molecules, 27(17), 5485.

In summary, these studies highlighted the versatility and effectiveness of the AF4 multi-detection platform at the various stages (R&D and QC) of NMs development. The developed methods and the wide array of analyzed samples led to identify AF4 as a *passepartout* technique in nanomedicine whose data could act as a reference common language while comparing different studies, samples methodologies and approaches in the context of NMs commercial approval.

Chapter 2. AF4 as a tool to unveil the relationship between different nanoforms.

2.1 Introduction

Melanin-like materials, particularly PDA, are gaining prominence in sectors with significant social and economic impacts, such as human health [213-215], energy conversion and storage, and environmental sustainability [216-218]. This success largely stems from the fact that melanin-like nanomaterials exhibit intrinsic biocompatibility, are easy to prepare in biomimetic forms, and possess unique optical and electronic properties as well as unparalleled multifunctionality. Despite recognition and extensive exploration of these exceptional features, these materials are highly complex, displaying a broad range of structures and morphologies that remain poorly understood. This complicates even their classification [217, 219]. Specifically, although PDA has been widely applied in the form of films, water-soluble polymers, and NPs, the relationship between its optical, chemical, physical, and electronic properties and its chemical structure and morphology remains largely unexplored [217]. Most efforts in the scientific community have been directed towards developing synthetic methods that predominantly yield a specific form of PDA (e.g., NPs rather than films). However, the simultaneous presence of different PDA species during the same synthetic process, as well as the distinct mechanisms governing their formation, have generally been overlooked. In this work, we showed that during a typical preparation process, multiple forms of PDA are produced simultaneously from the same molecular precursor, dopamine (DA), and they exhibit significant different properties. We also propose a chemical mechanism that explains how polymerization can result in either poorly branched, low-density polymeric species or highly cross-linked NPs. Additionally, we emphasized the crucial role of self-assembly in NPs formation [220]. To achieve this, we utilized two complementary strategies. The first approach involved monitoring the real-time formation of PDA from DA precursor using a combination of UV/Vis absorption spectroscopy, DLS, and HF5. Through this combination of studies, we demonstrated the simultaneous formation of low-density, poorly branched PDA polymers (PDA-Ps) and dense PDA nanoparticles (PDA-NPs). Both Ps and NPs exhibit the typical feature of melanin-like species: a broad absorption band ranging from UV to near-infrared (NIR). Although they are similar in terms of "coloration," they can be easily distinguished in real time via HF5, since it is

able to distinguish the presence of different morphologies during PDA formation, which allows for investigating formation kinetics of PDA-Ps and PDA-NPs. Our findings revealed that PDA-NPs formation occur within the first six hours of reaction, while PDA-Ps formation continue up to 36 hours. The second approach involved separation of PDANPs and PDAPs at the end of the polymerization process and characterization of their chemical and physical properties individually. These materials were analyzed using UV/Vis absorption spectroscopy, fluorescence spectroscopy with mapping, FT-IR, DLS, and TEM. To identify and quantify the functional groups present, pH titration experiments were conducted on both PDA-Ps and PDA-NPs. The charges of the species formed at various pH levels were determined using z-potential measurements for PDA-NPs and gel electrophoresis for PDA-Ps. Our results demonstrate that PDA-Ps and PDA-NPs exhibit significantly different properties. This is particularly relevant from an application perspective, as the two forms of PDA are expected to perform differently in the same application. For instance, a comparison of the antioxidant activities of PDA-Ps and PDA-NPs using the 2,2-diphenyl-1-picrylhydrazyl (DPPH) scavenging test revealed that PDA-Ps are much more effective antioxidant than PDA-NPs. Similar differences are anticipated in other important applications, such as surface coatings or metal removal. Overall, the HF5 platform, with its rapid and precise capacity for detailed analysis, proves to be an exceptionally effective tool for identifying and selecting the optimal PDA nanoforms for clinical development.

2.2 Materials and methods

Synthesis protocol

In this work we investigated the formation of PDA during a typical oxidation process of DA using atmospheric oxygen in a 1:3 mixture of EtOH/H_2O in the presence of 0.1 M NH_4OH. This reaction was widely exploited to produce PDA-NPs with good mono-dispersity and controlled diameter suitable for nanomedicine [221] or for the fabrication of structural pigments [222]. According to literature, the oxidation and polymerization of the DA precursor are known to result in the formation of NP [223, 224]. However, Messersmith and colleagues also demonstrated the formation of a polymeric structure (MW ~11.2 kDa) under similar conditions [225]. The detailed protocol is reported below.

Synthesis protocol. Initially, 40 mL of ethanol and 90 mL of deionized water were mixed in a 250 mL round-bottom flask. 2 mL of 28-30% NH4OH were added, and the solution was stirred vigorously for 10 minutes. In the next step, a dopamine hydrochloride solution was prepared by dissolving 400 mg of dopamine hydrochloride in 10 mL of deionized water. The dopamine solution was quickly added into the flask under vigorous stirring. An immediate color change was observed, which gradually transitioned from light yellow to dark brown. At the end of reaction, the NPs were collected by centrifugation at 14,000 rpm for 20 minutes. The first supernatant was retained as isolated polymer. The NPs were then washed three times with deionized water at 10,000 rpm and finally redispersed in water.

All reagents, solvents and chemicals were purchased from Sigma-Aldrich.

HF5 instrumental setup

An HF5-UV-FLD-MALS platform was exploited for the study. The system was comprised of an 1100 Series HPLC system (Agilent Technologies, Palo Alto, USA), connected to a module to control AF4 flow rates and operations (Eclipse 3, Wyatt Technology Europe, Dernbach, Germany). The ChemStation version B.04.02 (Agilent Technologies, Santa Clara, USA) data system for Agilent instrumentation was used to set and control the instrumentation and method parameters. The HF5 channels used for the experimental section were standard cartridges containing a 17 cm-long, commercially available hollow fiber. The fiber was a type FUS 0181 PES fiber (Microdyn-Nadir, Wiesbaden, Germany) of 0.8 mm inner diameter, 1.3 mm outer diameter, and 10 kDa Mw cut-off, corresponding to an average pore diameter of 5 nm. Carrier solution (10% EtOH//90% MilliQ water) was degassed using an online vacuum degasser (Agilent, 1100 series, Agilent Technologies). Online detection of the eluted species was performed with the following series of detectors: an Agilent 1100 DAD UV/Vis spectrophotometer, a MALS detector operating at 658 nm wavelength model DAWN HELEOS (Wyatt Technology Corporation, Santa Barbara, USA), a differential refractometer model Optilab rEX (Wyatt Technology Corporation, Santa Barbara, CA, USA), and an Agilent 1200 spectrofluorometer working using a 240 nm excitation wavelength. Data collection was performed by the software ChemStation version B.04.02 and ASTRA® software version 6.1.7 (Wyatt Technology Corporation, Santa Barbara, USA).

HF5 Method development

Other parameters such as crossflow program, detector flow and focusing time were optimized according to what discussed in Section 1.2. The flow program of the developed method is reported below (Table 2.1)

Δt (min)	Mode	Vx start (mL/min)	Vx end (mL/min)	Detector flow (mL/min)	Focus Flow (mL/min)
0.50	Focus	/	/	0.40	0.80
2.00	Focus+Inject	/	/	0.40	0.80
4.00	Elution (Linear)	0.10	0.02	0.40	/
8.00	Elution	0.02	0.02	0.40	/
1.00	Elution	0.00	3.00	0.40	/
1.00	Elution+Inject	0.00	0.00	0.40	/

Table 2.1. Flow program for the separative injection method. Δt (min): time of each step of the analysis. *Vx start (ml/min):* è il cross flow at the beginning of a certain analysis step. *Vx end (ml/min)*: cross flow at the end of a certain analysis step. *Focus flow (ml/min)*: focusing flow.

Particle recovery (expressed as area percentage ratio between a zero-crossflow analysis and separation method) was > 99% indicating no sample loss and no surface interactions with the fiber at the chosen separation conditions.

UV batch analysis

The experiments were carried out in air-equilibrated solutions at 25 °C. UV/Vis absorption spectra were recorded with a Perkin-Elmer Lambda 45 spectrophotometer (PerkinElmer, Inc.; Waltham, USA) using quartz cells with different path lengths that were 1.0 cm, 2 mm and 50 mm.

Hydrodynamic size (DLS) and Z-potential

Hydrodynamic size and Z-potential measurements were performed with Zetasizer Nano ZS (Malvern Panalytical, Malvern, UK) using PMMA semi-microcuvettes (BRAND, Wertheim, Germany).

SEM and TEM

TEM images were obtained using a Philips TEM CM 100 electron microscope (Philips, Amsterdam, Netherlands) at an accelerating voltage of 80kV. Samples were deposited on Formvar on 400 mesh Cu grids (TED PELLA INC, Redding, USA). A ZEISS Leo 1530 (Zeiss group, Oberkochen, Germany) microscope has been used for the SEM measurements.

Electrophoresis

Electrophoresis native agarose gel electrophoresis was performed on an Owl Easycast B-Series Horizontal Gel Systems Model B2 (Thermo Fisher Scientific Inc., Waltham, USA). Electrophoresis was performed in a 1 cm thick 5% agarose gel. The run was performed applying a potential of 30 V.

Fluorescence Spectroscopy

FLD spectra were recorded with a Horiba Jobin Yvon Fluoromax-4 (Horiba Scientific; Kyoto, Japan), a Perkin-Elmer LS-55 (PerkinElmer, Inc.; Waltham, USA) or an Edinburgh FLS920 (Edinburgh Instruments Ltd; Livingstone, UK) equipped with a photomultiplier Hamamatsu R928 (Hamamatsu Photonics; Hamamatsu City, Japan) phototube using quartz cuvettes 1.0cm path length. Excitation-emission fluorescence maps of each sample was determined using a FluoroMax-4 system (Horiba Scientific; Kyoto, Japan), in quartz cuvettes (1 cm).

DPPH Assay for Antioxidant Activity.

DPPH radical scavenging activity was measured according to the literature. Briefly, 0.2 mM of DPPH solution in 95% ethanol was prepared before use, and then either P or NP were dispersed in water and mixed with 1.8 mL of the DPPH solution. The scavenging activity was evaluated by monitoring the absorbance decrease at 516 nm after it remained in the dark for 20 min. DPPH radical scavenging activity was calculated as $\%_{deg}=[1-(Ai-Aj)/Ac]\times100\%$, where Ac is the absorbance of DPPH solution without neither PDA- Ps or PDA- Ps, Ai is the absorbance of the samples of PDA-Ps or PDA-NPs mixed with DPPH solution, and Aj is the absorbance of the samples of P or NP themselves without DPPH solution.

2.3 Results and discussion

HF5 monitoring of the reaction batch content

Melanin-like materials exhibit a broad-band absorption in the red-near infrared (NIR) region, which is responsible for their characteristic dark-brown color, while DA absorbs only in the UV region. Consequently, PDA formation can be easily monitored in a batch mode by tracking the

absorbance of the reaction mixture in the red-NIR range (e.g., 700 nm). As shown in Figure 2.1a, the absorbance at 700 nm increases during the reaction and follows a first-order kinetic behavior, with a rate constant of k = 0.084 h^{-1}. However, this kind of approach alone does not distinguish the different forms of PDA which may form during the reaction.

To achieve this, 5-µL samples of the reaction mixture were injected into the FFF channel at various times and analyzed using UV/Vis absorption and multi-angle light scattering (MALS) detectors. Specifically, the absorbance at 700 nm was monitored as the characteristic PDA signal. The typical elution plot (fractogram) shown in Figure 2.1b, recorded after 4 hours of reaction, presents absorbance as a function of elution time, and it reveals two distinct absorption peaks at elution times t_1 and t_2, clearly indicating the presence of two different PDA species.

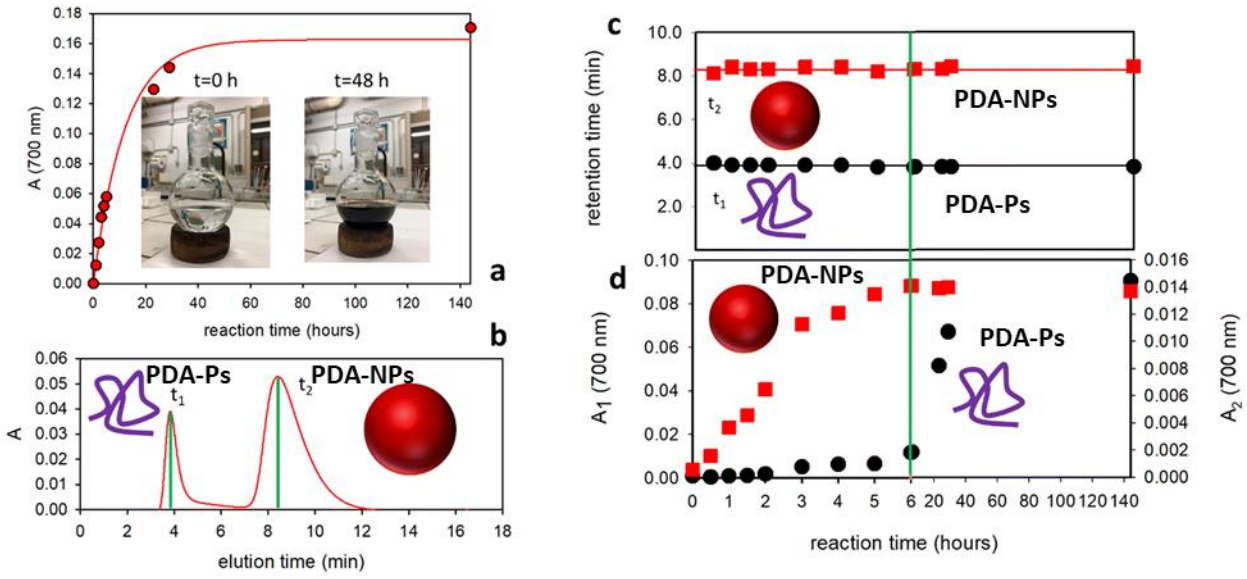

Figure 2.1. (**a**) Absorbance at 700 nm measured for a solution of DA at different times after the preparation (reaction time). The signal could be fitted according to first-order kinetics with k = 0.084 h^{-1}. (**b**) A typical fractogram obtained by HF5 analysis showing the two peaks at retention times t_1 and t_2 for PDA-Ps and the PDA-NPs, respectively. (**c**) Retention times t_1 and t_2 corresponding to the species PDA-Ps (black circles) and PDA-NPs (red squares) measured at different reaction times by FFF. (**d**) Absorbance (peak area) of the species PDA-Ps (black circles A_1) and PDA-Ps (red squares A_2), separated by FFF at different reaction times.

Interestingly, when the PDA formation reaction was followed for 6 days, we observed that: (i) the elution profiles consistently showed two peaks with retention times t_1 and t_2, and (ii) their retention

times remained stable throughout the reaction. This is illustrated in Figure. 2.1c, where the elution times (t_1 = 3.9 min and t_2 = 8.4 min) corresponding to peaks 1 and 2 in the fractogram are plotted against reaction time, showing minimal variation.

It is important to emphasize that since the measured retention time is directly proportional to the hydrodynamic radius (Rh), we can conclude that despite the complexity of the system, (i) only two primary PDA populations are formed during the reaction, and (ii) the hydrodynamic radius (Rh) of these two species remains constant, with values of Rh_1 = 2.7 nm and Rh_2 = 90 nm.

To provide comprehensive information about the optical properties of the two species, 3D spectra at different reaction times are presented in Figure. 2.2. These spectra display absorbance (z-axis) in the 200–800 nm range as a function of the absorption wavelength (x-axis) and retention time (y-axis). Figure 2.2 shows three representative 3D spectra taken at 2 hours, 8 hours, and 6 days of reaction. Both species exhibit the characteristic broad-band absorption spanning from UV to NIR, typical of melanin-like materials. Additionally, Figure 2.1 reveals that while the Rh of the two species remains constant throughout the reaction, there is a significant variation in the concentration ratio of the two species over time.

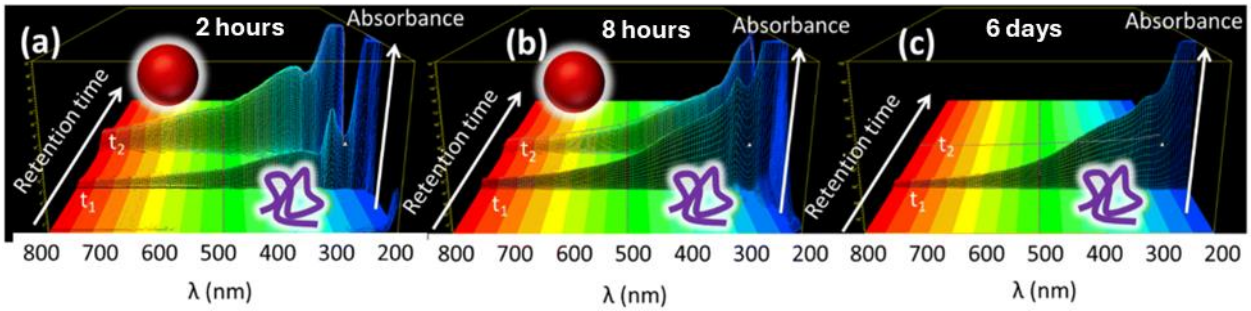

Figure 2.2. A 3-D plot acquired for the elution of a solution of DA at different times after the preparation (reaction time). Plots a, b and c correspond to 2 hours, 8 hours and 6 days reaction times, respectively.

As depicted in Figure 2.1a, after 2 hours of reaction, the species with a longer retention time t_2 and a larger hydrodynamic radius (Rh = 90 nm) dominated the absorbance in the red-NIR region, characteristic of melanin-like materials, while the smaller species with a shorter retention time t_1 and a smaller hydrodynamic radius (Rh = 2.7 nm) exhibited weaker absorption. After 8 hours of reaction (Figure 2.2b), both species contributed almost equally to the NIR absorption, whereas, after 6 days, the smaller species became dominant (Figure. 2.2c). To further understand the

contributions of these two species over time, the absorbance at 700 nm for peaks 1 and 2 (A_1 and A_2, respectively), separated by FFF, was plotted as a function of reaction time (Figure 2.1d). The data reveal that the species with the largest Rh is predominant in the early hours of reaction, with its concentration reaching a plateau after about 6 hours for up to 6 days. In contrast, concentration of the smaller species gradually increased until about 36 hours. These results clearly showed that DA oxidative polymerization under these conditions leads to two distinct melanin-like species with significantly different hydrodynamic radii.

Complementary analysis of the reaction batch

To further characterize these species, DLS was used to monitor the reaction. The scattering intensity, which correlates with both particle size and concentration, began to rise 0.5 hours into the reaction, and DLS analysis confirmed the presence of NP with a radius of approximately 60 nm. The scattering signal continued to increase for up to 6 hours, after which it remained constant, indicating the completion of PDA-NPs formation. Notably, the PDA-NPs size remained unchanged throughout the reaction, with only their concentration varying. The smaller Rh species was undetectable by DLS, as the signal did not change after 6 hours. To further analyze the morphology of the smaller species, FFF was combined with MALS, which, along with light absorption measurements, allowed for the estimation of molecular mass. Unlike the PDA-NPs, the smallest Rh species was identified as low-density polymers (PDA-Ps) with a molecular mass around 100 kDa, consistent with measurements by Messersmith et al [218]. Additionally, a molecular mass of approximately 10^9 Da was determined for the PDA-NPs population. As shown in Fig. 2.1c, the retention time of polymer population (t_1) remained unchanged throughout the 140-hour reaction, indicating no size change.

MALS analysis of the PDA-NPs further confirmed the DLS data. After 24 hours of reaction, MALS revealed a gyration radius (Rg) of 71.5 nm (±2.9%), and conformational analysis yielded a slope of 0.33, indicative of a spherical conformation. It is worth noticing that for a spherical object, Rg is expected to correspond to 0.78 × Rh; according to this relationship the estimated Rh for NP is around 90 nm which is coherent with the one predicted by the theoretical calibration further confirming the spherical shape of the particles. The formation of both PDA-Ps and PDA-NPs was further verified by the SEM images in Figure 2.3.

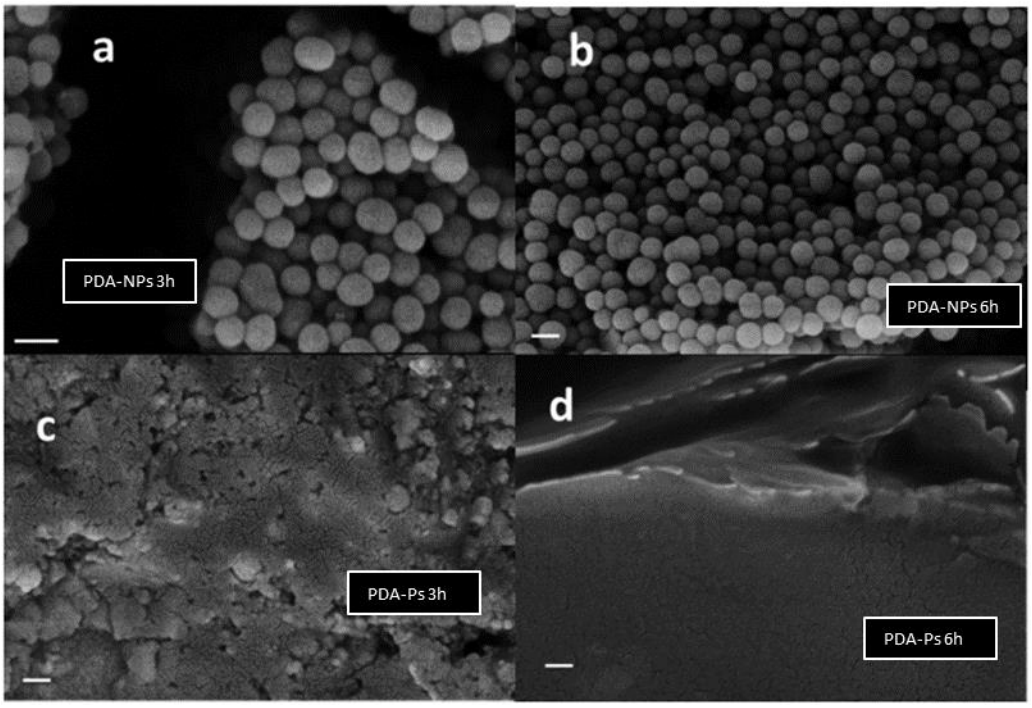

Figure 2.3. SEM images of PDA-NPs obtained after 3 h (**a**) and 6 h (**b**) of reaction. SEM images of PDA-Ps obtained after 3 h (**c**) and 6 h (**d**) reaction. Scale bar is 200 nm in all the cases.

Physicochemical characterization of PDA-NPs and PDA-Ps

As previously discussed, PDA-NPs formation occurred only within the first 6 hours of the reaction, while PDA-Ps production continued for approximately 36 hours. The final composition of the dark-colored suspension, analyzed after 6 days of reaction, involved separating PDA-NPs and PDA-Ps via centrifugation.

Despite their similar dark appearance (Figure 2.4a, inset), PDA-Ps and PDA-NPs exhibited markedly different physical, chemical, optical, and electronic properties. In terms of optical properties, the UV/Vis spectra of the PDA-NPs suspension revealed both absorption and scattering contributions, which together account for attenuation.

The mass attenuation coefficient (μ_m) values for PDA-Ps and PDA-NPs are presented in Figure 2.4a, showing significant differences, especially at higher wavelengths. This discrepancy is largely attributed to the different scattering efficiencies of PDA-Ps and PDA-NPs. Larger nanoparticles (d ~200 nm) are expected to scatter light more efficiently. The differing scattering abilities of PDA-Ps and PDA-NPs can be observed qualitatively in the inset of Figure 2.4b, where a laser

beam (635 nm) passes through two samples containing the same concentration of PDA-Ps and PDA-NPs (5 μg/mL). Only the PDA-NPs scatter light, which is visible at a 90° angle. To quantify this, SiO_2 nanoparticles, known for scattering without absorbing light, were used as a reference. The scattering efficiency as a function of wavelength is shown in Fig. 2.4b, confirming that PDA-Ps scatter light poorly, whereas PDA-NPs exhibit a partially wavelength-dependent scattering efficiency, reaching up to 27% around 600 nm.

In terms of fluorescence, PDA-Ps and PDA-NPs displayed notably different behaviors. As shown in Figure 2.4e, when PDA-Ps and PDA-NPs (both at 10 μg/mL) were excited at 460 nm, only scattered light matching the excitation color was detected for PDA-NPs, whereas PDA-Ps emitted a greenish fluorescence. These observations were confirmed via steady-state fluorescence spectroscopy. In the case of PDA-NPs, the fluorescence spectrum was dominated by scattering, while PDA-Ps showed excitation-dependent fluorescence. To further characterize PDA-Ps fluorescence, a fluorescence map of PDA-Ps (10 μg/mL) was obtained, as seen in Figure 2.4c. The pattern observed in Figure 2.4c is typical of systems with excitation-wavelength-dependent emission, as corroborated by the fluorescence spectra recorded at different excitation wavelengths in Figure 2.4d.

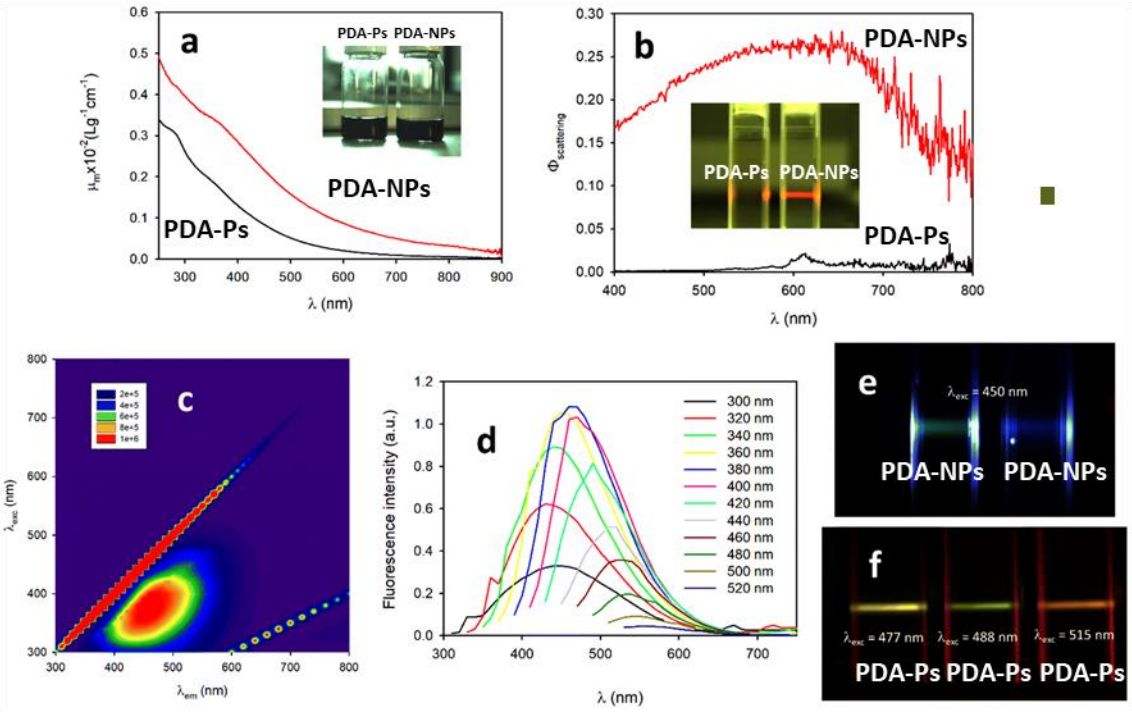

Figure 2.4. (**a**) Mass attenuation coefficients of PDA-Ps and PDA-NPs; inset: digital picture of PDA-Ps and PDA-NPs. (**b**) Scattering efficiency spectrum of PDA-Ps and PDA-NPs; inset: digital picture of PDA-Ps and PDA-NPs irradiated with a 635 nm laser. (**c**) Emission map of PDA-Ps. (**d**) Fluorescence spectra of PDA-Ps at different excitation wavelengths. (**e**) Digital picture of PDA-Ps and PDA-NP excited with a blue (460 nm) light beam. (**f**) Digital picture of PDA-Ps excited with different wavelength laser beams.

Different emission colors at varying excitation wavelengths for the same PDA-Ps sample were also captured using a digital camera, with excitation achieved through different wavelengths of an argon laser, as shown in Figure 2.4f. This behavior is characteristic of systems containing multiple independent fluorophoric units, which can be individually excited and detected. To further investigate the formation process of PDA-Ps and PDA-NPs, the oxidation of DA was studied at different initial concentrations of the precursor, and the amounts of PDA-Ps and PDA-NPs produced after 36 hours were compared. The results, presented in Figure 2.5, clearly demonstrate that PDA-NPs form only at high DA concentrations, whereas PDA-Ps can also form at lower DA concentrations.

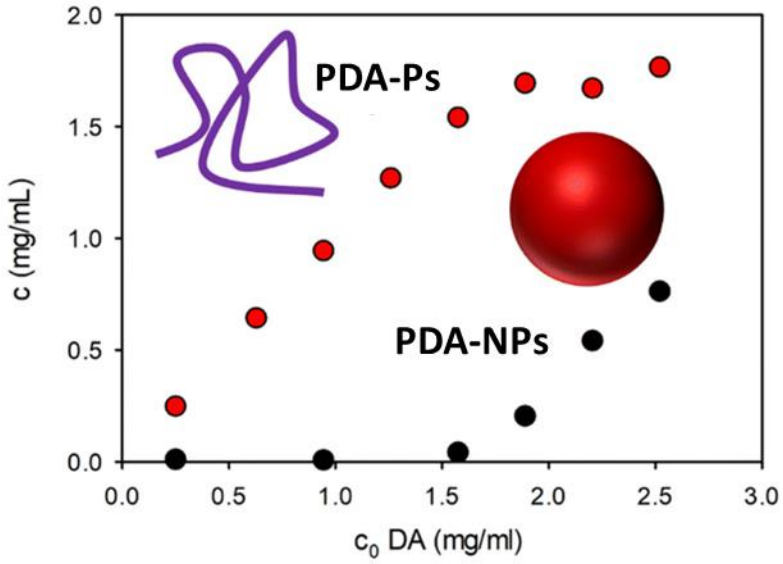

Figure 2.5. Concentration of PDA-NPs (black dots) and PDA-Ps (red dots) obtained after 36 hours of oxidation of DA at different initial concentrations of DA.

The distinct morphologies of PDA-Ps and PDA-NPs were clearly confirmed by TEM analysis. As shown in Figure 2.6a and b, spherical particles with a diameter of approximately 160 nm were observed in the case of PDA-NPs, whereas PDA-Ps only formed a solid black material upon drying on the TEM grid. The FTIR spectra of the two samples, shown in Figure 2.7c, were also completely different. Similar morphological differences were observed in the SEM images presented in Figure 2.3.

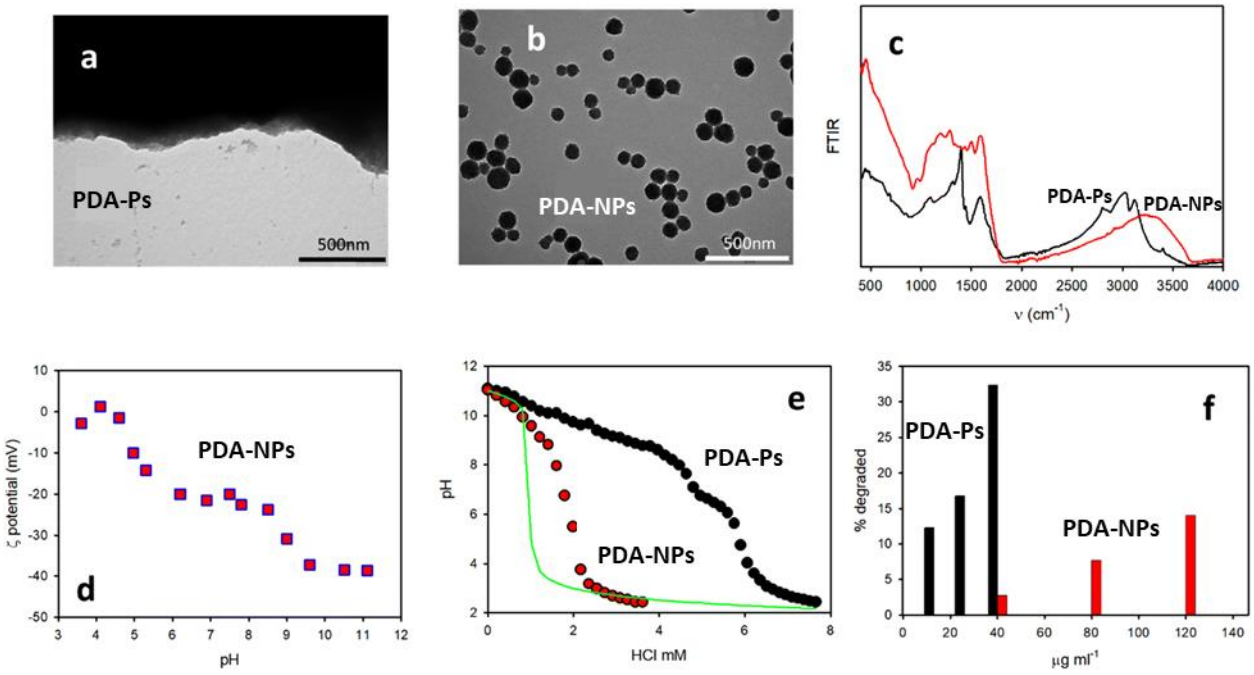

Figure 2.6. TEM images of PDA-Ps (**a**) and PDA-NPs (**b**). (**c**) FTIR spectra of PDA-Ps and PDA-NPs (**d**) Z-potential of PDA-NPs as a function of pH. (**e**) pH titration of P and NP. (**f**) DPPH degraded by P and NP at different concentrations.

To identify and quantify the acidic groups in PDA-Ps and PDA-NPs, pH titration experiments were performed. Equal concentrations (1 mg/mL) of both species were used, with NaOH added to raise the initial pH to 11. Subsequently, a 1 M HCl solution was added incrementally, and the pH was measured. Fig. 2.7e shows the pH variations for PDA-Ps and PDA-NPs (1 mg/mL) compared to NaOH at pH 11. The results revealed that the pure NaOH solution experienced a sharp drop in pH upon the addition of 1 mM HCl. In the case of PDA-NPs, however, the pH drop was delayed by 1 mM, indicating the presence of protonable groups (2 mmol/g). In contrast, PDA-Ps showed a much larger shift in pH, with two distinct protonation processes: one at pH ≈ 9.0 (∼4 mM HCl) and another at pH ≈ 6.0 (∼1 mM HCl).

To further explore the protonable groups, z-potential measurements were performed for PDA-NPs, as shown in Figure 2.6d. The results indicate a negative z-potential for PDA-NPs across all pH values, with a surface charge near 0 mV at pH levels below 4. PDA-NPs exhibited a strongly negative z-potential of approximately −40 mV at pH 11, which became less negative (∼−20 mV)

at neutral pH 7, with protonation occurring around pH 9. Another protonation was observed near pH 5, leading to a non-charged species. At pH 3, NP lost colloidal stability and precipitated, suggesting that protonation at pH ∼9 is due to residual $–O^-$ catechol groups, while protonation at pH ∼5 is likely due to carboxylate groups ($–COO^-$) formed by DA oxidation.

For PDA-Ps, light scattering could not be used to determine charge at different pH levels, so agarose gel electrophoresis was employed. The results showed that PDA-Ps carried a negative charge at pH >3, migrating towards the positive electrode, but did not migrate at pH <3: this is consistent with the observed precipitation of PDA-Ps at acidic pH. The titration data in Figure 2.6e revealed protonation of P at pH levels of approximately 9 and 6, like PDA-NPs, but with a much higher concentration of –OH (8 mmol/g) and –COOH (2 mmol/g) groups. In contrast, PDA-NPs had a total –OH and –COOH concentration of around 2 mmol/g, with equal fractions of ∼1 mmol/g for each group.

These findings highlight that DA undergoes more extensive oxidation in PDA-NPs, resulting in a much lower concentration of residual –OH groups compared to PDA-Ps. This conclusion was supported by antioxidant activity experiments, particularly the DPPH quenching assay. As shown in Figure 2.6f, at a concentration of 40 μg/mL, PDA-Ps degraded about 33% of the DPPH radical, while PDA-NPs degraded only 3%. This difference in antioxidant activity is noteworthy, as it has been linked to the presence of residual –OH catechol groups [226, 227]. Thus, the lower antioxidant activity of PDA-NPs is attributed to the reduced concentration of these groups, as confirmed by the above measurements.

2.4 Conclusions

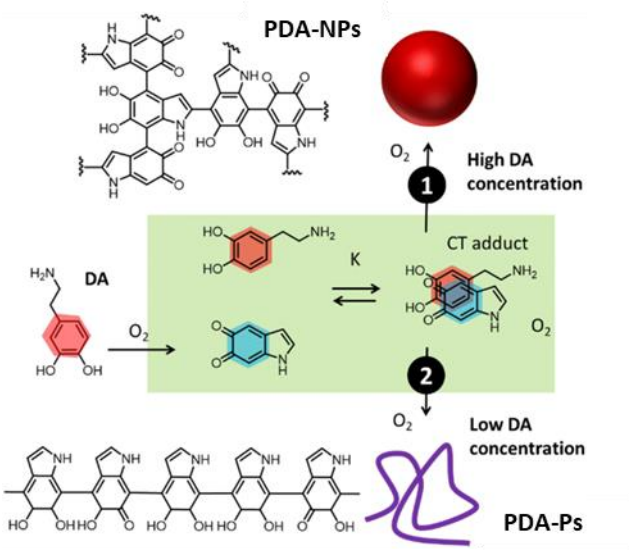

Figure 2.7. Schematization of the oxidation and polymerization of DA occurred through two different pathways leading to the simultaneous formation of PDA-NPs and PDA-Ps.

We demonstrated that during the oxidative polymerization of DA in the presence of atmospheric oxygen, both dense NPs and low-density polymer are simultaneously formed. Specifically, PDA-NPs formation occurs only within the first 6 hours of reaction, while PDA-NPs continues to polymerize up to 36 hours after the reaction begins. This phenomenon is coherent with a recent literature finding which showed that a supramolecular adduct between DA and oxidized DA can be detected in the early stages of DA oxidation [220]. This process facilitates the reaction of orthoquinone, produced by DA self oxidation, leading to polymerization. Concentration-dependent experiments revealed that PDA-NPs form only at high DA concentrations and stops when the concentration drops below a critical threshold (reached after 6 hours at an initial DA concentration of 2.6 mM). These findings suggest that large aggregates of DA and oxidized DA form at high DA concentrations, leading to NPs formation. While PDA-Ps form even at low DA concentrations and primarily results from the linear polymerization of DHI units produced by DA cyclization, PDA-NPs only form at high DA precursor concentrations. PDA-Ps and PDA-NPs exhibit distinct compositions, and distinct optical and chemical properties. PDA-NPs could be observed by TEM and SEM as spheres around 160 nm in size, consistent with FFF, DLS, and SLS measurements, while PDA-Ps appears as large aggregates in TEM and SEM images. Z-potential

measurements, gel electrophoresis, and pH titration revealed that PDA-Ps contain about 8 mmol/g catecholic –OH groups and 2 mmol/g –COOH groups, whereas PDA-NPs contains fewer catecholic –OH (1 mmol/g) and –COOH (1 mmol/g) groups. The lower density of catechol units makes PDA-NPs significantly less effective as an antioxidant compared to PDA-Ps. In terms of optical properties, both PDA-Ps and PDA-NPs exhibit the characteristic broad absorption band of melanin-like compounds; however, PDA-NPs demonstrates more effective light attenuation, especially in the vis-NIR region. Regarding excited state deactivation, PDA-Ps shows excitation wavelength-dependent fluorescence, characteristic of multi-fluorophoric decoupled systems, while PDA-NPs lacks fluorescence, but it scatters light with an efficiency of 27%. The distinct chemical compositions of PDA-Ps and PDA-NPs are further evidenced by their markedly different FTIR spectra. These findings should be considered in the design and development of new melanin-based nanoplatforms for applications in nanomedicine, energy conversion, and environmental remediation. Additionally, the term "PDA" itself should be re-evaluated, as it encompasses species with widely varying chemical, physical, optical, and electronic properties.

In this work HF5-MD played a key role, especially in the first stages of the research, and it allowed to:

1. Identify the contemporaneous presence of PDA-Ps and PDA-NPs in the reaction batch.
2. Monitor their differential formation over time while providing simultaneous multiparametric characterization of the species.

These features and result were consistent with what obtained by complementary techniques (SEM and DLS) and they represented the founding knowledge which led to expand the study with different, multiple techniques applied offline, as well as to help in their interpretation when results apparently incoherent were observed (e.g. size calculated by DLS and SEM). Additionally, the HF-MD approach is fast (separation in less than 20min) and automatable. Overall, these findings make HF5-MD emerge as an extremely powerful tool for the design and characterization of most optimal PDA nanoforms for clinical application.

Chapter 3. AF4 as an *all-in-one* platform for synthesis monitoring, characterization and purification of antimicrobial NPs

3.1 Introduction

As first described in section 1.1.1, metal NPs are increasingly used as an alternative to antibiotics or in combination with them. The advantages of these strategies are numerous, including providing activity based on different and simultaneous mechanisms such as oxidative stress induction, metal ion release, and non-oxidative mechanisms; the prevention of microbial drug resistance; and their potential use as carriers of antibiotics [228]. A wide range of nanomaterials have been demonstrated to possess antimicrobial effects, including iron (III) oxide, zinc oxide, magnesium oxide, silver, gold, copper and copper oxide, calcium oxide, titanium dioxide, and cadmium oxide. Among these, silver NPs (AgNPs) show promise for use as antimicrobials able to kill both Gram-negative and Gram-positive bacteria [229] due to both their internalization in the cell due to their small size and their release of silver ions [230]. Some antibacterial properties are strictly related to particle size, with smaller particles showing improved activity due to their increased surface area to mass ratio and higher surface reaction activities [231-233]. Different mechanisms of ion-dependent antimicrobial action, such as interference with bacterial metabolic processes and structures, cell wall disruption, and increased cell permeability, have been reported for AgNPs, including interaction with DNA [234] or the generation of reactive oxygen species [235, 236]. Cooperative actions with antibiotics and antifungal agents are also able to reduce the need for high antibiotic dosages and therefore minimize side effects [237, 238].

In this framework, biocompatible coatings can be used to improve antibacterial effects without increasing cytotoxicity, making the interactions with the biological system more versatile. A recent study demonstrated that PDA coating significantly enhances the potency of PDA-AgNPs against *Escherichia coli* [239]. In particular, the interaction between Ag and the catechol group on the PDA coating is responsible for the increase in the generation of ROS, causing bacterial damage.

Ag-coated PDA microspheres have been used to kill *Staphylococcus aureus* cells due to their elevated ROS level [240].

Even though Ag-PDA particles exhibit excellent antimicrobial activity, problems such as aggregation and toxicity limit their practical application.

To solve these issues, many researchers have focused on NP preparation. In one study, PDA nanospheres loaded with silver NPs with a controlled size able to inhibit bacterial growth were prepared exploiting the reduction of silver nitrate by PDA spheres [241]. Both in situ and ex situ methods have been developed for incorporating AgNPs onto material surfaces [242]. The reducing catechol groups of PDA have further been explored with regard to their ability to form in situ well-dispersed AgNPs on different membranes with improved salt rejection and a maintenance of good permeability, simultaneously enhancing the anti-adhesive and antimicrobial properties of the membrane [243]. Polysulfone membranes were also similarly modified to mitigate biofouling [244]. PDA was used to form a thin layer and induce AgNP formation without the use of additional reductants or stabilizers on central venous catheters or poly(ether ketone) implants, achieving both significant antimicrobial efficacy and limited biological side effects [245, 246].

As mentioned in Chapter 2, although the methods of preparation and application of PDA NPs are rapidly increasing, the structures and polymerization mechanisms used to obtain, purify, and define the size of NPs still represent an open issue, with limitations in their use [247]. While the development of PDA-based films is at a more advanced stage, there are no techniques or methods of synthesis in suspension able to yield NPs with a controlled size, high efficiency, and high purity therefore requiring purification. This type of step is often vaguely defined and achieved mainly by centrifugation, not considering the coexistence of different species.

The development of a method for the deep, native characterization of these NPs either during their synthesis or as a final product represents another crucial point that must be addressed before these nanoproducts can be used as antimicrobial tools in medical applications. Synthesized particles are usually characterized by FT-IR spectra for the identification of functional groups; while SEM and TEM are among the most widely used techniques for the direct determination of the geometric size, shape, and ultrastructural properties of those NPs [248]. However, the observed values may differ significantly from the native size/morphology that NPs exhibit in liquid dispersion. Light scattering (LS) methods are also broadly used to analyze the size of AgNPs, and DLS is perhaps

the most widely used technique for hydrodynamic size distribution analysis [249, 250]. However, DLS does not provide information on particle shape or density distribution, and in the case of samples with complex, multimodal PSD, the accuracy of DLS-based PSD analysis may be inherently limited. Static, multi-angle LS (MALS) provides independent data on NP molar mass (M) and RMS radius values [251], which can provide insights into the conformation and structure of NPs. Similar to DLS, the detection accuracy MALS is reduced for NPs with complex and multimodal PSD. These techniques are inadequate for directly providing precise information on dispersed NPs, particularly when multiple species coexist, and samples exhibit considerable complexity and heterogeneity.

Coherently with EMA and FDA guidelines [28] the combination of DLS or MALS with size-based separation methods can enhance the accuracy of size analysis for complex NP samples. Within this context recently, AF4 was applied to the quantification of AgNPs in complex matrices like food and biological samples [252-254]. HF5 has already been employed for the deep characterization of silver NPs, providing critical data on size/morphological characterization and ion release quantification under various conditions (e.g., dilution, preservation media, coated surfaces) [198, 255].

In this study the application of an HF5-based analytical platform for characterizing Ag-PDA NPs in dispersion, both during synthesis to monitor particle formation and to characterize, separate, and collect purified particles is described. The aim was to offer a time-efficient, cost-effective solution that overcomes the limitations of offline techniques, integrating information on particle synthesis and formation, delivering product characterization, and enabling the prompt purification of isolated, biologically active NPs. Notably, the purified AgPDA NPs were shown to effectively inhibit bacterial growth in vitro against *S. aureus* and *E. coli* reference strains, in contrast to the lack of activity in unpurified samples. Overall, the developed method can be used for synthesis optimization and the QC of the final AgPDA NPs product.

3.2 Materials and methods

Synthesis of Ag-PDA NPs

The synthesis of Ag-PDA NPs was performed with an optimized method elaborated from the literature [255-257]. An initial screening of synthesis conditions was performed to define the best reaction mixture (Table 3.1 and Fig 3.1), which was then used for this study.

	Ag ($AgNO_3$) (mM)	Dopamine-HCl (mM)	EtOH (% v/v)	Ammonia (% v/v)
R1	2	10	30	1
R2	1	10	30	1
R3	0.5	10	30	1
R4	0.5	2.5	30	1
R5	1	2.5	30	1

Table 3.1. Concentration of reagents (reaction batch) and medium used in Ag-PDA synthesis.

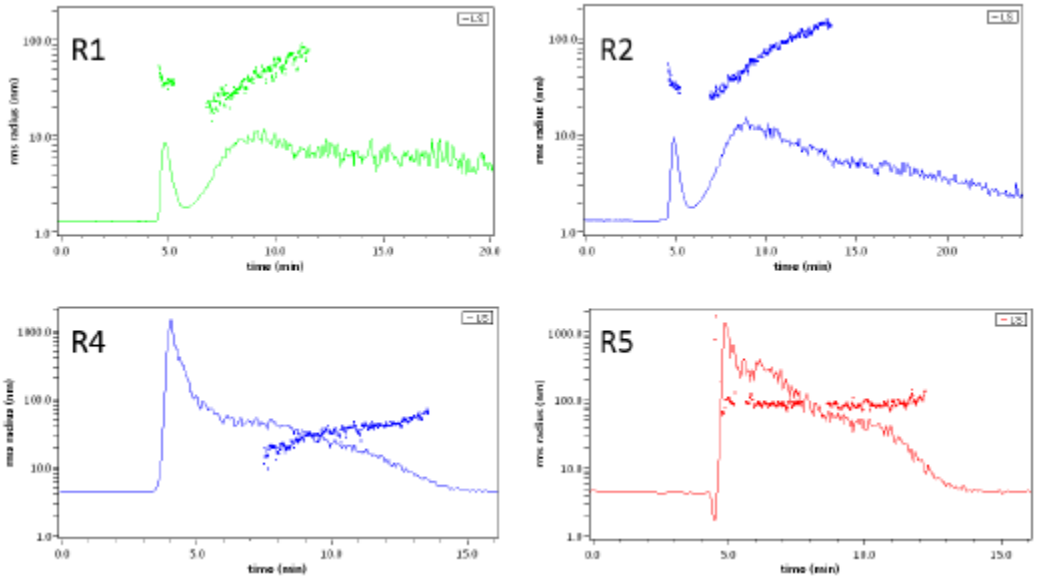

Figure 3.1. Solid line: LS profile of Ag-PDA particles obtained with R1-R2-R4-R5 Ag/dopamine ratios. Dotted distribution: Gyration radii.

Each reaction (R1-R5) was carried out for 30 hours. A 50 µL aliquot was injected and analyzed with HF5-MD to verify the formation of Ag-PDA NPs. The results showed that an increase in Ag concentration yielded less monodispersed particles, ranging from 25 to >100 nm in terms of Gyration radius (Fig 3.1, R1-R2). A lower dopamine concentration led to a scarce resolution from

the first population, suggesting that the formation of PDA particles was less effective. (Fig 3.1, R4-R5). R3 (Section 3.3) was then chosen for time monitoring, online and offline characterization, and activity tests.

Synthesis procedure. Briefly, ammonia aqueous solution (25%) was added to a mixture of ethanol in water (30% v/v). Following this, $AgNO_3$ was added to achieve a final concentration of 0.5 mM. Finally, Dopamine-HCl was added drop by drop and the solution was kept under stirring. The stirring solution turned first yellow, indicating the beginning of AgNP formation [258], and then became black, indicating the beginning of the formation of PDA (melanin) composites. The sampling of the solution was performed during the color changes (15 min, 1 h, 2 h) and every two hours from 22 h to 30 h. All reagents were purchased from Sigma Aldrich (St. Louis, USA). MilliQ water was employed for the mobile phase and synthesis medium.

HF5 instrumental setup

HF5 analyses were performed using an Agilent 1200 HPLC system (Agilent Technologies, Santa Clara, USA) consisting of a degasser, an isocratic pump, and an Agilent 1100 DAD UV/Vis spectrophotometer combined with an Eclipse® DUALTEC separation system (Wyatt Technology Europe, Dernbach, Germany). The system was connected to an 18-angle multiangle light scattering detector model DAWN HELEOS (Wyatt Technology Corporation, Santa Barbara, USA). The HF5 cartridge (Wyatt Technology Europe) is commercially available and has a 10 kDa cutoff. ChemStation version B.04.02 (Agilent Technologies) data system for Agilent instrumentation was used to set and control the instrumentation and for the computation of various separation parameters, complete with the Wyatt Eclipse @ ChemStation version 3.5.02 (Wyatt Technology Europe). ASTRA® software version 6.1.7 (Wyatt Technology Corporation) was used to handle signals from the detectors (MALS and UV) and to compute the sample Rg values.

The flow conditions for the developed HF5 method are detailed in Table 3.2, where longitudinal flow is indicated by Vc, and cross/focus flow is marked as Vx.

Δt (min)	Mode	Vx start (mL/min)	Vx end (mL/min)	Vc (mL/min)	Focus Flow (mL/min)
2.00	Focus	/	/	0.35	0.80
3.00	Focus+Inject	/	/	0.35	0.80
20.00	Elution	0.10	0.10	0.35	/
6.00	Elution+Inject	0.00	0.00	0.35	/

Table 3.2. Flow conditions used for the HF5 analyses of PDA and Ag-PDA.

MALS was used to calculate the gyration radius of eluted species, providing an absolute determination of the particle root mean square radius of gyration (Rg) by measuring the net intensity of light scattered by particles at fixed angles. The polydispersity index of the two populations obtained from FFF analysis was derived from the LS data. This separation method characterized the synthesis and fractionated Ag-PDA NPs. The injection volume was set to 10 µL for synthesis monitoring and 50 µL for particle characterization and collection. All analyses were conducted in MilliQ water as the mobile phase.

For antimicrobial evaluation, both non-separative, non-filtrating (FIA) and non-separative, filtrating (FFIA) methods were employed.

SEM Analysis

For morphological examinations, a few drops of each sample of interest were deposited onto a metallic stub and allowed to dry. A Philips XL-20 scanning electron microscope (Philips, Amsterdam, Netherlands) operating at 15 kV was used. Samples were sputter-coated with gold before examination. EDX measurements were also performed to confirm the presence of silver.

X-ray Powder Diffraction Analysis

For X-ray investigations, a few drops of each sample of interest (FFF fractions 1 and 2) were deposited onto a recessed silicon glass and allowed to dry. X-ray powder diffraction analyses were carried out using a Philips X'Celerator powder diffractometer (Philips, Amsterdam, Netherlands) equipped with a graphite monochromator in the diffracted beam. CuKα radiation (λ = 1.54 Å; 40 mA, 40 kV) was used. The 2θ range was from 30° to 80°, with a step size of 0.0668° and a scan rate of 500 s/step.

Antibacterial Activity

The antibacterial activity of the fractions derived from FIA, FFIA, and the method was evaluated in vitro against Staphylococcus aureus (ATCC 25923) and Escherichia coli (ATCC 25922), representing Gram-positive and Gram-negative bacteria, respectively. The effectiveness of the samples in inhibiting bacterial growth was assessed using a standardized microdilution broth method with a 96-well plate [259]. Bacterial suspensions were prepared at 0.5 McFarland, diluted 1:200 in Mueller–Hinton Broth (Sigma-Aldrich), and incubated with sample dilutions, starting with a ten-fold dilution of the volume collected from the fractionation process. Controls measured bacterial growth in regular medium (positive control) and checked the background turbidity of reagents and sterility of the procedures (negative controls). The microplate was incubated at 37°C, and bacterial growth was monitored by measuring Optical Density at 630 nm (Multiskan Ascent microplate reader, Thermo Fisher Scientific Inc., Waltham, USA). Percentage values of samples under different experimental conditions were determined relative to the positive growth control.

3.3 Results and discussion

Monitoring the Synthesis of Ag-PDA

Following the addition of dopamine to $AgNO_3$, according to the optimized synthesis protocol (see Section 3.2), we monitored the solution during the initial phase (at 15 min, 1 h, and 2 h) by collecting 10 µL of reaction medium at each timepoint and analyzing it via HF5 MD. The absorption profiles and the appearance of solution are depicted in Figure 3.2. The color change from transparent (Figure 3.2a) to yellow (Figure 3.2b) to black (Figure 3.2c) indicated both the initial formation of Ag seeds and the polymerization of dopamine. Concurrently, absorption signals at 310 nm showed an emerging band that increased in intensity at a low retention time (5 min) and developed into a second band at 7 min. However, these species were small and barely retained by the system, as they eluted at the void time (5 min). The high absorption and flat signal of laser scattering detection (not shown) indicated the lack of a nanodispersed sample.

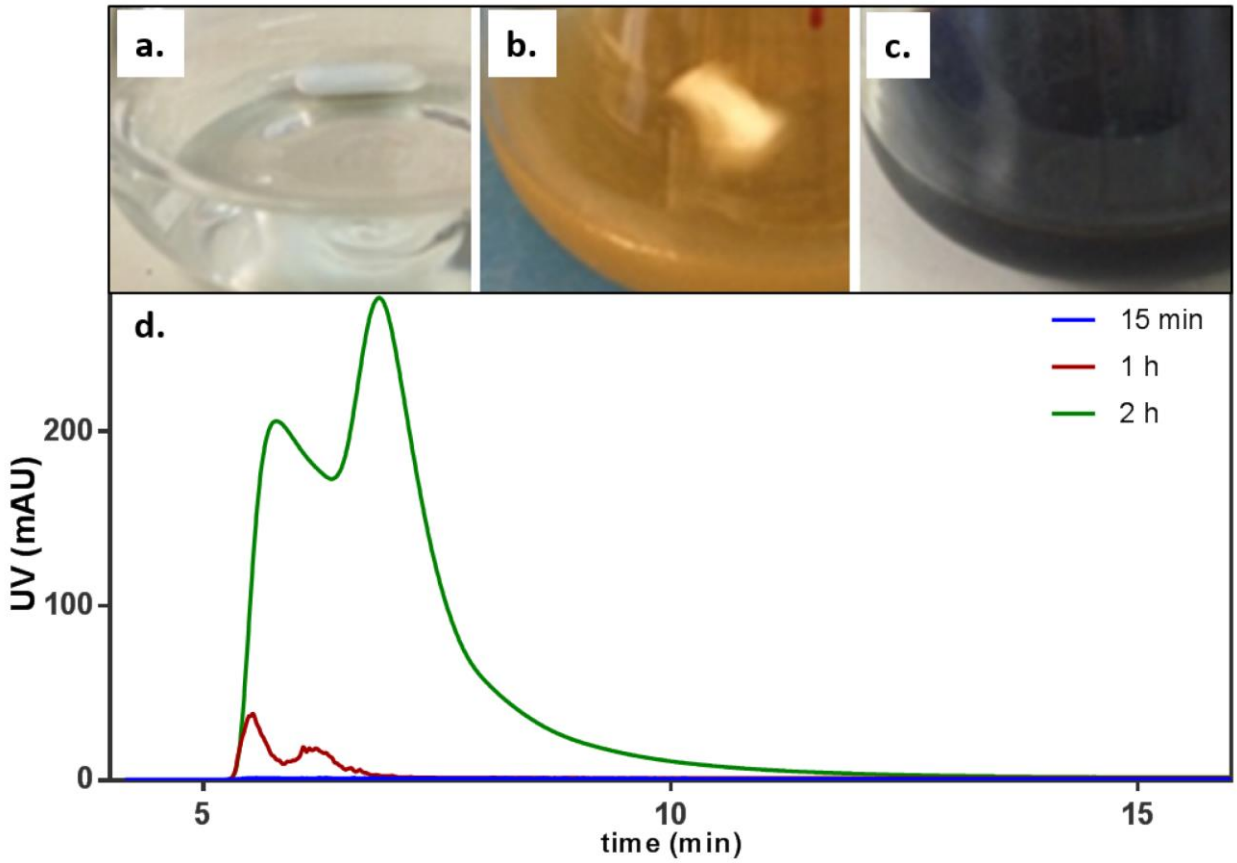

Figure 3.2. Appearance of the mixed solution over time after (**a**) 15 min, (**b**) 1 h, and (**c**) 2 h. (**d**) Absorption signal corresponding to the first stages of Ag-PDA formation, monitored by sampling and injection into HF5-MD after 15 min (blue), 1 h (red), and 2 h (green).

Subsequent reaction monitoring showed the appearance of an intense peak detected by MALS after approximately 20 hours, consistent with literature reports [257, 258, 260]. Real-time analysis, performed every two hours, illustrated the formation of Ag-PDA NPs (Figure 3.3).

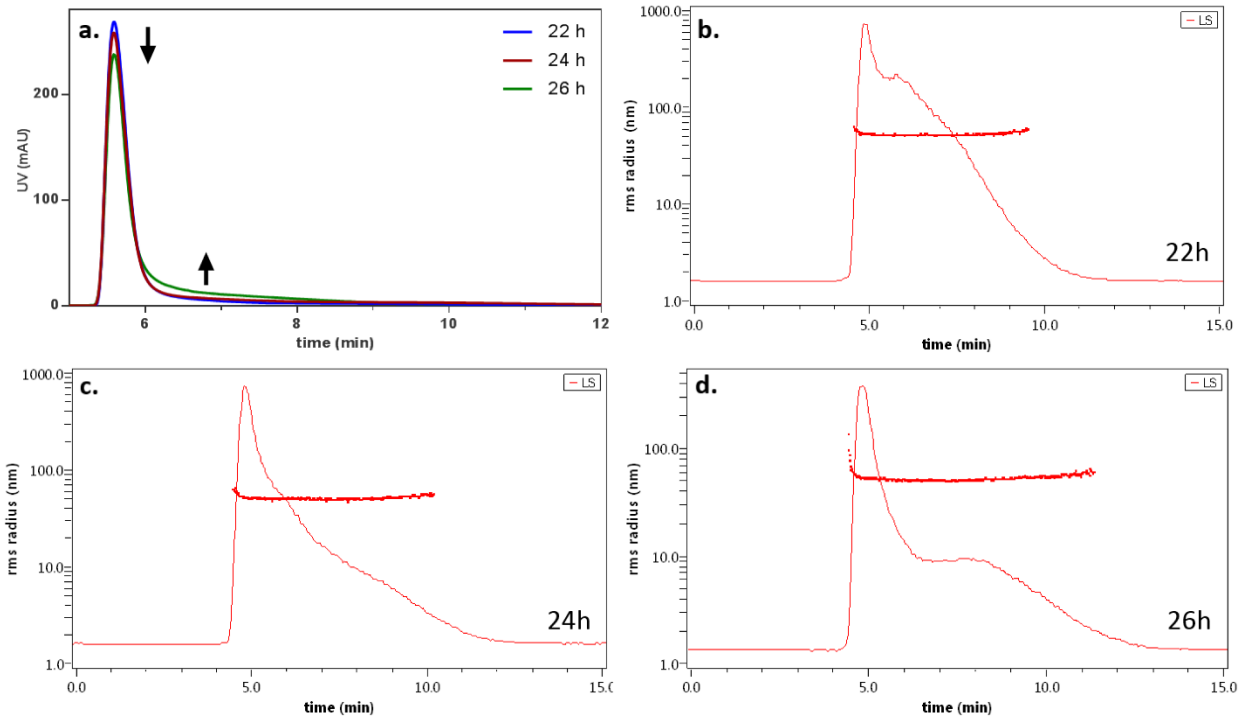

Figure 3.3. (**a**). Overlay of the UV absorption signal at 310 nm at three timepoints (22, 24, and 26 h). (**b–d**) LS signal (at 90°) and calculated radius of the species detected at the three timepoints.

Figure 3.3a shows the UV absorption profiles at 22, 24, and 26 hours, where an intense band at 5 min gradually diminished with increasing reaction time, accompanied by a peak tail with increasing absorption (black arrows). While UV detection alone may not reveal this, the light scattering trace (Figure 3.3b–d) clearly showed the emergence of a second species, with the measured gyration radii indicating good monodispersity. The radii ranged from 38 ± 5 nm (at 22 h) to 45 ± 4 nm (at 26 h), consistent with particle growth. Such detailed data on Ag-PDA synthesis would be challenging to obtain using offline techniques alone, which are cost- and time-intensive. Moreover, faster methods like DLS and spectra acquisition could not distinguish different species during early particle formation stages.

Online Characterization of Ag-PDA

The reaction was monitored until the relative intensities of the two bands stabilized. After 30 hours, the second band was resolved from the first (Figure 3.4a), indicating that two distinct species, likely in equilibrium, had formed.

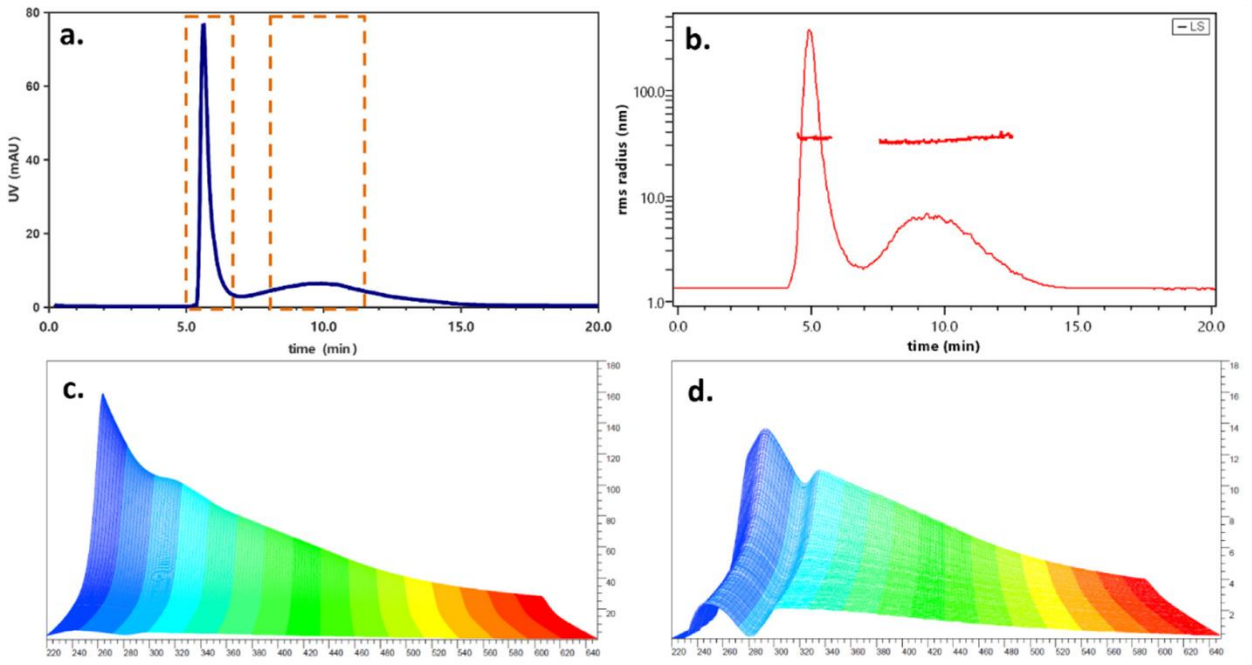

Figure 3.4. (**a**) UV fractogram at 310 nm; dashed selections: collection ranges. (**b**) Corresponding laser scattering profile. (**c**) UV spectrum of first band. (**d**) UV spectrum of second band.

The scattering profile (Figure 3.4b) is relatively more intense for the second band, which is compatible both with the increased hydrodynamical size and the presence of a stronger scatterer such as silver. The radius calculation supported this distinction: the first species, eluted at the void time, had a high gyration radius (35 ± 6 nm), suggesting intertwined polymeric chains lacking organized 3D structure chains which could be eluted with an inverse mechanism due to their elongated morphology [261]. A PDI value of 1.109 further supported the lack of structural organization of population 1 (a PDI value of 1.000 corresponds to a monodispersed sample). The second species, with a gyration radius of 47 ± 5 nm, was more monodispersed (PDI = 1.016). To verify the hydrodynamical size of Ag-PDA NPs, a size standard (polystyrene beads, geometrical radius = 51 nm) was injected (not shown). The resulting retention time was found to be identical to that of band 2, indicating that the estimated Rh of this species the same.

The morphology and arrangement of the PDA-silver nanocomposite were further explored by studying its shape factor. The shape factor, calculated as the Rg/Rh ratio, indicates the mass distribution relative to the center of mass of the particle. A value of 0.8 corresponds to solid spheres

(e.g., polystyrene beads), values closer to 1 indicate core-shell systems or prolate ellipsoids while higher values are associated to more elongated structures such as rods (1.4) and random coils (1.6).

The first species exhibits a shape factor >>1 consistent with its attribution to elongated PDA structures. The value of 0.9 for Species 2 particles suggests that nanosilver was localized on the nanoparticle surface, creating a denser shell and a slightly elongated structure compared to a perfect solid sphere [262]. The size, shape, and polydispersity results for the two species are summarized in Table 3.3.

	Hydrodynamic Radius (nm)	Gyration Radius (mm)	PDI	Shape Factor
Species 1	-	35 ± 6	1.109	>>1
Species 2	51	47 ± 5	1.016	0.9

Table 3.3. Summary of the size and morphology of the two populations separated and characterized through HF5-MD.

The spectroscopic behavior of the two species was also different (Figure 3c,d). The first species exhibited a spectrum typical of PDA, while the second displayed a local maximum at 390 nm, indicating that nanosilver was embedded in the PDA particle. This information is critical for potential applications: for instance, the presence of a biocompatible polymer which could be deposited as a film could hinder the application of a silver delivery system. While, by distinguishing and separating the two species it is possible to enable the production of an effective antiseptic candidate while minimizing this risk [263]. Two fractions (collected between 4–6 min and 8.5–11.5 min) were subjected to further offline characterization.

Purification and Offline Characterization

The two fractions were imaged using SEM. The first species (Figure 3.5a) appeared amorphous, lacking 3D organization, while the second (Figure 3.5b) consisted of well-defined, spherical particles (~100 nm in diameter). Energy dispersive X-ray (EDX) analysis confirmed the presence of silver only in the second fraction (green points), in line with the absorption maximum observed in Figure 3.4d. While the presence of silver in the nanostructure was confirmed, it was necessary to determine the nature of silver in the second fraction. This was achieved by X-ray analysis, together with the analysis of the spectrum of $AgNO_3$ as a reference. X-ray diffraction analysis confirmed that the second fraction contained metallic nanosilver, as evidenced by characteristic

Ag crystal peaks, while no Ag^+ signal was observed. Overall, these results were consistent with the peak attribution based on LS and spectroscopic results provided by the HF5-MD platform.

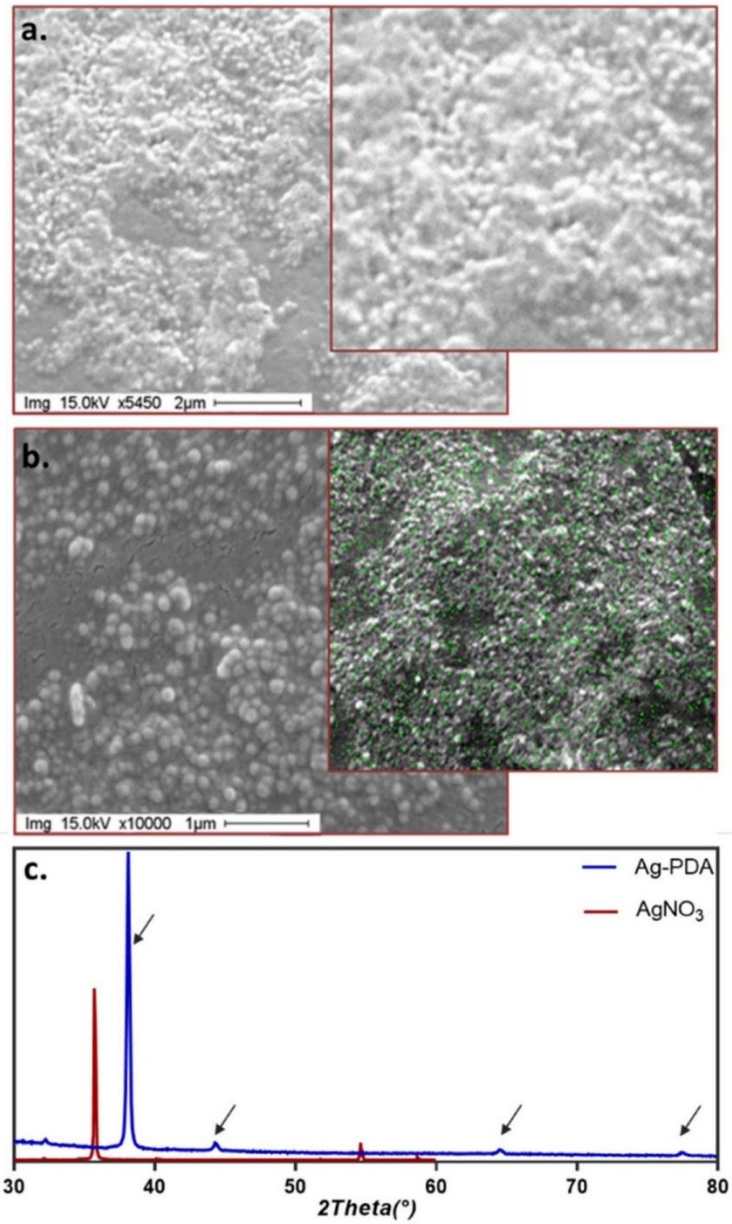

Figure 3.5. (**a**) SEM image of the first fraction (**b**) SEM image of the second fraction. Inset: EDX map. (**c**): X-rays diffraction patterns of the second fraction (blue line) collected (arrows: typical reflections of nanoAg), superimposed on the AgNO3 pattern as a control (red line). Indeed, analysis of the X-ray diffraction pattern shows characteristic peaks of Ag crystal found at 38.092, 44.214, 64.409, and 77.344 on the 2θ scale, corresponding, respectively, to the (1 1 1), (2 0 0), (2 2 0), and (3 1 1) crystal planes. There was no signal corresponding to Ag^+.

Antibacterial Activity

To evaluate the antimicrobial activity of the Ag-PDA NPs, we produced four sample fractions representing various stages of the reaction: free dopamine and potential unreacted Ag^+ ions (Figure 3.6A), colloidal polymeric PDA and Ag-PDA (Figure 3.6B), purified PDA (Figure 3.6C), and purified Ag-PDA (Figure 3.6D). This was achieved by the collection of HF5 fractions via FIA, FFIA, and the previously employed separation method.

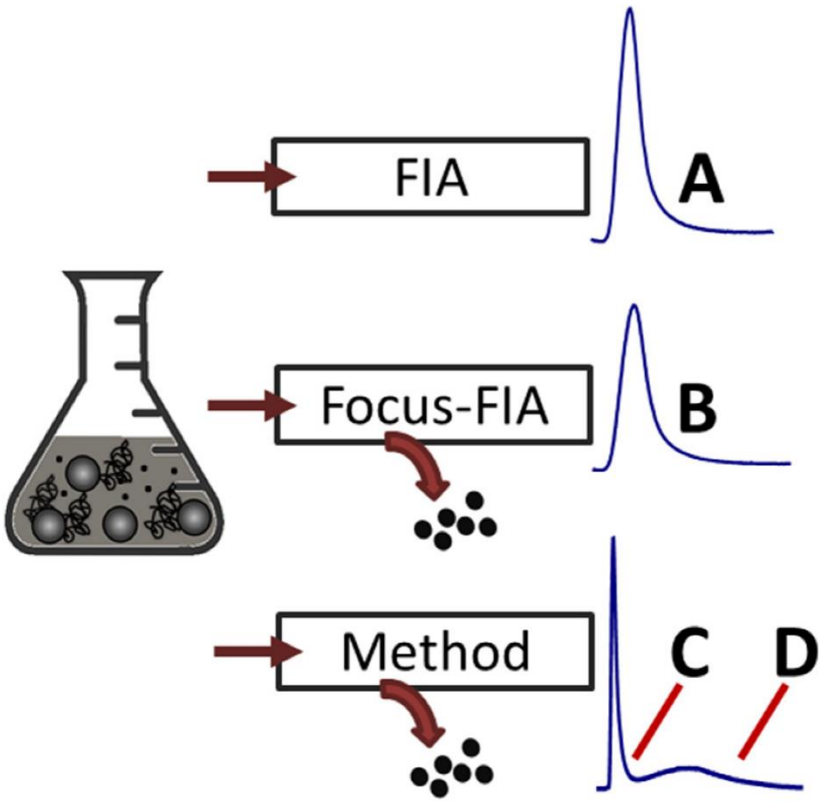

Figure 3.6. Schematization of the FFF fraction collection approach used to obtain comparable fractions of whole sample (A), filtered sample (B), polymeric PDA (C), and Ag-PDA (D). Dots represent small molecules and Ag ions.

The isolation process is schematized in Figure 3.6. The inhibitory activity of these fractions was tested in vitro against Gram-positive (S. aureus) and Gram-negative (E. coli) bacteria. Only fraction D, containing purified Ag-PDA NPs, exhibited significant antibacterial activity (Figure 6a). Gram-negative E. coli was more sensitive than Gram-positive S. aureus, as Gram-negative bacteria have narrower cell walls, making them more susceptible to Ag-based compounds [264].

Further testing of serial dilutions of fraction D confirmed dose-dependent antibacterial activity against E. coli (Figure 3.7b).

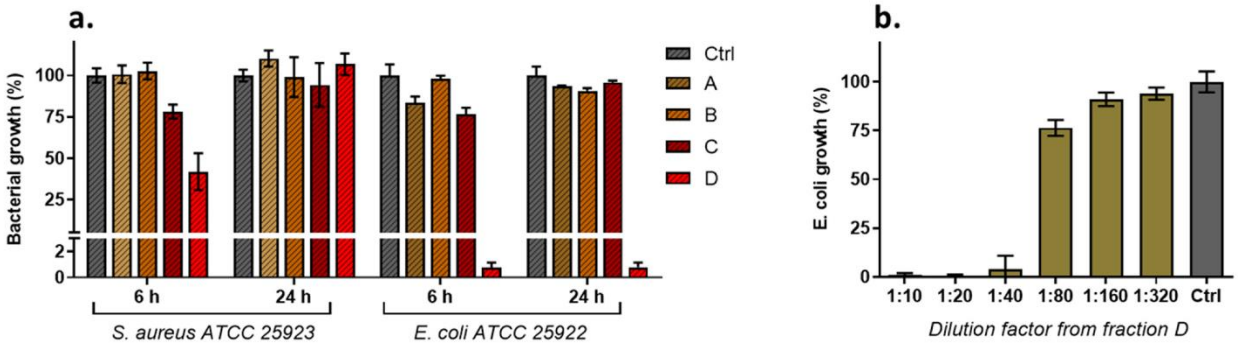

Figure 3.7. (**a**) Antibacterial activity of the samples (ten-fold diluted in MH broth) against S. aureus (left) and E. coli (right) reference strains after 6 and 24 h of incubation. Data are expressed as percentages of the bacterial growth relative to the positive control. (**b**) Antibacterial activity of fraction D (serial two-fold dilutions) against E. coli reference strain following 24 h of incubation.

3.4 Conclusions

We devised a fast, non-destructive method able to (1) monitor the synthesis of the nanocomposite in a TLC-like fashion and (2) Provide the characterization and purification of isolated Ag-PDA using the same, optimized separation method based on HF5-MD analytical platform. Orthogonal UV and light scattering detectors offered the simultaneous size determination and identification of the different species obtained during the conjugation, which were confirmed through conventional, offline characterization. The comparison between unfractionated, filtered, and isolated NPs confirmed the antibacterial effectiveness of Ag-PDA, especially towards Gram-negative E. coli, but also highlighted the importance of isolating these particles to avoid interference and the loss of activity. The HF5-MD approach allowed the reaction to be carried out to completion, avoiding wastage of time and chemicals; allowed fast on-line characterization; and provided isolated, purified, and biologically active Ag-PDA particles in water, ensuring their safe use as biocompatible antibacterials.

Chapter 4. AF4 as a tool to predict the behavior and stability of nanomedicines in biological environments

4.1 Introduction

Magnetic NPs (MNPs) represent one of the most extensively researched classes of nanomaterials for biomedical applications due to their unique physicochemical properties, which make them suitable for various applications in biotechnology, magnetic separation, targeted drug delivery, diagnostics, optical imaging, and as cytotoxic agents [265]. Furthermore, MNPs can be synthesized and modified with various chemical functional groups, enabling their conjugation with antibodies, ligands, and drugs of interest, thereby facilitating their use in theragnostic applications, which combine diagnosis and therapy, particularly in cancer treatment [266-268]. Iron oxide particles, such as magnetite (Fe_3O_4) and its oxidized form (α-Fe2O3), are among the most commonly used magnetic carriers in biomedical applications, offering good biocompatibility and low toxicity [269]. They are central to one of the most promising cancer therapies: magneto fluid hyperthermia (MFH), which uses magnetic NPs to heat biological tissues and destroy cancer cells which are more sensitive to elevated temperatures than healthy cells and they undergo apoptosis when exposed to temperatures above 43–46 °C [270]. MFH can be used alone or in combination with other treatments such as chemotherapy and radiotherapy to enhance its efficacy. To be effective in the human body, Fe_3O_4 MNPs should have a narrow size distribution and good dispersibility in aqueous media. The narrow size distribution of the iron oxide core ensures high heating capabilities in a low concentration under biocompatible, alternating magnetic field (AMF) conditions [271].

However, MNPs face two major issues: loss of magnetism due to oxidation and long-term inherent instability, caused by high surface energy and strong magnetic attraction between particles. High salt concentrations, typical of biological matrices, further compromise the colloidal stability of MNPs [271]. These instability challenges can be addressed through surface functionalization [272-275]. Various biocompatible chelating agents (lipids, gelatin, dextran, chitosan, polyvinyl alcohol, etc.) are used to form polymeric layers on the surface of magnetic NPs, improving their

stabilization for biological applications [276, 277]. Among different coatings, polyethylene glycol (PEG) stands out due to its hydrophilicity, biocompatibility, non-antigenicity, and antifouling properties [278]. PEG-coated iron oxide NPs have demonstrated the ability to significantly extend circulation time in the bloodstream [272]. Another noteworthy coating is the biodegradable copolymer poly-lactic-glycolic acid (PLGA), commonly used for preparing biodegradable carriers, which allows for tunable drug release properties and the modulation of the biological behavior of Fe_3O_4 NPs [273, 279, 280].

Properly coated MNPs, designed for biomedical use, are usually dispersed in a biocompatible fluid and injected directly into the tumor or bloodstream [281]. Upon entering the bloodstream, they encounter serum proteins such as human serum albumin (HSA), which constitutes 60% of the protein content. As infusion progresses, the mixing of particles with serum proteins leads to the formation of a protein corona, giving MNPs a new biological identity influenced by this new biochemical environment. The formation of this protein corona is critical for clinical applications, as it can alter the properties and bioavailability of NPs, either positively or negatively [282], [283]. This process is a complex, dynamic scenario [274], and when MNPs encounter a change in the medium, then initial destabilization, precipitation, or aggregation of the MNPs can occur, potentially leading to adverse reactions or toxicity for the patient.

Assessment of this transition is challenging because the number of interacting components is vast, and a range of parameters is needed to fully understand the process. Studies investigating MNP stability in biological matrices [284] and the formation and evolution of the protein corona [285] typically utilize batch sizing and imaging tools [286]. These methodologies reveal whether NPs undergo modifications, but they only provide averaged results, without capturing the evolution of individual populations [287]. This represents a significant limitation, given the complexity of the matrices and because NP samples are not always as monodispersed as assumed. AF4/HF5 offer a solution to these limitations since they allow for the separation of a wide range of analytes (from 1 nm to tens of µm, spanning 15 orders of magnitude in molar mass) under native conditions based on their interactions with an external field [288, 289]. Additionally, detector coupling can provide a powerful multiparametric characterization which is of outmost importance while dealing with evolving systems (such as NPs in biological media during the firsts moments after inoculation).

In this work PP-MNPs were analyzed using an HF5 platform in the presence of increasing amounts of HSA to simulate early stages of intravenous administration and to investigate their stability and behavior under simulated use conditions. At first, PP-MNPs as well as their changes in size and z-potential due to HSA-titration were monitored by batch techniques. This experiment was then translated into a separative mode using a specifically designed HF5 MD method to observe the behavior of PP-MNPs at increasing concentrations of HSA to the initial stages of administration. This platform enabled the separation of NPs-HSA conjugates from the remaining components and simultaneous characterization of each separated species through spectroscopy and laser scattering (molecular weight and gyration radius). Additionally, the determination of corresponding morphologies through v-value calculations [290] provided valuable insights into the shape of PP-MNPs and their conjugates, the mechanisms of HSA binding to PP-MNPs, and it addressed safety concerns.

4.2 Materials and methods

Materials

Fe_3O_4 PEG-PLGA NPs (PP-MNP) were provided by Colorobbia Consulting S.r.l. (Spicchio-Sovigliana, Vinci, Italy) in the form of a suspension at an Fe_3O_4 concentration of 2000 mg/L, prepared according to the patented procedure [291, 292]. Briefly, magnetite-based MNPs suspended in diethylene glycol were functionally modified with [N-(3,4-dihydroxyphenethyl dodecanamide (DDA)] and dispersed in tetrahydrofuran (THF). Subsequently, a THF solution of PLGA-b-PEG-COOH block copolymer was added to the magnetite-DDA NPs suspension. The formation of hybrid Fe_3O_4 PEG-PLGA was achieved using the nanoprecipitation method: two fluid streams ((1) an organic dispersion of functionalized magnetite and PLGA-b-PEG-COOH, and (2) a phosphate-buffered solution in a volumetric ratio of 1:10) were mixed and collected. The formed dispersion was dialyzed (Cogent M system, Pellicon membrane 2 Mini, cut-off 100 kDa) to remove the organic phase using a pure phosphate-buffered aqueous solution. The system was then concentrated to the final concentration and filtered through a polyethersulfone membrane syringe

filter (0.22 μm). The entire process was carried out under sterile conditions. HSA was purchased from Sigma-Aldrich (Milan, Italy).

Preparation of PP-MNP Stock Suspensions

The provided PP-MNP suspension was diluted to 256 ppm in an aqueous solution containing 0.05 wt% of filtered HSA by vortexing for 30 seconds.

X-ray Diffraction (XRD) analysis

XRD analysis was performed on powder obtained by drying the PP-MNP suspensions. The measurement was conducted at room temperature using a Bragg/Brentano diffractometer (X'pertPro PANalytical) equipped with a fast X'Celerator detector and a Cu anode as the X-ray source (Kα, $\lambda = 1.5418$ Å). The diffractogram was recorded in the 20–70° 2θ range, with a counting time of 0.2 seconds for every 0.05° 2θ step.

Colloidal Characterization

The colloidal behavior of PP-MNPs was evaluated in stock and stock suspensions diluted in MilliQ water at concentrations of 256 mg/L and 50 mg/L to determine the hydrodynamic size distribution and z-potential. These measurements were carried out using DLS and ELS techniques, respectively. The Zetasizer Nanoseries (Malvern Instruments, Malvern, UK) was used for the analyses. Each sample was prepared and analyzed in triplicate, with the particle size diameter (dDLS) and z-potential (ZpotELS) values calculated by averaging three measurements.

HSA Titration

PP-MNP stock (2000 mg/L) was diluted to 200 mg/L. Four different batches of HSA were prepared in phosphate buffer to be mixed with magnetite at Fe_3O_4/HSA weight ratios of 2:1, 1:1, 1:2, and 1:4, as shown in Table 4.1. The samples were prepared by mixing and homogenizing equal volumes (1 mL + 1 mL) of the two compounds at different concentrations using a vortex for 30 seconds.

PP-MNP:HSA Weight Ratio	PP-MNP		HSA	
	Volume (mL)	Concentration (mg L^{-1})	Volume (mL)	Concentration (mg L^{-1})
2:1	1	200	1	100
1:1		200		200
1:2		200		400
1:4		200		800

Table 4.1. Experimental concentration setup for the DLS/ELS measurements.

The hydrodynamic diameter and z-potential measurements were carried out in Phosphate Buffer (Sodium Phosphate 1 mM, pH 7.4) by DLS/ELS.

TEM

PP-MNPs were observed using an FEI TECNAI F20 microscope (FEI Company, Hillsboro, USA) operating at 200 keV. The suspension was applied to a holey carbon-coated grid, and the specimen was then dried at 60 °C. Images were collected in both phase-contrast mode and high-angle annular dark-field scanning transmission mode (HAADF-STEM). High-resolution electron microscopy (HREM) and Selected Area Electron Diffraction (SAED) analyses were performed to investigate the crystalline phase structure and composition. The mean particle diameter was calculated based on more than 100 particles.

HF5 setup

HF5 analyses were conducted using an Agilent 1200 HPLC system (Agilent Technologies, Santa Clara, USA), which consisted of a degasser, an isocratic pump paired with an Agilent 1100 DAD UV/Vis spectrophotometer, and an Agilent 1200 Fluorimeter, combined with an Eclipse® DUALTEC separation system (Wyatt Technology Europe, Dernbach, Germany). This system was followed by an 18-angle multiangle light scattering detector, model DAWN HELEOS (Wyatt Technology Corporation, Santa Barbara, USA). The HF5 cartridge (Wyatt Technology, Europe) with a 10 kDa membrane cutoff was used.

ChemStation software version B.04.02 (Agilent Technologies) was utilized to configure and control the instrumentation, and to calculate various separation parameters, in conjunction with Wyatt Eclipse @ ChemStation version 3.5.02 (Wyatt Technology Europe). ASTRA® software

version 6.1.7 (Wyatt Technology Corporation) was used to handle the signals from both the MALS and UV detectors and to compute the RMS radius of the sample also referred to as Rg.

The HF5 method was characterized by a longitudinal flow of 0.35 mL/min, while the cross/focus flow rates (Vx) are detailed in Table 4.2.

Δt (min)	Mode	Vx start (mL/min)	Vx end (mL/min)	Detector flow (mL/min)	Focus Flow (mL/min)
1.00	Focus	/	/	0.35	0.80
5.00	Focus+Inject	/	/	0.35	0.80
6.00	Elution (Linear)	0.55	0.04	0.35	/
18.00	Elution	0.04	0.04	0.35	/
3.00	Elution	0.00	0.00	0.35	/
2.00	Elution+Inject	0.00	0.00	0.35	/

Table 4.2. Flow conditions for the HF5 analyses.

4.3 Results and discussion

Batch and Static Characterization

The initial steps in characterizing the evolution of PP-MNPs involved the construction of a data set using common characterization techniques, among which X-ray diffraction, imaging, and batch measurements of size (DLS) and z-potential.

XRD. The primary peaks identified on the target NPs were consistent with the magnetite phase (JCPDS card no. 19-0629), with XRD reflections at 2Theta = 30.1°; 35.4°; 43.0°; 56.9°; and 62.5°, as shown in Figure 4.1. The collected peaks were typically broad, consistent with the nanosized dimensions of the particles.

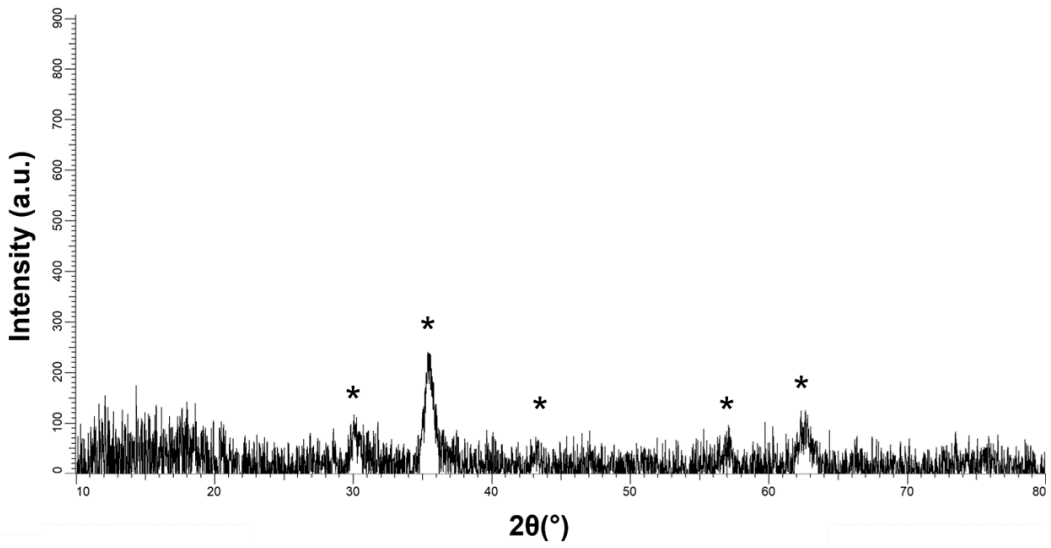

Figure 4.1. XRD diffractogram of MNPs (Fe3O4-PEG/PLGA). * = magnetite (JCPDS card n. 19-0629).

TEM. Images acquired in phase-contrast mode (Figure 4.2a) and HAADF-STEM mode (Figure 2b) revealed a regular spheroidal morphology of the particles with a mean diameter of 12 ± 4 nm. The higher magnification HREM (High-Resolution Electron Microscopy) image (Figure 4.2c) showed a cubic crystal structure consistent with the magnetite lattice. Crystalline magnetite was the sole phase composition resulting from the SAED analysis of the collected polycrystalline pattern rings (inset of Figure 4.2c).

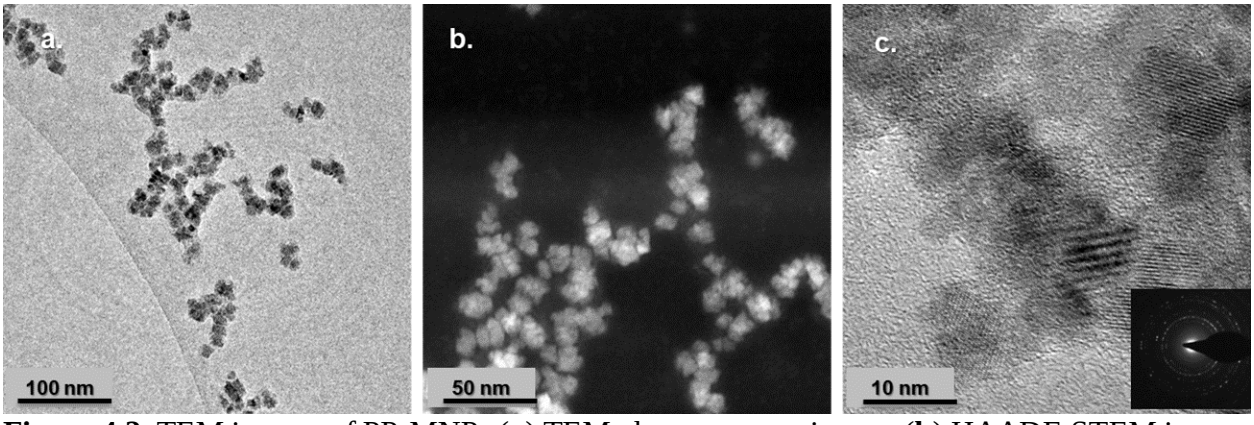

Figure 4.2. TEM images of PP-MNPs (**a**) TEM phase-contrast image; (**b**) HAADF-STEM image; (**c**) HREM image and in the inset SAED polycrystalline pattern rings. Scale bars: (**a**) 100 nm; (**b**) 50 nm; (**c**) 10 nm.

Size and z-potential. PP-MNPs dispersed in phosphate buffer and evaluated at two concentrations showed a neutral pH, a hydrodynamic diameter of about 75 nm, and a negative z-potential (~50 mV), as reported in Table 4.3. These results are consistent with previously published works on PEG-PLGA coating [293, 294].

Sample	Concentration (ppm)	d_{DLS} (nm)	PDI	z-potential (mV)	pH
PP-MNP	50	74 ± 1	0.1	−49.5 ± 3.3	7.3
	256	76 ± 2	0.2	−49.0 ± 2.4	7.4
HSA	800	9.8 ± 2.4	0.7	−31.5 ± 9.6	7.3
	100	10.4 ± 2.2	0.7	−33.5 ± 4.7	7.3

Table 4.3. Colloidal properties (hydrodynamic diameter, d_{DLS} and z-potential) of PP-MNPs and HSA.

As expected, the hydrodynamic diameter, comprehensive of the grafted polymers, was larger than the size assessed by TEM.

We also evaluated the colloidal properties of HSA at the highest and lowest concentrations used in dynamic-flow conditions. As expected, HSA was predominantly present as a monomer in phosphate buffer with a size around 10 nm and a negative charge at both concentrations. Notably, for PP-MNPs, we obtained similar data at both concentrations, indicating that the main colloidal properties were unaffected by dilution. The change in stability and the aggregation state were due to the medium change following interactions in the biological setting.

Titration with HSA in static conditions. Using DLS/ELS measurements, we monitored the colloidal evolution of magnetite NPs titrated with HSA according to the mass ratios reported in Table 4.2. A previous work [295] reported that the addition of albumin increased the DLS diameters recorded for the suspended NPs. However, when titrating PP-MNPs with HSA in phosphate buffer, we observed a decrease in the hydrodynamic diameter at higher HSA amounts (Figure 3), consistent with a dispersion action or size rearrangement promoted by protein adsorption on the NPs.

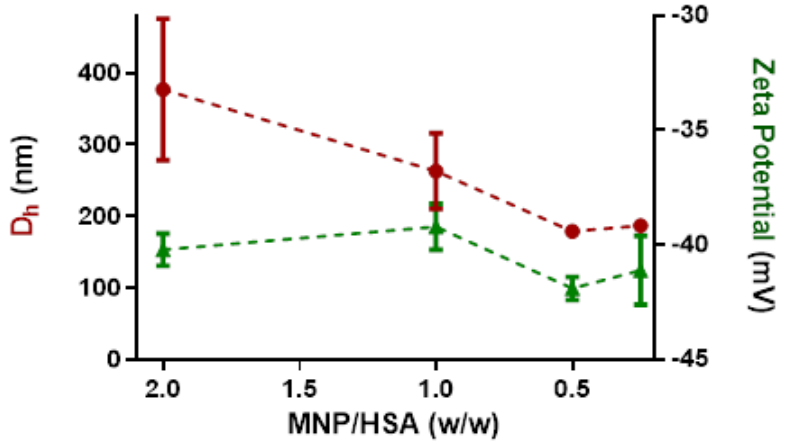

Figure 4.3. Titration of PP-MNPs with HSA in water. Red points: hydrodynamic diameter. Green triangles: z-potential.

Based on DLS results, it is reasonable to conclude that the increasing presence of HSA provides shielding and enhances colloidal stability. For PP-MNPs with HSA ratios < 1, e.g., at predominant concentrations of HSA, the hydrodynamic diameter reached a plateau at around 180 nm (Table 4.4).

PP-MNP/HSA	pH	Size d_{DLS} (nm)	Deviation (nm)	PDI	z-potential (mV)	Deviation (mV)
2	6.4	377	99	0.500	−40.2	0.7
1	6.7	263	53	0.450	−39.2	1.0
0.5	6.7	179	9	0.370	−41.9	0.5
0.25	6.6	187	4	0.400	−41.1	1.5

Table 4.4. DLS/ELS data for the titration of PP-MNPs with HSA.

The PP-MNP-HSA suspensions exhibited z-potentials stabilized at around −40 mV, close to the value of MNPs and slightly reduced due to the presence of HSA, which is characterized by a lower z-potential. Notably, the size deviation observed for lower ratios (0.5 and 0.25) was much lower, indicating that the formed structures were more stable and well-defined.

Native and Dynamic Characterization with FFF-MD

To simulate intravenous injection administration, the titration experiment was adapted from static conditions to an in-flow approach using HF5 as the separation device to isolate different populations, followed by online detection to monitor changes in UV/Vis absorption, fluorescence, and measured size. PP-MNPs were characterized alone and in the presence of increasing amounts of HSA to understand their stability and behavior once injected into a simulated biological medium. The selected points, which matched those used for batch characterization, aimed to capture the first moments of administration when PP-MNPs changes from being the main species to being surrounded by the biological medium. The analyses were conducted in phosphate buffer (Sodium Phosphate 1 mM, pH 7.4). The same quantity of PP-MNPs was injected in all the analyses, as shown in Table 4.2. All mixtures were prepared with a 1:1 volume ratio to avoid changes due to varying medium proportions.

The separation method was designed and optimized to elute HSA and PP-MNPs at distinct retention times. Method precision was assessed by performing triplicate tests on retention times and signal intensity, both showing deviations of <1%. The limit of quantification (LoQ), defined as 10× the baseline noise, was found to be 8.4 ng (0.42 pmol) for HSA and 48 ng for PP-MNPs. The final method combined gradient and isocratic crossflow, allowing for their baseline separation and elution within 30 minutes.

For the mixed suspensions, the appearance of new bands or the coexistence of characteristic signals from both species directly indicated interaction between them. To gather information about the composition of the combined species, it was necessary to assign peaks to one species, the other, or both, and “diagnostic” signals were selected. First, HSA exhibits intrinsic FLD (excitation at 280 nm, emission at 340 nm), which is typical for proteins [296], while PP-MNPs have only faint emission at 550 nm. Second, PP-MNPs absorb at 480 nm, whereas HSA does not, making 480 nm the optimal wavelength for monitoring PP-MNPs. The results are shown in Figure 4.4.

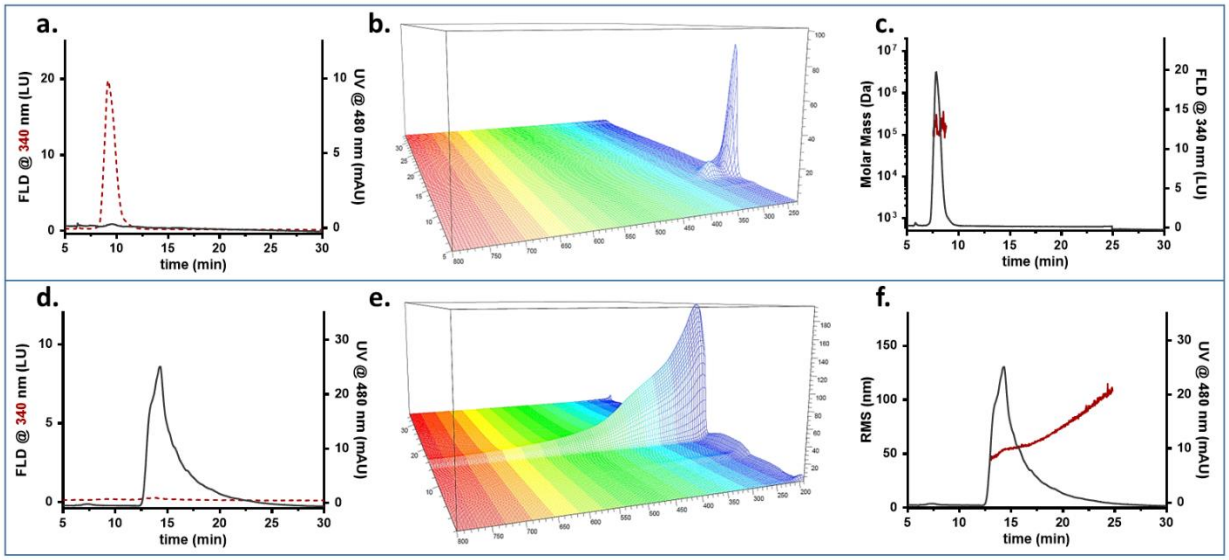

Figure 4.4. FFF fractogram (red dashed line: FLD signal; grey line: absorption signal), UV/Vis absorption spectrum, and Molar Mass/RMS radius (red) and FLD/UV profile (grey) obtained for HSA (**a–c**) and MNPs (**d–f**).

Figures 4.4a and 4.4d display for the optimized method the fractogram profiles recorded as absorption at 480 nm and FLD at 340 nm, respectively. The distinct profiles for the two signals and samples demonstrate that the method effectively baseline-separated HSA and PP-MNPs, with both species exhibiting characteristic signals that could be monitored individually.

HSA eluted at 9 minutes as a single peak (Figure 4.4a), with an absorption spectrum (Figure 4.4b) typical of a protein, showing a local maximum at 280 nm and no absorption beyond the UV range. The molar mass averaged around 100 kDa (Figure 4.4c), indicating the presence of HSA as a mixture of monomer (66.7 kDa, predominant) and oligomers, as previously observed under similar conditions with native separation [297].

PP-MNPs eluted as a single band with a broad size distribution (red distribution, Figure 4.4f), peaking at 15 minutes (Figure 4.4d). The UV/Vis spectrum (Figure 4.4e) was broad and intense, with scattering at higher wavelengths. The population of NPs was found to be monomodal (Figure 4.4f), with the majority of PP-MNPs (min 14.0 to 17.5, 75% of peak area) having an Rg of 51 ± 5 nm, while the peak tail extended to 110 nm and contained aggregated forms with a higher radius, formed following exposure to the saline environment. Overall, these results agreed with DLS data,

which measured an Rh of 75 nm. The shape factor obtained [198], expressed as the Rg/Rh ratio, was equal to 0.7, corresponding to a solid sphere.

We then monitored the system evolution after mixing PP-MNPs with increasing amounts of HSA. The results for PP-MNP:HSA mixtures at 2:1 and 1:1 mass ratios are shown in Figure 4.5. MALS measurements provide an overlay of the radius calculation on the 480 nm signal used to monitor NP elution and their size/aggregation state. This signal allowed for monitoring the evolution in all the mixtures. For each PP-MNP:HSA mixture, the fractogram overlaying the HSA FLD signal and PP-MNP absorption, the UV/Vis absorption spectrum, and the radius distribution are displayed (Figure 4.5).

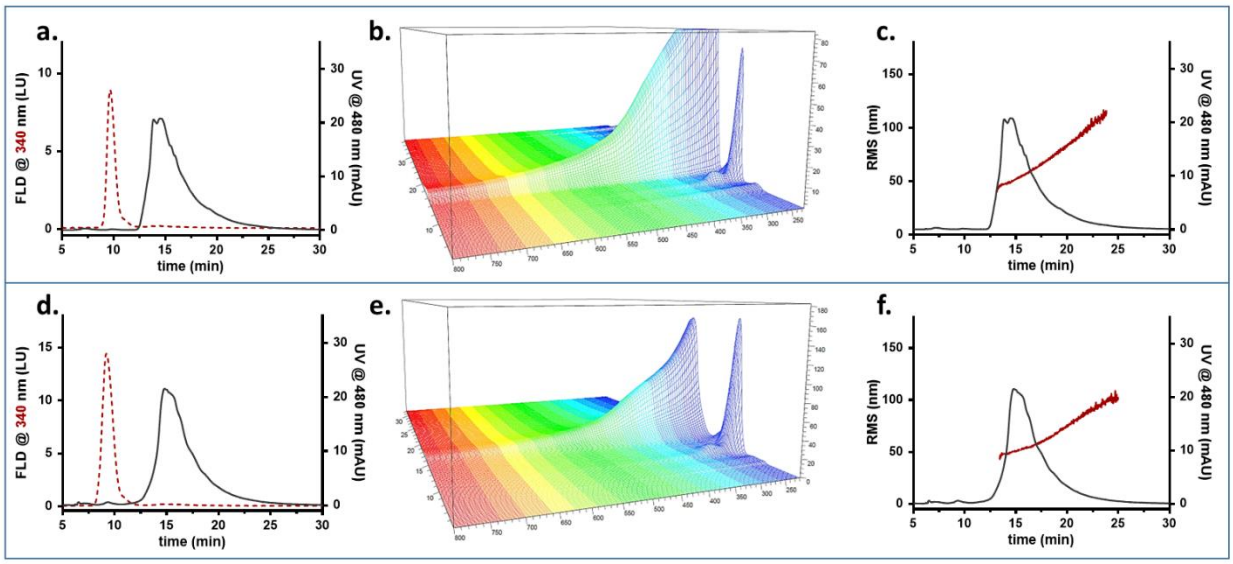

Figure 4.5. FFF fractogram (red dashed line: FLD signal; grey line: absorption signal), UV/Vis absorption spectrum, and Molar Mass/RMS radius (red) and FLD/UV profile (grey) obtained for suspensions at PP-MNP:HSA 2:1 (**a–c**) and 1:1 (**d–f**) mass ratios.

At a 2:1 proportion, PP-MNPs and HSA are eluted at different times (Figure 4.5a, red dotted line for HSA and grey line for MNP) and show no significant interactions, apart from a slight absorption at 480 nm at the HSA retention time, which represents about 0.2% of the integrated area of the 480 nm signal. The 3D output (Figure 4.5b) shows the two different absorption spectra. The PP-MNPs appear as a single band with a broad size distribution like what it is observed for PP-MNPs alone (Figure 4.5c). The majority of PP-MNPs are eluted between minutes 14 and 17.5,

corresponding to an average radius of 50 nm, while the peak tail reaches a dimension of 110 nm (red distribution).

For the PP-MNP:HSA mixture at a 1:1 ratio, a small peak at 480 nm is detected at 9 min (Figure 4.5d), which indicates that some NPs are eluted earlier, likely due to conformational or surface modification. The absorption spectrum shows a slight alteration in the HSA profile (with absorption at higher wavelengths, similar to the broad absorption of PP-MNPs), which suggest some interaction between the two phases; however, the signal intensity is too low for a reliable radius calculation. A main monomodal band instead appears at 15 min with a broad size distribution, as shown by the MALS calculation (Figure 4.5f). Most PP-MNPs (from min 14.0 to 17.5) have an average radius of 50 nm, with the peak tail reaching 100 nm.

Data collected on the 1:2 PP-MNP:HSA ratio, which corresponds to a doubled HSA content, reveal a completely different scenario, clearly showing interactions between the compounds (Figure 4.6a-c).

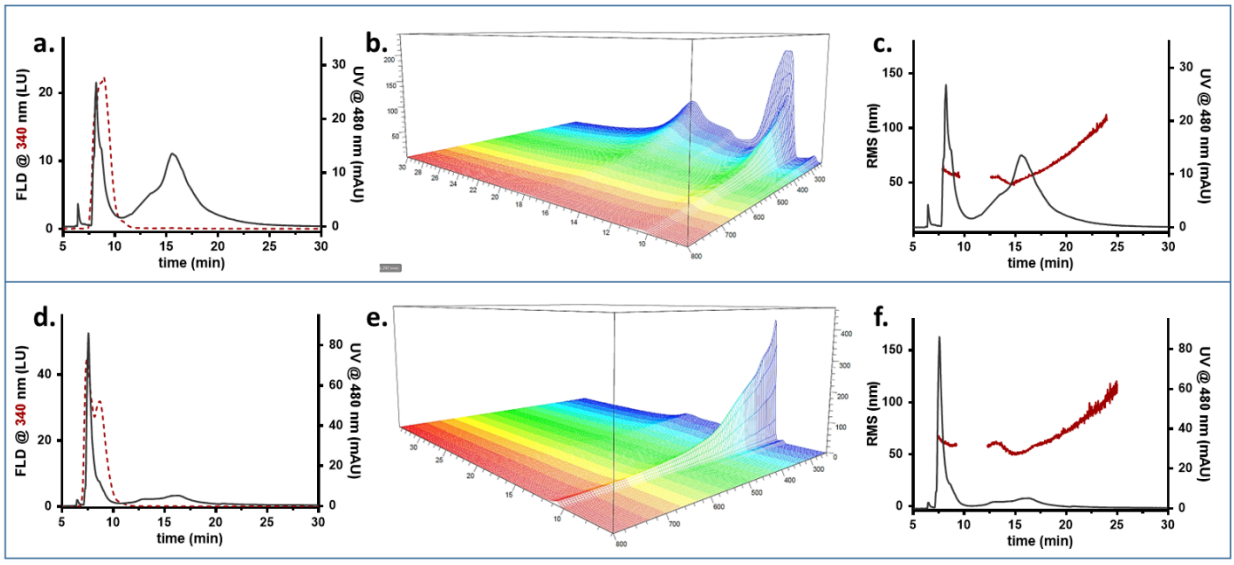

Figure 4.6. FFF fractogram (red dashed line: FLD signal; grey line: absorption signal), UV/Vis absorption spectrum, and Molar Mass/RMS radius (red) and FLD/UV profile (grey) obtained for 1:2 PP-MNP:HSA (**a–c**) and 1:4 PP-MNP:HSA (**d–f**) suspensions.

A new band, absorbing at 8 min at 480 nm, is visible in Figure 6a, preceding the HSA peak (Figure 4.6a), and the PP-MNP band at 14 min decreases proportionally, as the total integrated area

remains constant across all the analyses. Based on the FLD signal, we hypothesize that this new band also contains HSA, indicating that PP-MNPs and HSA interact to form a differently arranged system with a distinct retention behavior, involving both species. The absorption spectrum appears as a combined band of HSA and PP-MNPs (Figure 4.6b). MALS calculations indicate that the newly formed species have an RMS radius comparable to the previously characterized PP-MNPs (55 nm vs. 58 nm, Figure 4.6c). The earlier retention time for species with the same RMS radius suggests a different shape and/or surface charge, affecting retention behavior in HF5. DLS and z-potential results show a decreasing hydrodynamic radius, suggesting that HSA may participate in coating PP-MNPs, competing with PEG/PLGA (the formal coating), and creating a hybrid coating less influenced by the polymer encapsulation. We hypothesized the formation of an HSA protein corona on PP-MNPs, resulting in an HSA-PP-MNP composite.

Finally, the PP-MNP:HSA 1:4 ratio shows further progression in the PP-MNP shift toward the earlier peak. The signal corresponding to HSA is split into a PP-MNP-containing fraction (eluted at 8 min) and its typical retention peak at 10 min, where the PP-MNPs was tailed (Figure 4.6d). The UV/Vis spectrum shows a migration of the absorption profile toward the earlier peak (Figure 6e); in terms of RMS radius, the two species eluted at 8 and 15 min measure 60 nm and 59 nm, respectively (Figure 4.6f). A secondary shoulder of 60 nm at 12 min arises from the later band, suggesting a reconversion of PP-MNPs toward the newly formed band.

Eluted PP-MNPs exhibit an increase in peak intensity compared to the 1:2 mixture, along with a second maximum at their characteristic retention times. UV absorption data indicate that PP-MNPs primarily exist as an HSA-PP-MNPs composite (8 to 10 min) rather than as standalone particles (12 to 20 min). Under HSA-excess conditions (PP-MNPs:HSA $\geq$ 1:2), formation of an HSA-PP-MNPs composite occurs. The presence of HSA leads to the formation of a protein corona around the PP-MNPs, which reduces agglomeration by maximizing electrostatic and steric repulsion [298]. Consequently, the HSA-PP-MNPs system is characterized by well-dispersed NPs with a net negative charge.

The FFF-MD data suggest that when HSA levels are low, the two phases (HSA and PP-MNPs) separately exist. As the concentration of HSA increases, interactions begin to occur, with HSA becoming part of the existing PEG/PLGA coating and forming a protein corona around the PP-MNPs, with the eventual encapsulation of most of the MNPs within the HSA matrix. This

transition is also evident from the conformational analysis of the HSA-PP-MNPs (7.5–10 min interval) and PP-MNPs (14–18 min interval), for all mixtures referred to as population 1 and population 2, respectively, as shown in Figure 4.7.

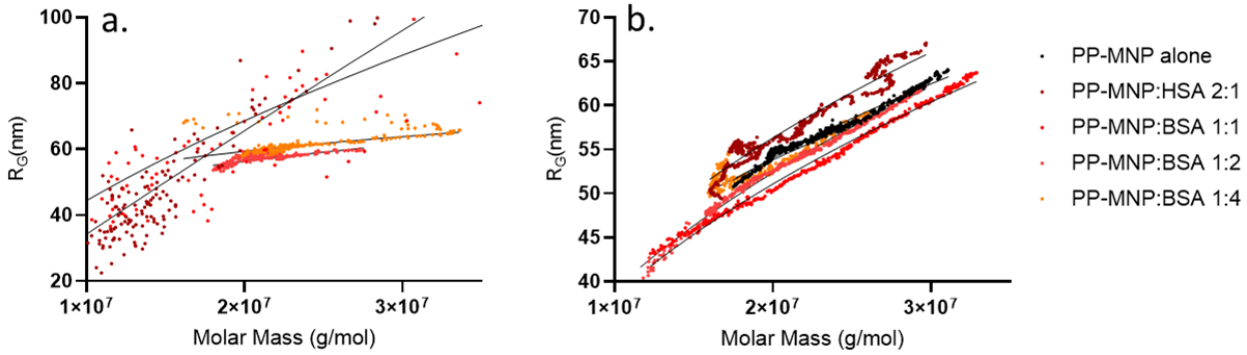

Figure 4.7. Conformation plots obtained for population 1 (**a**) and population 2 (**b**) expressed as double logarithmic molar mass/gyration radius regression lines.

Population 2 (free PP-MNPs, non-interacting with HSA) showed a v-value of 0.4, which decreased to 0.33 (0.40–0.41–0.40–0.36–0.33) at the highest measured ratio. These results describe a spherical shape that changed into a solid sphere as the concentration of free PP-MNPs decreases, with no significant conformational changes beyond what it is expected from a decreasing concentration. Meanwhile, as HSA concentration increases, population 1 begins to form. This change in conformation is notable, starting as an elongated (and polydisperse) structure (v-values of 0.9 and 0.7 for 2:1 and 1:1 ratios, respectively), likely representing HSA that encapsulates the PP-MNP system. The conformation plot then evolves into a core-shell structure, where dense PP-MNPs are surrounded by a less dense, stable PEG/PLGA-HSA coating (v-values of 0.21 and 0.19 for 1:2 and 1:4 ratios), which remains stable even with increasing the HSA:PP-MNP ratios.

This information is crucial, as the shape, surface, and conformation of NPs significantly influence their activity. When combined with DLS size data, these results confirm that MNPs maintain a spherical shape, and the previously noted retention time shifts are not due to conformational changes but rather to a change in apparent radius. The retention times of the observed species are inconsistent with the radii measured by MALS, suggesting the possibility of a reversed elution mode. This reversed elution indicates that the species may appear hydrodynamically large while being physically smaller, which could be explained by PEG surrounding the particles. Weak

interactions between particles and free PEG/PLGA could contribute to the appearance of a larger hydrodynamic radius, eluted in reverse mode. Evidence for surface interactions with increasing HSA concentration (rather than mere coelution) can also be seen in the conjugate emission spectra, which resemble that of HSA (PP-MNPs alone do not emit, see Figure 4d) but feature additional peaks (not shown). This interaction may arise from electrostatic interactions between MNPs and the negative charge of HSA at physiological pH (with a pI of 4.7), as well as chemisorption of thiol groups from albumin onto the MNP surface. Additionally, the absorption spectrum, typical of PP-MNPs, confirms the presence of a complex structure involving both PEG/PLGA and HSA over the MNPs. Literature describing the behaviour of PEG/PLGA coatings while in presence of proteins is variegated. Protein-repellent properties of coatings like PEG have been reported to prevent nonspecific interactions of serum proteins with NPs, thereby reducing immune system interactions and extending circulation time in the bloodstream [299]. However some studies have also shown that BSA can quickly couple with PEG-encapsulated NPs, enhancing their stability and biocompatibility in cell culture media and intracellular environments by preventing aggregation [300], [301]. This corroborates the mechanism hypothesized above.

Lastly, we analyzed the signal area at 480 nm for all mixtures. The total area values were consistent (within a 3% deviation), which demonstrates that the increase in HSA did not affect PP-MNPs absorption at this wavelength, and recovery remained constant in all the FFF analyses. We then examined the percentage area of HSA-PP-MNPs eluted at 8 min, as shown in Figure 4.8. To assess the binding trend, we increased the PP-MNPs:HSA ratio to 1:6, 1:8, and 1:10, at which point population 2 was no longer visible, and the only remaining species was the core-shell structure observed in population 1.

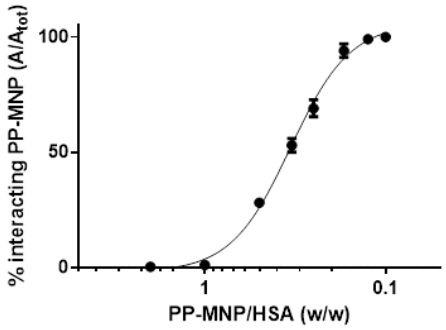

Figure 4.8. HSA/PP-MNP interaction vs. HSA increase expressed as the percentage of PP-MNPs interacting with HSA (black dots and error bars, n=3) calculated from independent runs of suspensions at 2:1, 1:1, 1:2, 1:4, 1:6, 1:8, 1:10 PP-MNPs:HSA mass ratio.

Until the amount of HSA doubles that of PP-MNPs, there is minimal interaction. This behaviour changes rapidly at a 1:2 ratio, indicating that a higher amount of protein is necessary for PP-MNPs to interact with HSA and form an HSA encapsulation around the PP-MNPs. At a 1:8 ratio, all PP-MNPs are converted into HSA-PP-MNPs, eluted as population 1.

With further increases in HSA and PP-MNP dilution in biological media, when the albumin concentration approaches the range in healthy human blood (34–54 g/L), all PP-MNPs are coated with an HSA protein corona, forming an HSA-PP-MNPs composite. This composite can be considered biocompatible due to the HSA shell, making it suitable for potential therapeutic applications [302].

However, there are some limitations to this study. The FFF method requires adjustments based on the sample type, which necessitate optimization when applied to other systems. While the current FFF setup requires minimal sample amounts, being a miniaturized device, it is not suitable for particle collection for further study. However, a scale-up in a flat, non-miniaturized channel could address this limitation. Despite these limitations, combination of these results with those from batch techniques clearly demonstrates the complementary nature of the obtained information. Whereas DLS and z-potential evaluations provide insight into the evolution of PP-MNPs when introduced into biological fluids, only the selective size/conformation analysis from FFF-MDMD enables visualization of the species present in a frame-by-frame manner. This allows for a detailed observation of the evolving PP-MNP surface and the significant excess of protein required to fully convert them to their biological identity.

4.4 Conclusions

In this study, a miniaturized FFF-MD method was used to demonstrate that the particles remain relatively stable in the medium, though some aggregation may occur. The particles progressively interact with proteins, forming a new biological identity through a process characterized by a highly imbalanced mass ratio. By combining conformation studies with batch characterization results, it was confirmed that morphology of the particles remained unchanged, which is closely linked to their activity and cytotoxicity. This approach and setup enable monitoring nanoparticle–

protein interactions at the earliest stages of infusion and allow for the evaluation of how concentration and ratio affect the size, shape, and arrangement of PP-MNPs. Compared to the traditional techniques, mostly reported in official guidelines, the HF5 platform was able to measure by itself all the QCAs of interest (excluding the z-potential), without the need to relay on multiple instruments, in a semi automatic and potentially scalable way. Additionally, z-potential could also have been determined by coupling to the device a commercial EAF4 module [303], making the instrument a *jack of all trades* in terms of QCAs detection. The other major feature of HF5-MD is the separation of the analyzed species. Unlike traditional techniques, the separation approach provided selective information and identification which allowed for precise monitoring of the evolution of injected MNPs at increasing levels of protein, and for simulating their dispersion in a biological medium.

Chapter 5. AF4 as a quality control (QC) system for the commercialization of peptide-based formulations

5.1 Introduction

Therapeutic peptides represent a significant area of interest in the pharmaceutical industry. To date, more than 50 candidates have been approved as therapeutics, and many others are undergoing clinical trials [304-306]. Compared to small molecule drugs, therapeutic peptides offer several advantages, such as higher specificity, low toxicity, and better tolerance by the human body [307]. Additionally, advances in manufacturing strategies, primary structure modifications, and computational approaches to formulation development have facilitated investment in these types of drugs [308, 309].

Peptide candidates can be produced either chemically or recombinantly (upstream process), depending on the sequence length and the presence of non-proteinogenic amino acids in the primary structure [310, 311]. Regardless of the production method, the crude peptides obtained require purification (downstream process) to meet the quality standards set by national regulatory authorities. Techniques such as ion exchange and size-exclusion chromatography, precipitation, and extraction are employed, although ion pair reversed-phase liquid chromatography remains the reference technique [312, 313]. After the peptide API is produced, purified, and typically lyophilized, it undergoes formulation into its Finished Dosage Form (FDF). This phase involves several studies, including pre-formulation (evaluation of physicochemical properties before and after excipient combination), analytical profiling (structural characterization and impurity determination), and assessment of pharmaceutical properties [314, 315]. The commercialization of protein drug candidates also faces significant challenges; changes in external or internal variables (such as temperature, pH, and chemical environment) may lead to denaturation, aggregation, or precipitation, destabilizing the protein structure and impairing its function [316].

Among these physical and chemical degradation pathways, peptide aggregation is especially critical, as it can potentially trigger immunogenicity in patients, making it one of the most vital attributes of peptide FDFs. During drug development, this undesired phenomenon is typically

mitigated by using suitable formulation buffers or by modifying the primary sequence of the peptide [317]. The importance of addressing peptide aggregation is further underscored by the FDA requirement that the aggregation properties of generic peptides match those of the Reference Listed Drug (RLD) already on the market [318]. Although the 2021 FDA guidance applies primarily to a limited number of generic peptides manufactured through alternative methods (e.g., synthetic vs. recombinant), it has now become the standard for evaluating all commercialized generic peptides.

There are numerous techniques for monitoring peptide aggregation, many of which are also used for protein aggregation analysis. Although peptides are smaller than proteins, they can still aggregate into high molecular weight species detectable by similar methods. Traditional techniques include microscopy and turbidimetry. However, microscopy is time-consuming and requires sample drying, while turbidimetry provides only limited information on the type of aggregates formed [319]. Historically, SEC has been the go-to method for detecting peptide aggregation. Despite being an effective tool in terms of sensitivity, precision, and throughput, SEC has notable technical limitations that can lead to inaccurate aggregate estimates in peptide products. The size resolution of SEC is restricted to approximately 10^7 Da (around 100 nm), and the mobile phase composition is limited by compatibility with the stationary phase, preventing analysis under native conditions. Additionally, adsorption or dissociation of samples on the stationary phase can occur [176, 320]. Consequently, regulatory bodies like the FDA and the EMA now mandate the use of techniques orthogonal to SEC, such as Sedimentation Velocity Analytical Ultracentrifugation (SV-AUC) and AF4, to confirm SEC data [28].

While SV-AUC has size limitations similar to SEC, AF4 covers a broader range, measuring particles from 1 nm to 20 µm. Additionally, AF4 operates without a stationary phase, eliminating adsorption and dissociation issues, and is highly flexible since the mobile phase can be tailored to sample requirements allowing analysis in native-like conditions. Moreover, comparative studies of protein and monoclonal antibody (mAb) aggregation using AF4 and SEC further highlight AF4 advantages in detecting larger aggregates and operating under more flexible conditions [321].

In this context, we focused on Liraglutide, a peptide API used to treat Type 2 diabetes and chronic obesity, marketed under the brand names Victoza and Saxenda [322, 323]. The Liraglutide FDF is available as an injectable solution containing 6 mg/mL of the API, along with phenol, propylene

glycol, and sodium phosphate for pH adjustment to approximately 8.15. Liraglutide is also listed in the FDA 2021 guidance, requiring extensive characterization of aggregation properties and comparison to the RLD for any generic candidates to ensure "sameness" and market approval [318]. Despite the pharmacological properties of Liraglutide being well established, little is known about its aggregation behavior, even for the currently marketed RLD. Existing studies primarily focus on how environmental pH influences Liraglutide aggregation and kinetics [324-326]. For instance, Steensgaard et al. [327] demonstrated that Liraglutide oligomerizes into heptamers within a concentration range of 0.004 – 4.501 mg/mL, while circular dichroism studies also provided valuable insights [328]. Furthermore, Frederiksen et al. [329] conducted molecular dynamic simulations to predict the stable aggregation states of Liraglutide, comparing these results with Small-Angle X-ray Scattering (SAXS) and FFF-UV-DAD analyses. These studies, performed on Victoza using PBS as the mobile phase, identified a hexameric structure for the aggregates. Theoretical studies suggested that hexa-, hepta-, and octameric structures were the most likely forms. However, several key aspects of the aggregation behavior of Liraglutide remain unexplored: (a) none of these studies were conducted with the API dissolved in the diluent used in the Victoza/Saxenda FDF (an aqueous solution at pH ~8.15 containing phenol and propylene glycol); (b) most samples were purified standards rather than commercial products; and (c) none of the studies used the FDF concentration (6 mg/mL), instead relying on more diluted systems. Therefore, while these findings represent important first steps in this field, they lack practical applicability for characterizing commercial products or developing general tools for evaluating aggregation properties between peptide samples.

For these reasons, in this study, we conducted measurements on several Liraglutide samples in their formulation, with two primary objectives: (1) to perform a sameness study while maintaining the native state of the samples in the FDF diluent; and (2) to evaluate the aggregation state of Liraglutide both before lyophilization and after formulation. To achieve these goals, we employed an AF4 platform coupled with UV, FLD, dRI, and MALS detection, which provided excellent recovery, detection limits, and mass- and size-wise characterization. This approach also overcame technical limitations associated with using formulation as the mobile phase. We selected a range of samples, including pre-lyophilization API in solution, an internally produced FDF, and two RLDs (Victoza and Saxenda), all of which were characterized in their native states. The results from the FDF and RLDs were also evaluated using SEC-UV-FLD-dRI-MALS analysis to provide

a comprehensive view of Liraglutide in suspension. This approach aligns with FDA recommendations and serves as a foundation for future studies on peptide aggregation to ensure representative results and product safety.

5.2 Material and methods

3.1. Samples

Bovine Serum Albumin (BSA, Merck KGaA, Darmstadt, Germany); aggregated Liraglutide: AF00195L, 6 mg/mL; API: ALICEP 00136C and API MC 00291D, lyophilized and resuspended to 6 mg/mL in water or formulation; finished dosage form sample: FDF lot #33124-46 and Lot #33387-18, 6 mg/mL; RLD (Fresenius Kabi, Bad Homburg, Germany): Victoza Lot #HS65J01 and Lot #KS6AH74, 6 mg/mL. RLD (Novo Nordisk, Bagsværd, Denmark): Saxenda Lot #JP54138 and Lot #JP54138, 6 mg/mL. The composition of the formulation buffer is as follows: disodium phosphate dihydrate, 0.476 g/L; propylene glycol, 0.47 g/L; phenol, 1.8 g/L; and water for injection. The lyophilized samples were resuspended to the same concentration as the FDF and RLD. The Liraglutide sample names, concentration, dilution media, and codename are listed in Table 5.1.

	State	Concentration	Medium	Name	Injection volume (µL)
API (Lot #ALICEP-001-36C)	lyophilized	6 mg/mL	Water, formulation	API1-w API1-f	30
API (Lot #MC-002-91D)	lyophilized	6 mg/mL	Water formulation	API2-w API2-f	30
Finished dosage form (FDF) (Lot #33124-46)	solution	6 mg/mL	Formulation	FDF	30
Victoza (Lot #HS65J01) (Lot #KS6AH74)	solution	6 mg/mL	Formulation	Victoza1 Victoza2	30
Saxenda (Lot #JP54138)	solution	6 mg/mL	Formulation	Saxenda	30
Stressed API (Lot #AF-001-95L)	solution	3 mg/mL	Formulation	APIaggr	60
Finished dosage form (FDF) (Lot #33387-18)	solution	6 mg/mL	Formulation		30
Saxenda (Lot #JP54138)	solution	6 mg/mL	Formulation		30

Table 5.1. Sample list. All chemicals were purchased from Merck KGaA, Darmstadt, Germany.

AF4-UV-FLD-RI-MALS Analysis

AF4-MALS was performed using a 1100 Series HPLC system (Agilent Technologies, Palo Alto, USA), connected to a module controlling AF4 flow rates and operations (Eclipse 3, Wyatt Technology Europe, Dernbach, Germany). On-line detection of the eluted species was performed with an Agilent 1100 DAD UV/Vis spectrophotometer, an Agilent 1200 FLD , a MALS DAWN HELEOS detector (Wyatt Technology Corporation, Santa Barbara, USA), and an Optilab rEX refractive index detector (Wyatt Technology Corporation, Santa Barbara, USA). Carrier solutions were degassed using an on-line vacuum degasser (Agilent, 1100 series, Agilent Technologies).

The separation device is a flat channel (Wyatt Technology Europe) with a trapezoidal shape and capillary height. For analysis, sample solutions are injected into the channel and focused, allowing the sample to concentrate into a narrow band. When elution begins, separation occurs due to the

combination of longitudinal and perpendicular hydrodynamic fields. The channel was 152 mm long and equipped with a PES membrane (Nadir), with a 1 kDa molecular weight cutoff. The channel spacer was 350 μm thick, with a trapezoidal shape (upstream width b_0 = 16 mm; downstream width bL = 4 mm).

SEC-UV-dRI-MALS

SEC analyses were performed using a Shodex HPLC Protein KW-802.5 column (300 × 8.0 mm, 5 μm). The mobile phase composition was 1 g/L L-Arginine: Acetonitrile: Acetic acid in a 35:50:15 ratio (isocratic, 0.5 mL/min). Molar mass was determined based on dRI detection for concentration measurement. The samples analyzed were Liraglutide FDF Lot #33387-18 and Saxenda Lot #JP54138, both provided in suspension at a concentration of 6 mg/mL.

5.3 Results and discussion

Method Development and Optimization of Detection Parameters

The AF4-MD method developed in this work utilized Liraglutide formulation as the mobile phase. On one hand, this approach accurately represents the aggregation state of the peptide in suspension. On the other hand, it complicates finding optimal separation and detection conditions, as the mobile phase is not optimized for the instrumental setup. Therefore, using a combination of different, uncorrelated detectors is recommended to overcome the limitations of individual techniques, such as signal interferences from absorbents in the mobile phase and baseline drift caused by eluent viscosity.

In the case of Liraglutide formulation (see Materials and Methods), the presence of phenol in the mobile phase caused absorption and emission in the same wavelength ranges as conventional values for proteins and peptides (280 nm absorption and excitation, 340 nm emission). The presence of ethylene glycol increased the mobile phase viscosity, causing baseline drifts in the concentration detectors (UV, dRI) during the separation methods, which are subject to flow and pressure changes. For this reason, absorption at 280 nm could not be utilized due to a high noise/signal ratio and the absence of a relative maximum, leading to the preference for the 290 nm

wavelength. Unlike UV and dRI, FLD is unaffected by pressure and flow changes and can provide a reliable source. Therefore, excitation at 280 and 290 nm was explored to obtain a reliable signal for recovery studies.

The UV absorption spectrum of Liraglutide in formulation buffer and the emission spectra upon excitation at 280 and 290 nm are shown in Figure 5.1. Absorption below 280 nm (Figure 5.1a) is completely masked by interferences, whereas the signal at 290 nm (red trace, Figure 5.1b), compared to absorption at 280 nm (blue trace), is intense and shows low baseline noise. Based on this information, emission upon excitation at these two wavelengths was scanned, resulting in the corresponding emission spectra (Figures 5.1d, 1e). The baseline noise was acceptable at 400 nm emission (Figure 5.1d, dashed line) and after 340 nm (Figure 5.1e, dashed line), where the noise/signal ratio was lowest in both cases. The corresponding emission profiles are shown in Figure 5.1c. Interestingly, though absorption at 280 nm was not effective, its emission exhibited the lowest LoD and LoQ, which were found to be 2.1 nmol and 7 nmol, respectively.

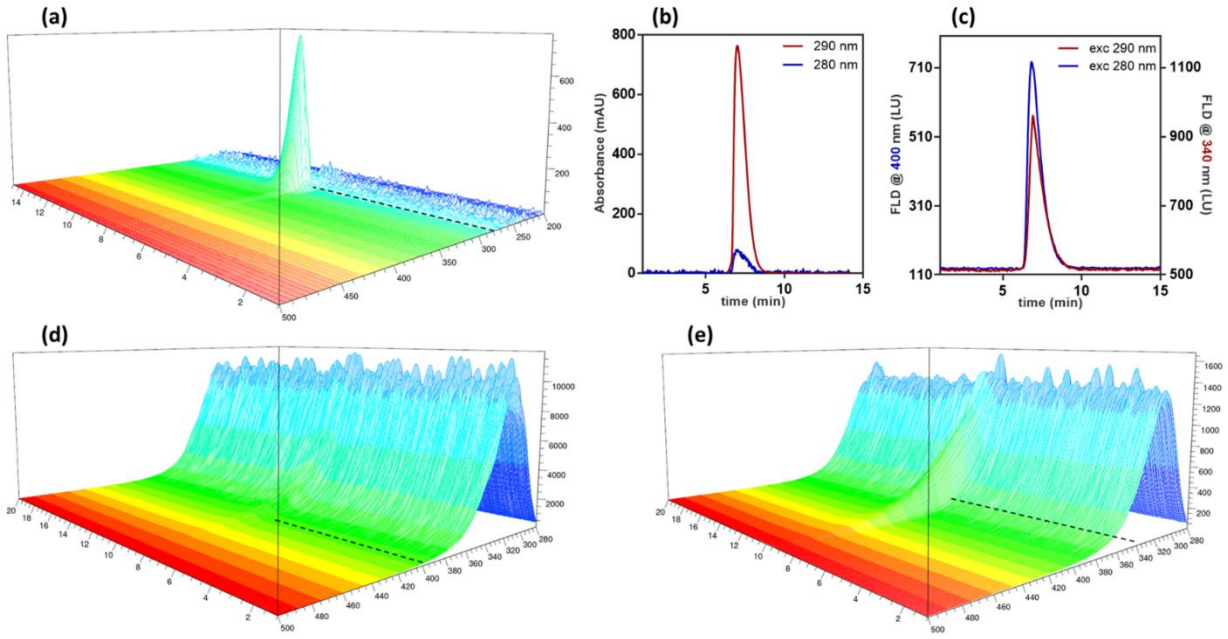

Figure 5.1. (**a**) Absorption spectrum of Liraglutide in formulation buffer analysed in FFIA. Dashed line: absorption at 280 nm. (**b**) Overlay of UV absorption at 280 (blue) and 290 (red) nm. (**c**) Comparison between FLD signals at optimal wavelength upon excitation at 280 nm (blue) or 290 nm (red). (**d,e**) Emission spectrum of Liraglutide upon excitation at 280 nm (**d**) and 290 nm (**d,e**). Dashed line: emission signal at 340 nm.

The next steps in method development involved selecting the channel membrane and calculating recovery. A PES membrane with a molecular weight cutoff (MWCO) of 1 kDa was chosen, as other materials and variants could not guarantee a cutoff below the peptide molecular weight. Recovery, calculated in triplicate, was evaluated both for BSA as a standard protein and for all Liraglutide samples (API, FDF, RLD, and aggregated API; see Table 1). BSA exhibited quantitative recovery (>99.9%), while Liraglutide recovery, though optimal, ranged between 98 and 100%. As shown in Figure 5.2, higher recovery was observed for the API samples (aggregated or untreated), while slightly lower values were found for FDF and commercial products (between 98 and 99%), likely due to the different aging times between the API samples (freshly suspended in the formulation media at the time of the experiment) and the FDF and RLD samples (suspended in the formulation buffer at the beginning of their shelf life).

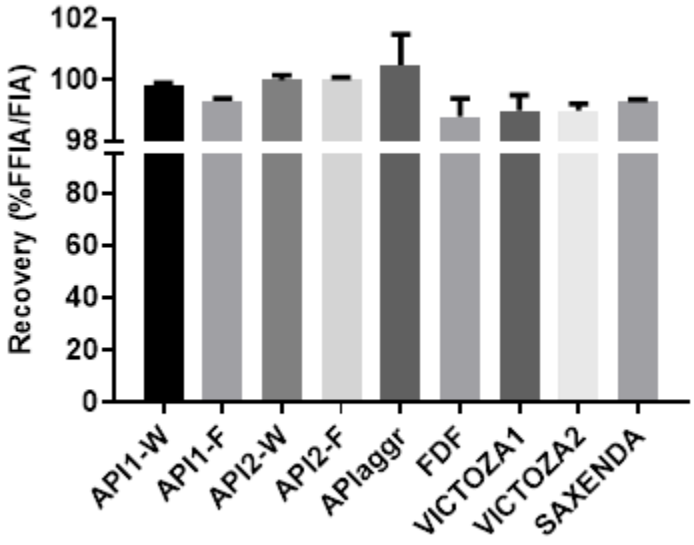

Figure 5.2. Recovery calculated for all Liraglutide FDF, expressed as area % between a FFIA and a FIA.

A focus flowrate of 1.50 mL/min (inject flow: 0.2 mL/min) and a longitudinal flowrate of 0.50 mL/min were selected. Different focus flowrates and focusing times did not affect recovery but worsened baseline drift. The crossflow velocity was scanned in the 1.0–2.5 mL/min range using API1-W as a test sample. Only the highest applied crossflow rate resulted in a good separation from the void peak, while higher flowrates could not be employed due to the pressure limits of the

system. To reduce analysis time and allow highly aggregated species to elute before the field release, the method was further modified to a gradient decreasing crossflow rate to zero over 20 minutes. Six minutes into the run, when the flow control switched from focus to elution, a system peak appeared in all analyses (blank included), due to the change in system pressure. Application of the crossflow also caused the aforementioned baseline drifts in both the dRI and UV detectors, while FLD remained unaffected in all cases. The applicability of the developed setup was confirmed by BSA injections, with its mass accurately calculated using dRI as the concentration source (Figure 5.3).

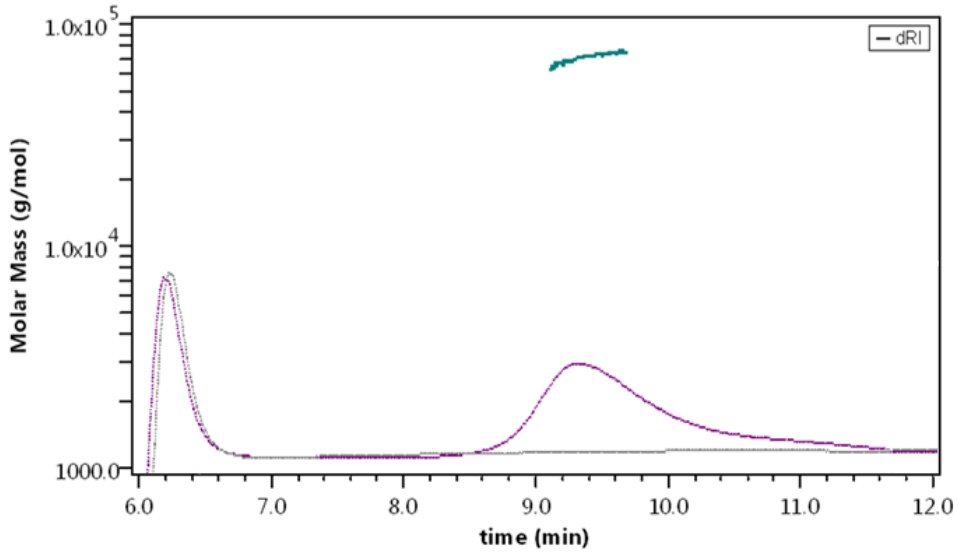

Figure 5.3. dRI signal overlay of a blank (grey) and BSA (pink) injection with the optimized method. Green distribution: molar mass calculation of BSA monomer.

The developed method met the standards required for a validated method according to the harmonized guidelines ICHQ2R1 and ISO/TS 21362 [330, 331] and was, therefore, considered a standardized method, used to characterize all samples.

Characterization of API and Aggregated API

The API samples were characterized using the AF4-MD method, both after resuspension in water and in formulation at a concentration of 6 mg/mL. In both cases, Liraglutide eluted with a single

peak at 7.8 min, with API1 and API2 overlapping and showing identical profiles and molar mass distributions (Figure 5.4a).

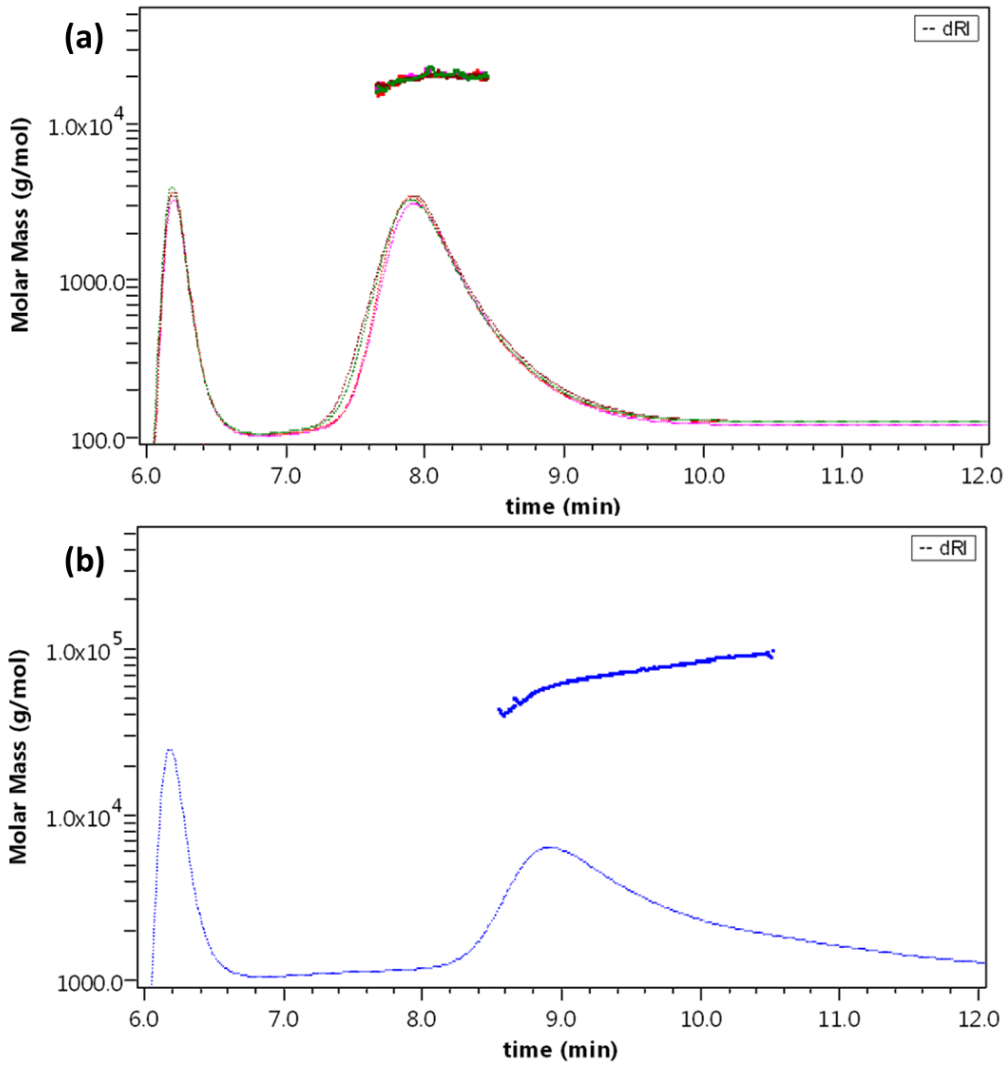

Figure 5.4. (a) dRI fractogram and molar mass overlay of API1-W (red), API1-F (purple), API2-W (green), and API2-F (violet), representative runs. (b) dRI fractogram and molar mass overlay of APIaggr, representative run.

The molar mass obtained from light scattering ranged between 19 and 20 kDa for all samples (API1-W: 19.6 ± 0.4; API1-F: 19.8 ± 0.2; API2-W: 19.2 ± 0.8; and API2-F: 19.7 ± 0.5 kDa). No evidence of monomer was observed, as confirmed by the FLD signal profile. The v-value calculated from a conformation plot (see Section 1.3.4) averaged 0.78, indicating a non-spherical, non-compact conformation [332].

The ability of the method to distinguish different forms of Liraglutide was further tested by analyzing a sample of thermally stressed, aggregated API. In this case, no species were observed before 9 min elution time, where a band was eluted with a broad molar mass distribution averaging 73.7 kDa, corresponding to aggregates of over 20 units (Figure 5.4b). The v-value was negative, suggesting that mass increase corresponded to a size decrease [296], indicating that the structure was extremely compact, possibly due to irreversible denaturation and covalent aggregation. Additionally, a second population was detected by FLD (9 ± 1% of FLD area) at 26 min, corresponding to the field release (e.g., zero crossflow), with an estimated molar mass of up to 10^8 Da (not shown).

Characterization of FDF and RLD Samples

The FDF and RLD (Victoza, Saxenda) samples were also subjected to the same method. The FDF sample appeared as a single band, with the same retention time (7.8 min) and molar mass distribution (19.9 ± 0.4 kDa) as the previous samples. Similarly, the Victoza lots and the Saxenda lot analyzed contained a single population corresponding to Liraglutide oligomers (Victoza1: 19.2 ± 0.7 kDa; Victoza2: 20.1 ± 0.4 kDa; Saxenda: 19.9 ± 0.3 kDa). All samples are overlaid in Figure 5.5.

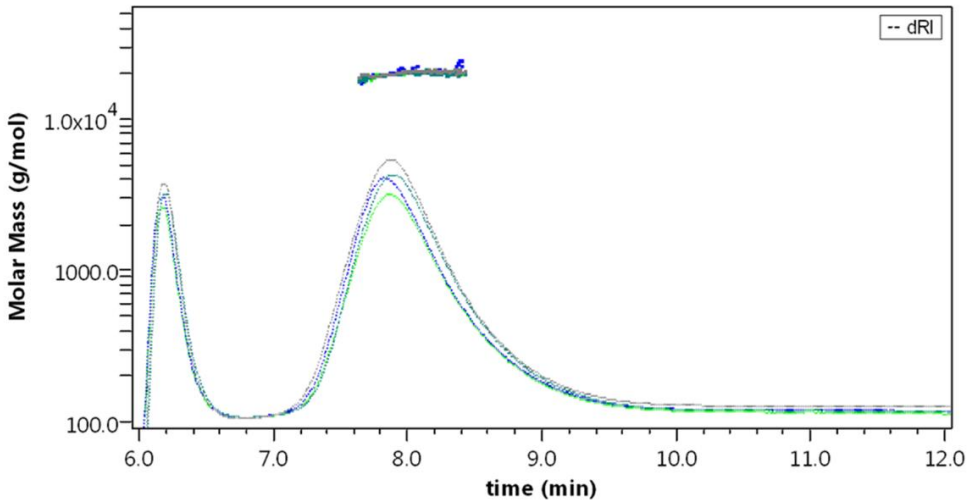

Figure 5.5. dRI fractogram and molar mass overlay of FDF (blue), Victoza1 (green), Victoza2 (teal), and Saxenda (blue), representative runs.

As with previous samples, the calculated v-values corresponded to 0.7, indicating a branched/extended conformation. No trace of monomer or higher molecular weight oligomers was detected.

Mass Comparison and Sameness Evaluation

All samples are grouped together and shown in Figure 5.6 as histograms representing their molar mass. Statistical evaluation (performed using one-way ANOVA) confirmed that there was no significant difference between all samples, except for the aggregated API ($p < 0.0001$ against all other samples), confirming the identity between commercial and R&D products.

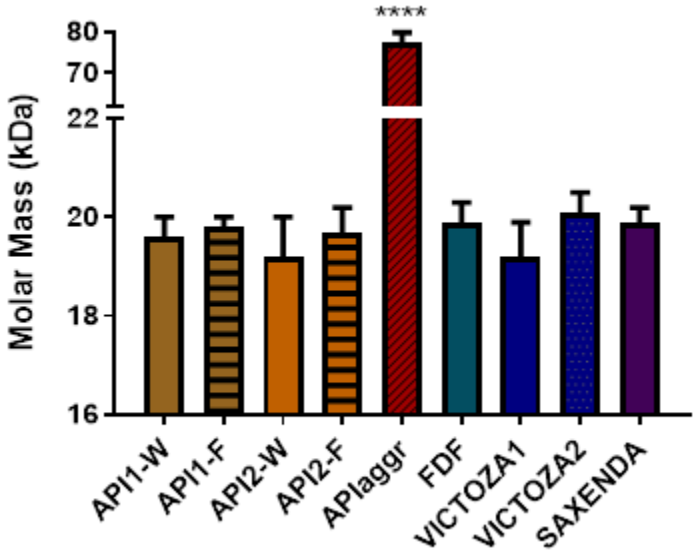

Figure 5.6. Molar mass distributions calculated for all samples. ****: $p < 0.0001$.

Interestingly, sameness was also assessed for freshly dissolved APIs (API1-W and API2-W), suggesting that the aggregation of Liraglutide in formulation is a fast process, yielding a single aggregate type that stabilizes the structure and prevents further aggregation. This was further verified by reducing the focusing time and confirming that no difference in molar mass distribution was detected.

The associated form found for Liraglutide in formulation is numerically equal to 5.2 units, indicating the primary presence of a pentamer. Upon heating (APIaggr), the thermal stress imposed on the sample generated stable aggregates, likely through unfolding, leading to very compact denatured aggregates averaging 20 units.

SEC Analyses

The aggregation state of Liraglutide, along with the sameness evaluation of the finished product and commercial products, was also analyzed through SEC-MALS as a benchmark technique. In this case, due to limitations in the mobile phase composition caused by the need of compatibility with the stationary phase of the column, the analyses were performed in a aqueous mobile phase containing 30% acetonitrile.

The results showed a main peak at 19 min for all samples tested, followed by two minor peaks at 16 and 17 min, respectively. At 23 min, the peak corresponding to phenol (contained in the formulation medium) was eluted (Figure 5.7a).

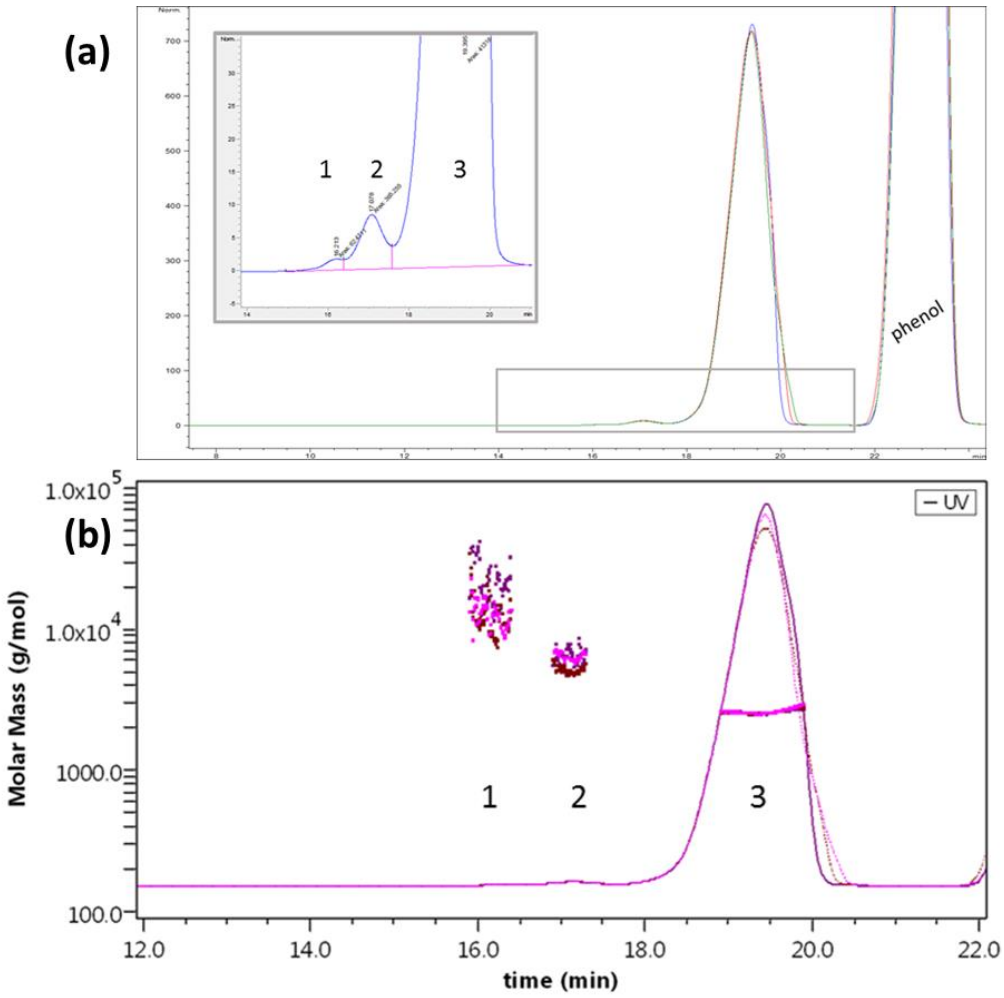

Figure 5.7. SEC analysis of Liraglutide. (**a**) Separation profile. Inset: zoom on the higher MW population (dimer, tetramer). (**b**) Molar mass calculation obtained from MALS overlay of three replicates of a representative sample.

Mass calculation (Figure 5.7b) showed a slight underestimation of the monomer weight, an effect (MW deviation) observed with the use of a mixed solvent due to preferential solvation [333]. The species detected corresponded to monomer, dimer, and tetramer (n = 3), with both preparations showing the same peaks, retention times, and molar mass distributions. In terms of relative abundance, the monomer percentage was above 99.5% for both preparations (Figure 5.8a,b), though some differences were detected between samples. Samples nearing their expiration dates showed lower monomer percentages, suggesting that aging is associated with irreversible aggregation.

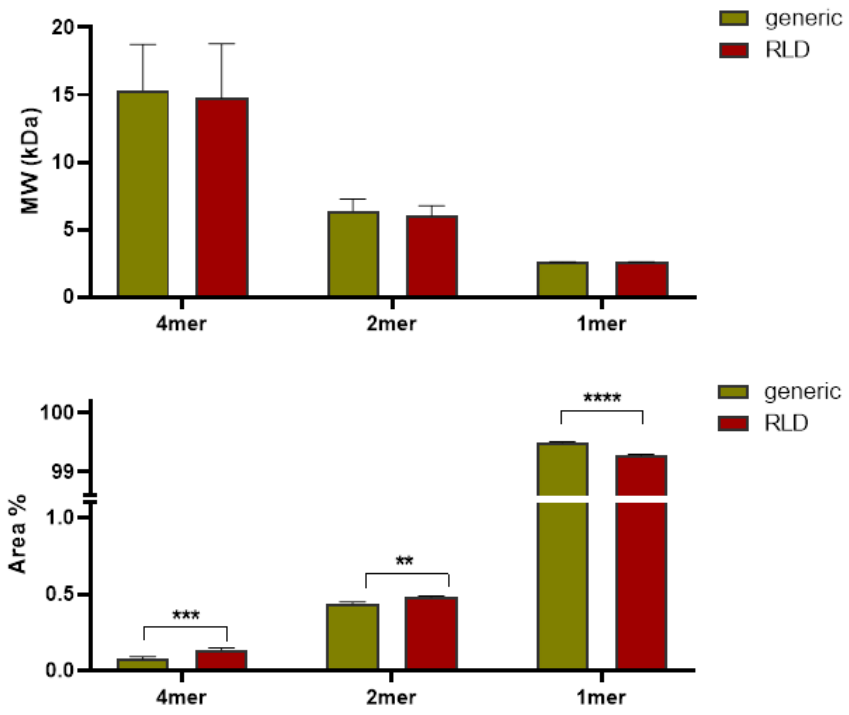

Figure 5.8. Comparison between different Liraglutide samples. (**a**) Measured molar mass; (**b**) relative abundance of aggregated species. ****: $p < 0.0001$. ***: $p < 0.001$. **: $p < 0.01$ (two-way ANOVA).

Interestingly, SEC analyses reversed the aggregation state found in FFF analyses, highlighting the predominant presence of the monomer and confirming the non-covalent nature of the pentamer. The size of the aggregates provided information on the aggregation pattern (e.g., dimer-dimer or dimer-monomer combinations) or indicated sample degradation, which may follow the same process but in an irreversible manner.

The combination of novel FFF data in formulation with SEC analyses is crucial to meet FDA requirements for peptide drug commercialization. Abbreviated New Drug Application (ANDA) applicants are encouraged to apply orthogonal analytical methods to characterize properties such as secondary structure, oligomerization, and aggregation, and to "demonstrate that the proposed synthetic peptide active ingredient is the ‘same as’ the active ingredient in the RLD" [318]. As these properties may be affected by the formulation, they should be evaluated in an environment as close as possible to the real one.

The use of AF4 and SEC represents a suitable approach for such studies. AF4 depicts the real aggregation state in native conditions, while SEC removes labile aggregates. Together, they show that Liraglutide is not polymerized, but aggregated into stable, non-covalent oligomers (pentamers), which are removed in SEC conditions. Furthermore, the reversed elution order between the two techniques favors the use of FFF for high molecular weight species. For example, the 10^8 Da species found in the aggregated API sample would go undetected in SEC analyses, omitting critical information for understanding the aggregation properties of Liraglutide, thus posing a potential health risk. At the same time, FFF is necessary for detecting low molecular weight species and accurately representing the native state, where the monomer is absent. Additionally, FFF analyses can be performed in formulation buffers to meet the latest FDA requirements for comparative studies on peptide aggregation and molecular conformation (sameness studies). Thus, SEC and FFF together provide a complete picture of the native aggregation state (FFF) and aggregate type (SEC) of Liraglutide.

5.4 Conclusions

Proper measurement of the native aggregation state of peptide APIs is critical for ensuring their safety and pharmacological profile. Regulatory agencies worldwide emphasize the importance of this by requiring pharma companies to fully characterize their peptide APIs and demonstrate sameness with the RLD when the API is a generic. Achievement of accurate characterization necessitates working within the formulation to adequately represent the sample state.

In this study, we focused on the characterization of Liraglutide, a Glucagon-like peptide 1 (GLP1) agonist, using an AF4 analytical platform. The developed method successfully identified the aggregation state of Liraglutide and exhibited excellent limits of quantification (LoQ) and recovery rates, despite challenges associated with using a highly absorbing, high-viscosity eluent. Additionally, the analysis of a purposely degraded sample demonstrated the capability of the method to differentiate Liraglutide aggregates in terms of both retention time and conformation.

Our results indicated that the native association state of Liraglutide is pentameric. Moreover, the method was used to conduct a sameness study, confirming the identity between commercial RLD samples, finished dosed forms, and APIs. This technology enhances the toolkit for characterizing

the aggregation properties not only of peptide APIs but also of protein drugs. Key advantages are the softness and nativeness of the separation which allow a characterization of the sample in its native state and at the same time preserving existing weak quaternary structures.

Chapter 6. General conclusions

The whole work here presented has dealt with the role of AF4/HF5-MD platforms in the field of nanomedicine; this role is discussed trough a review of the state of the art (Chapter 1) and four thematic chapters presenting the results of novel studies on NMs, of different nature and complexity, in which AF4 played different roles during their development, as sketched in Figure 6.1.

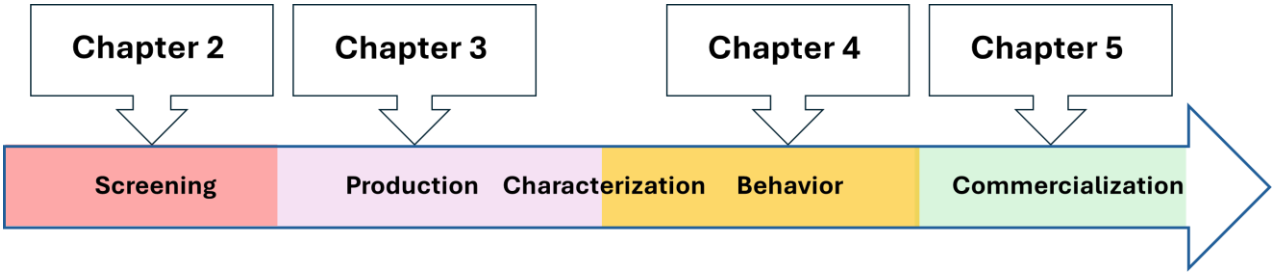

Figure 6.1. Schematization of how the various chapter/studies position themselves in the context of NMs development.

In Chapter 2 HF5-MD has been exploited to unveil for the first time the contemporaneous presence and behaviour of different PDA nanoforms. These results may act at the base for the identification of the optimal PDA nanoforms for the intended purposes.

In Chapter 3 HF5-MD acted as a comprehensive platform for synthesis monitoring, characterization and purification of Ag-PDA NPs.

In Chapter 4 HF5-MD was used to characterize the behaviour of PP-MNPs during a simulated injection in the blood stream.

In Chapter 5, according to FDA guidelines, AF4-MD was used to evaluate the native aggregation state of Liraglutide and perform a *sameness study* regarding different Liraglutide based products.

Altogether, a common thread emerges: the ubiquity of the technique in terms of analyzed species (from small peptides to ENPs), analytical conditions and evaluated CQAs (Table 6.1).

	Evaluated in this work by AF4/HF5-MD?	HOW?	Could be Evaluated by AF4/HF5-MD?	HOW?
Chemical composition, structure, impurities	NO	/	YES	Online coupling with MS detector [334]
Particle size distribution and concentration	YES (Chapter 2-5)	AF4/HF5-MALS - concentration detector	/	/
Surface properties (e.g. z-potential, hydrophobicity, surface area, surface coating)	NO	/	YES (z-potential only)	Use of a EAF4 module [303].
Drug loading	NO	/	YES	Online coupling with MS detector [193] or by exploiting a standard MALS + concentration detector setup [97].
Drug release (In vitro/in vivo/in physiologically-clinically relevant media)	NO	/	YES (AF4-MD can act as a standalone technique for API separation and quantification)	Standard MALS + concentration detector setup [106].
Chemical and physical stability, degradation paths and relative kinetics	YES (Chapter 4)	HF5-DAD-MALS (Further information could be obtained by MS coupling)	/	/

Table 6.1. Summary of the roles played by AF4/HF5-MD in this work as well as of the other potential applications for the evaluation on the main physicochemical CQAs for market approval.

These features are unique of this set up. Many of the common alternatives are batch techniques which provide only average results and whose limitations were made apparent in the study. SEM and TEM are slow and expensive, and they could not clearly assess the presence of the polymeric PDA-Ps species (Chapter 2) as well the PEG/PLGA coating of PP-MNPs (Chapter 4). DLS fell on the same limitations as it is not able to adequately observe the presence of PDA-Ps (Chapter 2) and precisely visualize the evolution of PP-MNPs in the simulated media (Chapter 4).

The separation ability of the AF4 platform has major implication besides the ability to identify and resolve the presence of different populations. By monitoring over time the evolution of species formed during a reaction, the technique opens the doors to reaction time optimization (Chapter 2 and 3) as well tuning the reaction conditions to obtain a preferential product (e.g. PDA-NPs instead of PDA-Ps; Chapter 2). Moreover, the soft separation allows for a non-destructive isolation of the species of interest, a feature of outmost importance as for the production pipeline as well as in terms of NMs activity (Chapter 3). Other advantages provided by the platform are represented by its potential automatability, high throughput and easy size scalability.

Currently the only technique on the market which can be compared to AF4 is SEC. The latter, however, does not have the same degree of flexibility (Chapter 1) that, combined with a separation mechanism less gentle than in AF4, could affect representativeness of the results (Chapter 5).

Although AF4 is increasingly appearing in FDA and EMA guidelines as a complementary technique, because of a general lack of basic knowledge and a limited diffusion of the relevant instrumentation, it is still highly underexplored and does not play as yet a prominent role despite its outstanding potential. This work however clearly highlights the *passepartout* role of AF4 in terms of NMs development.

To uniform as much as possible the characterization requirements and to better compare the results of different studies on different samples, reference techniques are required. As highlighted in this study, given the complexity and heterogeneity of the challenges in nanomedicine, the highest degree of analytical flexibility is required to achieve the set goal. These needs make it difficult to identify reference techniques that can consistently provide reliable results without being affected by analytical biases or lack of representativeness. Currently, no techniques besides AF4 is potentially able to check almost all the needs for the physicochemical characterization of NMs. Therefore, AF4 should be globally employed in all the stages of NMs development, and its results should act as a reference *common language* during the various stages of NMs development and market approval.

Appendix A - List of the main abbreviations

Abbreviation	Full Name
AF4	Asymmetrical Flow Field-Flow Fractionation
APCs	Antigen-presenting cell(s)
APIs	Active Pharmaceutical Ingredient(s)
CQAs	Critical Quality Attribute(s)
DAD	Diode Array Detector
DLS	Dynamic Light Scattering
DPPH	2,2-DiPhenyl-1-PicrylHydrazyl
EAF4	Electrical Asymmetrical Flow Field Flow Fractionation
ELS	Electrophoretic Light Scattering
EMA	European Medicines Agency
ENPs	Engineered Nanoparticle(s)
EPR	Enhanced Permeation and Retention
FDA	Food and Drug Administration
FDF	Finished Dosage Form
FLD	Fluorescence Detector
FlFFF	Flow Field-Flow Fractionation
FT-IR	Fourier Transform Infrared (Spectroscopy)
GMP	Good Manufacturing Practice
HF	Hollow-Fiber
HF5	Hollow-Fiber Flow Field-Flow Fractionation
HPLC	High-Performance Liquid Chromatography
HSA	Human Serum Albumin
ICH	International Conference on Harmonization of Technical Requirements for Registration of Pharmaceuticals for Human Use
LoD	Limit of Detection
LoQ	Limit of Quantification
LS	Light Scattering
MALS	Multi-Angle Light Scattering
MD	Multidetection
MNPs	Magnetic Nanoparticle(s)
NanoPSs	Nano Photosensitizer(s)
NML	Nanomedical
NMs	Nanomedicine(s)
NNPs	Natural occurring Nanoparticle(s)
NPs	Nanoparticle(s)
PDA	Polydopamine
PDI	Polydispersity Index
PEG	Polyethylene Glycol
PES	Polyether Sulfone
PLGA	Poly-Lactic-Glycolic Acid
PP-MNPs	PEG/PLGA MNPs
Ps	Polymer(s)
PSD	Particle Size
QC	Quality Control

R&D	Research and Development
RC	Regenerated Cellulose
Rg, r_g	Gyration Radius
Rh, r_h	Hydrodynamic Radius
RLD	Reference Listed Drug
RMS	Rate Mean Squared
ROS	Reactive Oxygen Species
SAXS	Small-Angle X-ray Scattering
SE	Scattering Element
SEC	Size Exclusion Chromatography
SEM	Scanning Electron Microscopy
TEM	Transmission Electron Microscopy

Appendix B - Bibliography

1. Bayda, S., et al., *The history of nanoscience and nanotechnology: from chemical–physical applications to nanomedicine.* Molecules, 2019. **25**(1): p. 112.
2. Liu, Q., et al., *Current research trends of nanomedicines.* Acta Pharmaceutica Sinica B, 2023. **13**(11): p. 4391-4416.
3. Mai, W.X. and H. Meng, *Mesoporous silica nanoparticles: a multifunctional nano therapeutic system.* Integrative Biology, 2013. **5**(1): p. 19-28.
4. Colombo, M., et al., *Biological applications of magnetic nanoparticles.* Chemical Society Reviews, 2012. **41**(11): p. 4306-4334.
5. Parak, W.J., T. Pellegrino, and C. Plank, *Labelling of cells with quantum dots.* Nanotechnology, 2005. **16**(2): p. R9.
6. Sperling, R.A., et al., *Biological applications of gold nanoparticles.* Chemical Society Reviews, 2008. **37**(9): p. 1896-1908.
7. Lin, C.-A.J., et al., *Synthesis, characterization, and bioconjugation of fluorescent gold nanoclusters toward biological labeling applications.* ACS nano, 2009. **3**(2): p. 395-401.
8. Rai, M., A. Yadav, and A. Gade, *Silver nanoparticles as a new generation of antimicrobials.* Biotechnology advances, 2009. **27**(1): p. 76-83.
9. Wilhelm, S., et al., *Water dispersible upconverting nanoparticles: effects of surface modification on their luminescence and colloidal stability.* Nanoscale, 2015. **7**(4): p. 1403-1410.
10. Torchilin, V.P., *Micellar nanocarriers: pharmaceutical perspectives.* Pharmaceutical research, 2007. **24**: p. 1-16.
11. Zhang, R., et al., *Sequential combination therapy of ovarian cancer with degradable N-(2-hydroxypropyl) methacrylamide copolymer paclitaxel and gemcitabine conjugates.* Proceedings of the National Academy of Sciences, 2014. **111**(33): p. 12181-12186.
12. Lee, Y., et al., *A protein nanocarrier from charge-conversion polymer in response to endosomal pH.* Journal of the American Chemical Society, 2007. **129**(17): p. 5362-5363.
13. Guo, P., *The emerging field of RNA nanotechnology.* Nature nanotechnology, 2010. **5**(12): p. 833-842.
14. Baker, S.N. and G.A. Baker, *Luminescent carbon nanodots: emergent nanolights.* Angewandte Chemie International Edition, 2010. **49**(38): p. 6726-6744.
15. Yu, S.-J., et al., *Bright fluorescent nanodiamonds: no photobleaching and low cytotoxicity.* Journal of the American Chemical Society, 2005. **127**(50): p. 17604-17605.
16. Baughman, R.H., A.A. Zakhidov, and W.A. De Heer, *Carbon nanotubes--the route toward applications.* science, 2002. **297**(5582): p. 787-792.
17. Nurunnabi, M., et al., *Photoluminescent graphene nanoparticles for cancer phototherapy and imaging.* ACS applied materials & interfaces, 2014. **6**(15): p. 12413-12421.
18. Zhang, X.-X., H.S. Eden, and X. Chen, *Peptides in cancer nanomedicine: drug carriers, targeting ligands and protease substrates.* Journal of controlled release, 2012. **159**(1): p. 2-13.
19. Zhang, Q., et al., *Mechanical properties and biomineralization of multifunctional nanodiamond-PLLA composites for bone tissue engineering.* Biomaterials, 2012. **33**(20): p. 5067-5075.

20. Altınogˇlu, E.I., et al., *Near-infrared emitting fluorophore-doped calcium phosphate nanoparticles for in vivo imaging of human breast cancer.* ACS nano, 2008. **2**(10): p. 2075-2084.
21. Matsumura, Y. and H. Maeda, *A new concept for macromolecular therapeutics in cancer chemotherapy: mechanism of tumoritropic accumulation of proteins and the antitumor agent smancs.* Cancer research, 1986. **46**(12_Part_1): p. 6387-6392.
22. Chow, E.K.-H. and D. Ho, *Cancer nanomedicine: from drug delivery to imaging.* Science translational medicine, 2013. **5**(216): p. 216rv4-216rv4.
23. Peteiro-Cartelle, J., et al., *One example on how colloidal nano-and microparticles could contribute to medicine.* Nanomedicine, 2009. **4**(8): p. 967-979.
24. Pelaz, B., et al., *Diverse applications of nanomedicine.* ACS nano, 2017. **11**(3): p. 2313-2381.
25. Fang, J., W. Islam, and H. Maeda, *Exploiting the dynamics of the EPR effect and strategies to improve the therapeutic effects of nanomedicines by using EPR effect enhancers.* Advanced drug delivery reviews, 2020. **157**: p. 142-160.
26. Islam, R., H. Maeda, and J. Fang, *Factors affecting the dynamics and heterogeneity of the EPR effect: Pathophysiological and pathoanatomic features, drug formulations and physicochemical factors.* Expert opinion on drug delivery, 2022. **19**(2): p. 199-212.
27. Thangudu, S., F.-Y. Cheng, and C.-H. Su, *Advancements in the blood–brain barrier penetrating nanoplatforms for brain related disease diagnostics and therapeutic applications.* Polymers, 2020. **12**(12): p. 3055.
28. Giordani, S., et al., *Liposomes characterization for market approval as pharmaceutical products: Analytical methods, guidelines and standardized protocols.* Journal of Pharmaceutical and Biomedical Analysis, 2023: p. 115751.
29. Nimesh, S., *Gene therapy: Potential applications of nanotechnology*. 2013: Elsevier.
30. Massing, U. and S. Fuxius, *Liposomal formulations of anticancer drugs: selectivity and effectiveness.* Drug resistance updates, 2000. **3**(3): p. 171-177.
31. Gao, D., et al., *Multifunctional phototheranostic nanomedicine for cancer imaging and treatment.* Materials Today Bio, 2020. **5**: p. 100035.
32. Tan, Y.F., et al., *Controlled-release nanotherapeutics: State of translation.* Journal of controlled release, 2018. **284**: p. 39-48.
33. Rehan, F., et al., *Therapeutic applications of nanomedicine: recent developments and future perspectives.* Molecules, 2024. **29**(9): p. 2073.
34. Wong, C.H., et al., *The estimated annual financial impact of gene therapy in the United States.* Gene Therapy, 2023. **30**(10): p. 761-773.
35. Xue, C., et al., *Programmably tiling rigidified DNA brick on gold nanoparticle as multi-functional shell for cancer-targeted delivery of siRNAs.* Nature Communications, 2021. **12**(1): p. 2928.
36. Rohiwal, S., et al., *Iron Oxide Nanoparticle-Mediated siRNA Delivery System for Huntington's Disease Treatment.* ACS Applied Nano Materials, 2023. **6**(7): p. 5106-5116.
37. Khademi, Z., et al., *A novel dual-targeting delivery system for specific delivery of CRISPR/Cas9 using hyaluronic acid, chitosan and AS1411*. Carbohydrate polymers, 2022. **292**: p. 119691.
38. Casadidio, C., et al., *Effect of Polyplex Size on Penetration into Tumor Spheroids.* Molecular Pharmaceutics, 2023. **20**(11): p. 5515-5531.

39. Duan, L., et al., *Nanoparticle delivery of CRISPR/Cas9 for genome editing.* Frontiers in Genetics, 2021. **12**: p. 673286.
40. Jürgens, D.C., et al., *Lab-scale siRNA and mRNA LNP manufacturing by various microfluidic mixing techniques–an evaluation of particle properties and efficiency.* OpenNano, 2023. **12**: p. 100161.
41. Zhu, Y., et al., *Multi-step screening of DNA/lipid nanoparticles and co-delivery with siRNA to enhance and prolong gene expression.* Nature communications, 2022. **13**(1): p. 4282.
42. Fan, Y., et al., *Cationic liposome–hyaluronic acid hybrid nanoparticles for intranasal vaccination with subunit antigens.* Journal of Controlled Release, 2015. **208**: p. 121-129.
43. Namiot, E.D., et al., *Nanoparticles in clinical trials: analysis of clinical trials, FDA approvals and use for COVID-19 vaccines.* International journal of molecular sciences, 2023. **24**(1): p. 787.
44. Schwendener, R.A., *Liposomes as vaccine delivery systems: a review of the recent advances.* Therapeutic advances in vaccines, 2014. **2**(6): p. 159-182.
45. Wang, N., M. Chen, and T. Wang, *Liposomes used as a vaccine adjuvant-delivery system: From basics to clinical immunization.* Journal of Controlled Release, 2019. **303**: p. 130-150.
46. Milane, L. and M. Amiji, *Clinical approval of nanotechnology-based SARS-CoV-2 mRNA vaccines: impact on translational nanomedicine.* Drug delivery and translational research, 2021. **11**: p. 1309-1315.
47. Lakshmanan, V.-K., et al., *Nanomedicine-based cancer immunotherapy: recent trends and future perspectives.* Cancer Gene Therapy, 2021. **28**(9): p. 911-923.
48. Debele, T.A., C.-F. Yeh, and W.-P. Su, *Cancer immunotherapy and application of nanoparticles in cancers immunotherapy as the delivery of immunotherapeutic agents and as the immunomodulators.* Cancers, 2020. **12**(12): p. 3773.
49. Shan, X., et al., *Current approaches of nanomedicines in the market and various stage of clinical translation.* Acta Pharmaceutica Sinica B, 2022. **12**(7): p. 3028-3048.
50. Amaravadi, R.K., A.C. Kimmelman, and J. Debnath, *Targeting autophagy in cancer: recent advances and future directions.* Cancer discovery, 2019. **9**(9): p. 1167-1181.
51. Zhang, J., et al., *An updated overview on the development of new photosensitizers for anticancer photodynamic therapy.* Acta pharmaceutica sinica B, 2018. **8**(2): p. 137-146.
52. Alsaab, H.O., et al., *Progress in clinical trials of photodynamic therapy for solid tumors and the role of nanomedicine.* Cancers, 2020. **12**(10): p. 2793.
53. Lin, L., et al., *Nano-photosensitizers for enhanced photodynamic therapy.* Photodiagnosis and Photodynamic Therapy, 2021. **36**: p. 102597.
54. Xiang, Y., et al., *Near-infrared mediated orthogonal bioimaging and intracellular tracking of upconversion nanophotosensitizers.* Microchimica Acta, 2022. **189**(3): p. 120.
55. Galdiero, S., et al., *Silver nanoparticles as potential antiviral agents.* Molecules, 2011. **16**(10): p. 8894-8918.
56. Tanwar, J., et al., *Multidrug resistance: an emerging crisis.* Interdisciplinary perspectives on infectious diseases, 2014. **2014**(1): p. 541340.
57. Sharma, R.K. and R. Ghose, *Synthesis of zinc oxide nanoparticles by homogeneous precipitation method and its application in antifungal activity against Candida albicans.* Ceramics International, 2015. **41**(1): p. 967-975.

58. McCoy, M.E., et al., *Mechanisms of protective immune responses induced by the Plasmodium falciparum circumsporozoite protein-based, self-assembling protein nanoparticle vaccine.* Malaria journal, 2013. **12**: p. 1-12.
59. Ngoy, J.M., et al., *Covalent functionalization for multi-walled carbon nanotube (f-MWCNT)-folic acid bound bioconjugate.* J Appl Sci, 2011. **11**(15): p. 2700-11.
60. Gilbertson, L.M., et al., *Toward safer multi-walled carbon nanotube design: Establishing a statistical model that relates surface charge and embryonic zebrafish mortality.* Nanotoxicology, 2016. **10**(1): p. 10-19.
61. Parise, A., H. Thakor, and X. Zhang, *Activity inhibition on municipal activated sludge by single-walled carbon nanotubes.* Journal of nanoparticle research, 2014. **16**: p. 1-9.
62. Yah, C.S. and G.S. Simate, *Nanoparticles as potential new generation broad spectrum antimicrobial agents.* DARU Journal of Pharmaceutical Sciences, 2015. **23**: p. 1-14.
63. Ponkshe, P., S. Feng, and C. Tan, *Inhalable liposomes for treating lung diseases: Clinical development and challenges.* Biomedical Materials, 2021. **16**(5): p. 054101.
64. Park, K., *The beginning of the end of the nanomedicine hype.* Journal of controlled release: official journal of the Controlled Release Society, 2019. **305**: p. 221-222.
65. Anselmo, A.C. and S. Mitragotri, *Nanoparticles in the clinic: An update.* Bioengineering & translational medicine, 2019. **4**(3): p. e10143.
66. Marques, M.R., et al., *Nanomedicines-tiny particles and big challenges.* Advanced Drug Delivery Reviews, 2019. **151**: p. 23-43.
67. Weissig, V., T.K. Pettinger, and N. Murdock, *Nanopharmaceuticals (part 1): products on the market.* International journal of nanomedicine, 2014: p. 4357-4373.
68. He, H., et al., *Survey of clinical translation of cancer nanomedicines—lessons learned from successes and failures.* Accounts of chemical research, 2019. **52**(9): p. 2445-2461.
69. Wong, C.H., K.W. Siah, and A.W. Lo, *Estimation of clinical trial success rates and related parameters.* Biostatistics, 2019. **20**(2): p. 273-286.
70. Germain, M., et al., *Delivering the power of nanomedicine to patients today.* Journal of Controlled Release, 2020. **326**: p. 164-171.
71. Martins, J.P., et al., *The solid progress of nanomedicine.* Drug delivery and translational research, 2020. **10**: p. 726-729.
72. Wang, Y. and D.W. Grainger, *Regulatory considerations specific to liposome drug development as complex drug products.* Frontiers in Drug Delivery, 2022. **2**: p. 901281.
73. Borman, P. and D. Elder, *Q2 (R1) validation of analytical procedures: text and methodology.* ICH quality guidelines: an implementation guide, 2017: p. 127-166.
74. Balsgart, N.M., et al., *High throughput identification and quantification of phospholipids in complex mixtures.* Analytical chemistry, 2016. **88**(4): p. 2170-2176.
75. Navas-Moreno, M. and J.W. Chan, *Laser tweezers Raman microspectroscopy of single cells and biological particles.* Cellular Heterogeneity: Methods and Protocols, 2018: p. 219-257.
76. Fan, Y., M. Marioli, and K. Zhang, *Analytical characterization of liposomes and other lipid nanoparticles for drug delivery.* Journal of pharmaceutical and biomedical analysis, 2021. **192**: p. 113642.
77. McPhee, C., et al., *Measuring the lamellarity of giant lipid vesicles with differential interference contrast microscopy.* Biophysical journal, 2013. **105**(6): p. 1414-1420.

78. Brandl, M., et al., *Three-dimensional liposome networks: freeze fracture electron microscopical evaluation of their structure and in vitro analysis of release of hydrophilic markers.* Advanced drug delivery reviews, 1997. **24**(2-3): p. 161-164.
79. Crawford, R., et al., *Analysis of lipid nanoparticles by Cryo-EM for characterizing siRNA delivery vehicles.* International journal of pharmaceutics, 2011. **403**(1-2): p. 237-244.
80. Robson, A.-L., et al., *Advantages and limitations of current imaging techniques for characterizing liposome morphology.* Frontiers in pharmacology, 2018. **9**: p. 80.
81. Faustino, C. and L. Pinheiro, *Lipid systems for the delivery of amphotericin B in antifungal therapy.* Pharmaceutics, 2020. **12**(1): p. 29.
82. Stetefeld, J., S.A. McKenna, and T.R. Patel, *Dynamic light scattering: a practical guide and applications in biomedical sciences.* Biophysical reviews, 2016. **8**: p. 409-427.
83. Willmott, G.R., *Tunable resistive pulse sensing: better size and charge measurements for submicrometer colloids.* Analytical chemistry, 2018. **90**(5): p. 2987-2995.
84. Varenne, F., et al., *Multimodal dispersion of nanoparticles: a comprehensive evaluation of size distribution with 9 size measurement methods.* Pharmaceutical research, 2016. **33**: p. 1220-1234.
85. Grabielle-Madelmont, C., S. Lesieur, and M. Ollivon, *Characterization of loaded liposomes by size exclusion chromatography.* Journal of biochemical and biophysical methods, 2003. **56**(1-3): p. 189-217.
86. Lee, J.H., et al., *Cysteine-loaded pH-responsive liposome/gold nanoparticles as a time-temperature indicator with instantaneous color change.* Innovative Food Science & Emerging Technologies, 2021. **73**: p. 102794.
87. Contado, C., *Field flow fractionation techniques to explore the "nano-world".* Analytical and bioanalytical chemistry, 2017. **409**: p. 2501-2518.
88. Moon, J.J., et al., *Interbilayer-crosslinked multilamellar vesicles as synthetic vaccines for potent humoral and cellular immune responses.* Nature materials, 2011. **10**(3): p. 243-251.
89. Mayer, L., M. Hope, and P. Cullis, *Vesicles of variable sizes produced by a rapid extrusion procedure.* Biochimica et Biophysica Acta (BBA)-Biomembranes, 1986. **858**(1): p. 161-168.
90. Fröhlich, M., V. Brecht, and R. Peschka-Süss, *Parameters influencing the determination of liposome lamellarity by 31P-NMR.* Chemistry and physics of lipids, 2001. **109**(1): p. 103-112.
91. Engel, H., et al., *External surface area determination of lipid vesicles using trinitrobenzene sulfonate and ultraviolet/visible spectrophotometry.* Analytical biochemistry, 2013. **442**(2): p. 262-271.
92. Fan, Y., et al., *Immunogenic cell death amplified by co-localized adjuvant delivery for cancer immunotherapy.* Nano letters, 2017. **17**(12): p. 7387-7393.
93. Wang, J., et al., *Quality control and purification of ready-to-use conjugated gold nanoparticles to ensure effectiveness in biosensing.* Frontiers in Sensors, 2022. **3**: p. 1087115.
94. Franzen, U. and J. Østergaard, *Physico-chemical characterization of liposomes and drug substance–liposome interactions in pharmaceutics using capillary electrophoresis and electrokinetic chromatography.* Journal of chromatography A, 2012. **1267**: p. 32-44.
95. Van Haute, D., W. Jiang, and T. Mudalige, *Evaluation of size-based distribution of drug and excipient in amphotericin B liposomal formulation.* International Journal of Pharmaceutics, 2019. **569**: p. 118603.

96. Ansar, S.M. and T. Mudalige, *Characterization of doxorubicin liposomal formulations for size-based distribution of drug and excipients using asymmetric-flow field-flow fractionation (AF4) and liquid chromatography-mass spectrometry (LC-MS).* International journal of pharmaceutics, 2020. **574**: p. 118906.
97. Caputo, F., et al., *Asymmetric-flow field-flow fractionation for measuring particle size, drug loading and (in) stability of nanopharmaceuticals. The joint view of European Union Nanomedicine Characterization Laboratory and National Cancer Institute-Nanotechnology Characterization Laboratory.* Journal of Chromatography A, 2021. **1635**: p. 461767.
98. HALAMODA, K.B., et al., *Methodological needs in the quality and safety characterisation of nanotechnology-based health products: priorities for method development and standardisation.*
99. Shen, J. and D.J. Burgess, *In vitro dissolution testing strategies for nanoparticulate drug delivery systems: recent developments and challenges.* Drug delivery and translational research, 2013. **3**: p. 409-415.
100. D'Souza, S., *A review of in vitro drug release test methods for nano-sized dosage forms.* Advances in pharmaceutics, 2014. **2014**(1): p. 304757.
101. Yu, M., et al., *Predicting drug release kinetics from nanocarriers inside dialysis bags.* Journal of Controlled Release, 2019. **315**: p. 23-30.
102. Xu, X., M.A. Khan, and D.J. Burgess, *A two-stage reverse dialysis in vitro dissolution testing method for passive targeted liposomes.* International Journal of Pharmaceutics, 2012. **426**(1-2): p. 211-218.
103. Bhardwaj, U. and D.J. Burgess, *A novel USP apparatus 4 based release testing method for dispersed systems.* International journal of pharmaceutics, 2010. **388**(1-2): p. 287-294.
104. Solomon, D., et al., *Role of in vitro release methods in liposomal formulation development: challenges and regulatory perspective.* The AAPS journal, 2017. **19**: p. 1669-1681.
105. Nguyen, T.T., et al., *Determination of platinum drug release and liposome stability in human plasma by CE-ICP-MS.* International journal of pharmaceutics, 2013. **449**(1-2): p. 95-102.
106. Hinna, A.H., et al., *The use of asymmetrical flow field-flow fractionation with on-line detection in the study of drug retention within liposomal nanocarriers and drug transfer kinetics.* Journal of pharmaceutical and biomedical analysis, 2016. **124**: p. 157-163.
107. Skupin-Mrugalska, P., P.A. Elvang, and M. Brandl, *Application of asymmetrical flow field-flow fractionation for characterizing the size and drug release kinetics of theranostic lipid nanovesicles.* International Journal of Molecular Sciences, 2021. **22**(19): p. 10456.
108. Laverman, P., et al., *Microscopic localization of PEG-liposomes in a rat model of focal infection.* Journal of controlled release, 2001. **75**(3): p. 347-355.
109. de Oliveira Silva, J., et al., *Folate-coated, long-circulating and pH-sensitive liposomes enhance doxorubicin antitumor effect in a breast cancer animal model.* Biomedicine & pharmacotherapy, 2019. **118**: p. 109323.
110. Mehta, C.H., R. Narayan, and U.Y. Nayak, *Computational modeling for formulation design.* Drug Discovery Today, 2019. **24**(3): p. 781-788.
111. Balouch, M., et al., *In silico screening of drug candidates for thermoresponsive liposome formulations.* Molecular Systems Design & Engineering, 2021. **6**(5): p. 368-380.

112. Bordi, F. and C. Cametti, *Salt-induced aggregation in cationic liposome aqueous suspensions resulting in multi-step self-assembling complexes.* Colloids and surfaces B: Biointerfaces, 2002. **26**(4): p. 341-350.
113. Schimpf, M.E., K. Caldwell, and J.C. Giddings, *Field-flow fractionation handbook*. 2000: John Wiley & Sons.
114. Yang, J., et al., *Cell separation on microfabricated electrodes using dielectrophoretic/gravitational field-flow fractionation.* Analytical chemistry, 1999. **71**(5): p. 911-918.
115. Yohannes, G., et al., *Asymmetrical flow field-flow fractionation technique for separation and characterization of biopolymers and bioparticles.* Journal of chromatography A, 2011. **1218**(27): p. 4104-4116.
116. Reschiglian, P., et al., *Field-flow fractionation and biotechnology.* TRENDS in Biotechnology, 2005. **23**(9): p. 475-483.
117. Giordani, S., et al., *Field-flow fractionation in molecular biology and biotechnology.* Molecules, 2023. **28**(17): p. 6201.
118. Ko, M., et al., *Optimization for size separation of graphene oxide sheets by flow/hyperlayer field-flow fractionation.* Journal of Chromatography A, 2022. **1681**: p. 463475.
119. Williams, P.S. and J.C. Giddings, *Theory of field-programmed field-flow fractionation with corrections for steric effects.* Analytical chemistry, 1994. **66**(23): p. 4215-4228.
120. Martin, M. and R. Reynaud, *Polymer analysis by thermal field-flow fractionation.* Analytical Chemistry, 1980. **52**(14): p. 2293-2298.
121. Lou, J., M.N. Myers, and J. Calvin Giddings, *Separation of polysaccharides by thermal field-flow fractionation.* Journal of Liquid Chromatography & Related Technologies, 1994. **17**(14-15): p. 3239-3260.
122. Wahlund, K.-G., *Flow field-flow fractionation: critical overview.* Journal of Chromatography A, 2013. **1287**: p. 97-112.
123. Zattoni, A., et al., *Flow field-flow fractionation for the analysis of nanoparticles used in drug delivery.* Journal of pharmaceutical and biomedical analysis, 2014. **87**: p. 53-61.
124. Fuentes, C., et al., *Comparison between conventional and frit-inlet channels in separation of biopolymers by asymmetric flow field-flow fractionation.* Analyst, 2019. **144**(15): p. 4559-4568.
125. Shin, S.Y., et al., *Flow Field-Flow Fractionation with a Thickness-Tapered Channel.* Analytical Chemistry, 2022. **94**(41): p. 14460-14466.
126. Rambaldi, D.C., et al., *An analytical method for size and shape characterization of blood lipoproteins.* Clinical Chemistry, 2007. **53**(11): p. 2026-2029.
127. Lee, J.Y., S.K. Byeon, and M.H. Moon, *Profiling of oxidized phospholipids in lipoproteins from patients with coronary artery disease by hollow fiber flow field-flow fractionation and nanoflow liquid chromatography–tandem mass spectrometry.* Analytical chemistry, 2015. **87**(2): p. 1266-1273.
128. Tri, N., K. Caldwell, and R. Beckett, *Development of electrical field-flow fractionation.* Analytical chemistry, 2000. **72**(8): p. 1823-1829.
129. Zhang, X., et al., *Field-flow fractionation: A gentle separation and characterization technique in biomedicine.* TrAC Trends in Analytical Chemistry, 2018. **108**: p. 231-238.
130. Johann, C., et al., *Instrument and method to determine the electrophoretic mobility of nanoparticles and proteins by combining electrical and flow field-flow fractionation.* Analytical chemistry, 2015. **87**(8): p. 4292-4298.

131. Giddings, J.C., F.J. Yang, and M.N. Myers, *Sedimentation field-flow fractionation.* Analytical Chemistry, 1974. **46**(13): p. 1917-1924.
132. Reschiglian, P. and G. Torsi, *Determination of particle size distribution by gravitational field-flow fractionation: Dimensional characterization of silica particles.* Chromatographia, 1995. **40**: p. 467-473.
133. Contado, C., et al., *Continuous split-flow thin cell and gravitational field-flow fractionation of wheat starch particles.* Journal of Chromatography A, 2000. **871**(1-2): p. 449-460.
134. Williams, P.S., F. Carpino, and M. Zborowski, *Characterization of magnetic nanoparticles using programmed quadrupole magnetic field-flow fractionation.* Philosophical Transactions of the royal society A: Mathematical, physical and engineering sciences, 2010. **368**(1927): p. 4419-4437.
135. Williams, P.S., F. Carpino, and M. Zborowski, *Magnetic nanoparticle drug carriers and their study by quadrupole magnetic field-flow fractionation.* Molecular pharmaceutics, 2009. **6**(5): p. 1290-1306.
136. Waheed, W., et al., *Dielectrophoresis-field flow fractionation for separation of particles: A critical review.* Journal of Chromatography A, 2021. **1637**: p. 461799.
137. Semyonov, S. and K. Maslow, *Acoustic field-flow fractionation.* Journal of Chromatography A, 1988. **446**: p. 151-156.
138. Hwang, J.Y., S. Youn, and I.-H. Yang, *Gravitational field flow fractionation: Enhancing the resolution power by using an acoustic force field.* Analytica Chimica Acta, 2019. **1047**: p. 238-247.
139. Zappi, A., et al., *A green analytical method combined with chemometrics for traceability of tomato sauce based on colloidal and volatile fingerprinting.* Molecules, 2022. **27**(17): p. 5507.
140. Wahlund, K.G. and J.C. Giddings, *Properties of an asymmetrical flow field-flow fractionation channel having one permeable wall.* Analytical chemistry, 1987. **59**(9): p. 1332-1339.
141. Myers, M.N. and J.C. Giddings, *Properties of the transition from normal to steric field-flow fractionation.* Analytical Chemistry, 1982. **54**(13): p. 2284-2289.
142. Peterson, R.E., M.N. Myers, and J.C. Giddings, *Characterization of steric field-flow fractionation using particles to 100 μm diameter.* Separation Science and Technology, 1984. **19**(4-5): p. 307-319.
143. Ratanathanawongs, S.K. and J.C. Giddings, *Dual-field and flow-programmed lift hyperlayer field-flow fractionation.* Analytical chemistry, 1992. **64**(1): p. 6-15.
144. Marassi, V., et al., *Emerging Microfluidic Tools for Simultaneous Exosomes and Cargo Biosensing in Liquid Biopsy: New Integrated Miniaturized FFF-Assisted Approach for Colon Cancer Diagnosis.* Sensors, 2023. **23**(23): p. 9432.
145. Zattoni, A., et al., *Hollow-fiber flow field-flow fractionation.* Current Analytical Chemistry, 2007. **3**(4): p. 310-323.
146. Lee, W.J., B.-R. Min, and M.H. Moon, *Improvement in particle separation by hollow fiber flow field-flow fractionation and the potential use in obtaining particle size distribution.* Analytical Chemistry, 1999. **71**(16): p. 3446-3452.
147. Moon, M.H., K.H. Lee, and B.R. Min, *Effect of temperature on particle separation in hollow fiber flow field-flow fractionation.* Journal of Microcolumn Separations, 1999. **11**(9): p. 676-681.

148. Wang, J.-L., et al., *Theoretical and experimental investigation of the focusing position in asymmetrical flow field-flow fractionation (AF4).* Journal of Chromatography A, 2018. **1561**: p. 67-75.
149. You, Z., F. Meier, and S. Weidner, *Comparison of miniaturized and conventional asymmetrical flow field-flow fractionation (AF4) channels for nanoparticle separations.* Separations, 2017. **4**(1): p. 8.
150. Moon, M. and M. Myers, *Experimental field-flow fractionation: practices and precautions.* Field-Flow Fractionation Handbook, 2000: p. 199-211.
151. Oppenheimer, L.E. and G.A. Smith, *Sedimentation field-flow fractionation of colloidal metal hydrosols.* Journal of Chromatography A, 1989. **461**: p. 103-110.
152. Yang, F.-S., K.D. Caldwell, and J.C. Giddings, *Colloid characterization by sedimentation field-flow fractionation: II. Particle-size distribution.* Journal of Colloid and Interface Science, 1983. **92**(1): p. 81-91.
153. Zattoni, A., et al., *Turbidimetric detection method in flow-assisted separation of dispersed samples.* Analytical chemistry, 2003. **75**(23): p. 6469-6477.
154. Hupfeld, S., D. Ausbacher, and M. Brandl, *Asymmetric flow field-flow fractionation of liposomes: 2. Concentration detection and adsorptive loss phenomena.* Journal of separation science, 2009. **32**(20): p. 3555-3561.
155. Leeman, M., et al., *Proteins and antibodies in serum, plasma, and whole blood—size characterization using asymmetrical flow field-flow fractionation (AF4).* Analytical and bioanalytical chemistry, 2018. **410**: p. 4867-4873.
156. Wittgren, B. and K.-G. Wahlund, *Fast molecular mass and size characterization of polysaccharides using asymmetrical flow field-flow fractionation-multiangle light scattering.* Journal of Chromatography A, 1997. **760**(2): p. 205-218.
157. Wyatt, P.J., *Light scattering and the absolute characterization of macromolecules.* Analytica chimica acta, 1993. **272**(1): p. 1-40.
158. Zattoni, A., et al., *Tandem hollow-fiber flow field-flow fractionation.* Journal of Chromatography A, 2011. **1218**(27): p. 4132-4137.
159. Abd Mutalib, M., et al., *Scanning electron microscopy (SEM) and energy-dispersive X-ray (EDX) spectroscopy*, in *Membrane characterization*. 2017, Elsevier. p. 161-179.
160. De Graef, M., *Introduction to conventional transmission electron microscopy*. 2003: Cambridge university press.
161. Amini, R., et al., *Intertechnique comparisons for nanoparticle size measurements and shape distribution.* Journal of Hazardous, Toxic, and Radioactive Waste, 2016. **20**(1): p. B4015004.
162. Bhattacharjee, S., *DLS and zeta potential–what they are and what they are not?* Journal of controlled release, 2016. **235**: p. 337-351.
163. Connolly, J.R., *for EPS400-002.* Introduction to X-Ray Powder Diffraction, Spring, 2007.
164. Kurrey, R., et al., *Citrate-capped gold nanoparticles as a sensing probe for determination of cetyltrimethylammonium surfactant using FTIR spectroscopy and colorimetry.* Analytical and bioanalytical chemistry, 2019. **411**: p. 6943-6957.
165. Brusotti, G., et al., *Advances on size exclusion chromatography and applications on the analysis of protein biopharmaceuticals and protein aggregates: a mini review.* Chromatographia, 2018. **81**(1): p. 3-23.

166. Sidhom, K., P.O. Obi, and A. Saleem, *A review of exosomal isolation methods: is size exclusion chromatography the best option?* International Journal of Molecular Sciences, 2020. **21**(18): p. 6466.
167. Saunders, G. and H. Barth, *The state of the art and future trends of size-exclusion chromatography packings and columns.* 2012.
168. Hong, P., S. Koza, and E.S. Bouvier, *A review size-exclusion chromatography for the analysis of protein biotherapeutics and their aggregates.* Journal of liquid chromatography & related technologies, 2012. **35**(20): p. 2923-2950.
169. Engelhardt, H. and G. Ahr, *Optimization of efficiency in size-exclusion chromatography.* Journal of Chromatography A, 1983. **282**: p. 385-397.
170. Kopaciewicz, W. and F. Regnier, *Nonideal size-exclusion chromatography of proteins: effects of pH at low ionic strength.* Analytical biochemistry, 1982. **126**(1): p. 8-16.
171. Arakawa, T., et al., *The critical role of mobile phase composition in size exclusion chromatography of protein pharmaceuticals.* Journal of pharmaceutical sciences, 2010. **99**(4): p. 1674-1692.
172. Golovchenko, N.P., I.A. Kataeva, and V.K. Akimenko, *Analysis of pH-dependent protein interactions with gel filtration medium.* Journal of Chromatography A, 1992. **591**(1-2): p. 121-128.
173. Park, S., et al., *Fast size-exclusion chromatography at high temperature.* Journal of Chromatography A, 2007. **1157**(1-2): p. 96-100.
174. Popovici, S.T. and P.J. Schoenmakers, *Fast size-exclusion chromatography—theoretical and practical considerations.* Journal of Chromatography A, 2005. **1099**(1-2): p. 92-102.
175. Das, T. and S. Nema, *Protein particulate issues in biologics development.* American Pharmaceutical Review, 2008. **11**(4): p. 52.
176. Manning, R.R., et al., *Review of orthogonal methods to SEC for quantitation and characterization of protein aggregates.* BioPharm International, 2014. **27**(12).
177. Marassi, V., et al., *A new approach for the separation, characterization and testing of potential prionoid protein aggregates through hollow-fiber flow field-flow fractionation and multi-angle light scattering.* Analytica Chimica Acta, 2019. **1087**: p. 121-130.
178. Railean-Plugaru, V., et al., *Physicochemical study of natural fractionated biocolloid by asymmetric flow field-flow fractionation in tandem with various complementary techniques using biologically synthesized silver nanocomposites.* Analytical and bioanalytical chemistry, 2018. **410**: p. 2837-2847.
179. Lee, J., et al., *Synthesis and characterization of elution behavior of nonspherical gold nanoparticles in asymmetrical flow field-flow fractionation (AsFlFFF).* Journal of Nanoparticle Research, 2020. **22**: p. 1-12.
180. Loeschner, K., et al., *Optimization and evaluation of asymmetric flow field-flow fractionation of silver nanoparticles.* Journal of Chromatography A, 2013. **1272**: p. 116-125.
181. Amde, M., Z.-Q. Tan, and J. Liu, *Separation and size characterization of zinc oxide nanoparticles in environmental waters using asymmetrical flow field-flow fractionation.* Talanta, 2019. **200**: p. 357-365.
182. Roda, B., et al., *Flow field-flow fractionation and multi-angle light scattering as a powerful tool for the characterization and stability evaluation of drug-loaded metal–organic framework nanoparticles.* Analytical and bioanalytical chemistry, 2018. **410**: p. 5245-5253.

183. Gigault, J. and B. Grassl, *Improving the understanding of fullerene (nC60) aggregate structures: Fractal dimension characterization by static light scattering coupled to asymmetrical flow field flow fractionation.* Journal of colloid and interface science, 2017. **502**: p. 193-200.
184. Moquin, A., et al., *Quantum dot agglomerates in biological media and their characterization by asymmetrical flow field-flow fractionation.* European Journal of Pharmaceutics and Biopharmaceutics, 2015. **89**: p. 290-299.
185. Correia, M. and K. Loeschner, *Detection of nanoplastics in food by asymmetric flow field-flow fractionation coupled to multi-angle light scattering: possibilities, challenges and analytical limitations.* Analytical and bioanalytical chemistry, 2018. **410**: p. 5603-5615.
186. Gigault, J., et al., *Asymmetrical flow field flow fractionation methods to characterize submicron particles: application to carbon-based aggregates and nanoplastics.* Analytical and bioanalytical chemistry, 2017. **409**: p. 6761-6769.
187. Marassi, V., et al., *Synthesis Monitoring, Characterization and Cleanup of Ag-Polydopamine Nanoparticles Used as Antibacterial Agents with Field-Flow Fractionation.* Antibiotics, 2022. **11**(3): p. 358.
188. Pornwilard, M.-M. and A. Siripinyanond, *Field-flow fractionation with inductively coupled plasma mass spectrometry: past, present, and future.* Journal of Analytical Atomic Spectrometry, 2014. **29**(10): p. 1739-1752.
189. Loosli, F., et al., *Analysis of engineered nanomaterials (Ag, CeO2 and Fe2O3) in spiked surface waters at environmentally relevant particle concentrations.* Science of The Total Environment, 2020. **715**: p. 136927.
190. Barber, A., et al., *Coupling single particle ICP-MS with field-flow fractionation for characterizing metal nanoparticles contained in nanoplastic colloids.* Environmental Science: Nano, 2020. **7**(2): p. 514-524.
191. López-Sanz, S., et al., *Analytical strategy based on asymmetric flow field flow fractionation hyphenated to ICP-MS and complementary techniques to study gold nanoparticles transformations in cell culture medium.* Analytica chimica acta, 2019. **1053**: p. 178-185.
192. Bai, Q., et al., *Flow field-flow fractionation hyphenated with inductively coupled plasma mass spectrometry: A robust technique for characterization of engineered elemental metal nanoparticles in the environment.* Applied Spectroscopy Reviews, 2023. **58**(2): p. 110-131.
193. Bouzas-Ramos, D., et al., *Quantitative assessment of individual populations present in nanoparticle–antibody conjugate mixtures using AF4-ICP-MS/MS.* Analytical chemistry, 2019. **91**(5): p. 3567-3574.
194. Faucher, S., et al., *Characterization of polymer-coated CdSe/ZnS quantum dots and investigation of their behaviour in soil solution at relevant concentration by asymmetric flow field-flow fractionation–multi angle light scattering–inductively coupled plasma-mass spectrometry.* Analytica Chimica Acta, 2018. **1028**: p. 104-112.
195. Garcia-Cortes, M., et al., *Capping of Mn-doped ZnS quantum dots with DHLA for their stabilization in aqueous media: determination of the nanoparticle number concentration and surface ligand density.* Langmuir, 2017. **33**(25): p. 6333-6341.
196. Marassi, V., et al., *Silver nanoparticles as a medical device in healthcare settings: A five-step approach for candidate screening of coating agents.* Royal Society open science, 2018. **5**(1): p. 171113.

197. Sánchez-García, L., et al., *Size determination and quantification of engineered cerium oxide nanoparticles by flow field-flow fractionation coupled to inductively coupled plasma mass spectrometry.* Journal of Chromatography A, 2016. **1438**: p. 205-215.
198. Marassi, V., et al., *Hollow-fiber flow field-flow fractionation and multi-angle light scattering investigation of the size, shape and metal-release of silver nanoparticles in aqueous medium for nano-risk assessment.* Journal of pharmaceutical and biomedical analysis, 2015. **106**: p. 92-99.
199. Tan, Z.-Q., et al., *Tracking the transformation of nanoparticulate and ionic silver at environmentally relevant concentration levels by hollow fiber flow field-flow fractionation coupled to ICPMS.* Environmental Science & Technology, 2017. **51**(21): p. 12369-12376.
200. Tan, Z., et al., *Tracking the dissolution behavior of zinc oxide nanoparticles in skimmed milk powder solutions.* Food Chemistry, 2021. **365**: p. 130520.
201. Marassi, V., et al., *Native study of the behaviour of magnetite nanoparticles for hyperthermia treatment during the initial moments of intravenous administration.* Pharmaceutics, 2022. **14**(12): p. 2810.
202. Schadlich, A., et al., *Tumor accumulation of NIR fluorescent PEG–PLA nanoparticles: Impact of particle size and human xenograft tumor model.* ACS nano, 2011. **5**(11): p. 8710-8720.
203. Schädlich, A., et al., *How stealthy are PEG-PLA nanoparticles? An NIR in vivo study combined with detailed size measurements.* Pharmaceutical research, 2011. **28**: p. 1995-2007.
204. Lee, S., et al., *Study on elution behavior of poly (amidoamine) dendrimers and their interaction with bovine serum albumin in asymmetrical flow field-flow fractionation.* Analytical and bioanalytical chemistry, 2010. **396**: p. 1581-1588.
205. Boye, S., et al., *pH-triggered aggregate shape of different generations lysine-dendronized maleimide copolymers with maltose shell.* Biomacromolecules, 2012. **13**(12): p. 4222-4235.
206. Oh, J.K., et al., *The development of microgels/nanogels for drug delivery applications.* Progress in polymer science, 2008. **33**(4): p. 448-477.
207. Ekkelenkamp, A.E., et al., *Responsive crosslinked polymer nanogels for imaging and therapeutics delivery.* Journal of Materials Chemistry B, 2018. **6**(2): p. 210-235.
208. Smeets, N.M. and T. Hoare, *Designing responsive microgels for drug delivery applications.* Journal of Polymer Science Part A: Polymer Chemistry, 2013. **51**(14): p. 3027-3043.
209. Smith, M.H., et al., *Monitoring the erosion of hydrolytically-degradable nanogels via multiangle light scattering coupled to asymmetrical flow field-flow fractionation.* Analytical chemistry, 2010. **82**(2): p. 523-530.
210. Niezabitowska, E., et al., *Insights into the internal structures of nanogels using a versatile asymmetric-flow field-flow fractionation method.* Nanoscale Advances, 2020. **2**(10): p. 4713-4721.
211. Gaulding, J.C., A.B. South, and L.A. Lyon, *Hydrolytically degradable shells on thermoresponsive microgels.* Colloid and Polymer Science, 2013. **291**: p. 99-107.
212. Shimoda, A., et al., *Dual crosslinked hydrogel nanoparticles by nanogel bottom-up method for sustained-release delivery.* Colloids and Surfaces B: Biointerfaces, 2012. **99**: p. 38-44.
213. Chen, W., et al., *Cloaking mesoporous polydopamine with bacterial membrane vesicles to amplify local and systemic antitumor immunity.* ACS nano, 2023. **17**(8): p. 7733-7749.

214. Liu, L., et al., *Highly elastic and strain sensing corn protein electrospun fibers for monitoring of wound healing.* ACS nano, 2023. **17**(10): p. 9600-9610.
215. Xing, Y., et al., *Flower-like nanozyme with highly porous carbon matrix induces robust oxidative storm against drug-resistant cancer.* ACS nano, 2023. **17**(7): p. 6731-6744.
216. Mavridi-Printezi, A., et al., *Bio-applications of multifunctional melanin nanoparticles: from nanomedicine to nanocosmetics.* Nanomaterials, 2020. **10**(11): p. 2276.
217. Mavridi-Printezi, A., et al., *The Photophysics and Photochemistry of Melanin-Like Nanomaterials Depend on Morphology and Structure.* Chemistry–A European Journal, 2021. **27**(66): p. 16309-16319.
218. Ryu, J.H., P.B. Messersmith, and H. Lee, *Polydopamine surface chemistry: a decade of discovery.* ACS applied materials & interfaces, 2018. **10**(9): p. 7523-7540.
219. Hong, S., et al., *Non-covalent self-assembly and covalent polymerization co-contribute to polydopamine formation.* Advanced Functional Materials, 2012. **22**(22): p. 4711-4717.
220. Mavridi-Printezi, A., et al., *Reversible supramolecular noncovalent self-assembly determines the optical properties and the formation of melanin-like nanoparticles.* The Journal of Physical Chemistry Letters, 2022. **13**(42): p. 9829-9833.
221. Huang, Y., et al., *Mimicking melanosomes: polydopamine nanoparticles as artificial microparasols.* ACS central science, 2017. **3**(6): p. 564-569.
222. Xiao, M., et al., *Bio-inspired structural colors produced via self-assembly of synthetic melanin nanoparticles.* ACS nano, 2015. **9**(5): p. 5454-5460.
223. Cao, W., et al., *Unraveling the structure and function of melanin through synthesis.* Journal of the American Chemical Society, 2021. **143**(7): p. 2622-2637.
224. Battistella, C., et al., *Mimicking natural human hair pigmentation with synthetic melanin.* ACS Central Science, 2020. **6**(7): p. 1179-1188.
225. Delparastan, P., et al., *Direct evidence for the polymeric nature of polydopamine.* Angewandte Chemie, 2019. **131**(4): p. 1089-1094.
226. Mavridi-Printezi, A., et al., *Recent applications of melanin-like nanoparticles as antioxidant agents.* Antioxidants, 2023. **12**(4): p. 863.
227. Guo, Y., et al., *Hydrogen Atom Transfer from HOO. to ortho-Quinones Explains the Antioxidant Activity of Polydopamine.* Angewandte Chemie International Edition, 2021. **60**(28): p. 15220-15224.
228. Wang, L., C. Hu, and L. Shao, *The antimicrobial activity of nanoparticles: present situation and prospects for the future.* International journal of nanomedicine, 2017: p. 1227-1249.
229. Taglietti, A., et al., *Antibacterial activity of glutathione-coated silver nanoparticles against gram positive and gram negative bacteria.* Langmuir, 2012. **28**(21): p. 8140-8148.
230. Boudreau, M.D., et al., *Differential effects of silver nanoparticles and silver ions on tissue accumulation, distribution, and toxicity in the Sprague Dawley rat following daily oral gavage administration for 13 weeks.* Toxicological Sciences, 2016. **150**(1): p. 131-160.
231. Lok, C.-N., et al., *Silver nanoparticles: partial oxidation and antibacterial activities.* JBIC Journal of Biological Inorganic Chemistry, 2007. **12**: p. 527-534.
232. Ivask, A., et al., *Size-dependent toxicity of silver nanoparticles to bacteria, yeast, algae, crustaceans and mammalian cells in vitro.* PloS one, 2014. **9**(7): p. e102108.
233. Kubo, A.-L., et al., *Antimicrobial potency of differently coated 10 and 50 nm silver nanoparticles against clinically relevant bacteria Escherichia coli and Staphylococcus aureus.* Colloids and Surfaces B: Biointerfaces, 2018. **170**: p. 401-410.

234. Li, W.-R., et al., *Antibacterial effect of silver nanoparticles on Staphylococcus aureus.* Biometals, 2011. **24**: p. 135-141.
235. Saravanan, M., et al., *Synthesis of silver nanoparticles from Bacillus brevis (NCIM 2533) and their antibacterial activity against pathogenic bacteria.* Microbial pathogenesis, 2018. **116**: p. 221-226.
236. Nakamura, S., et al., *Synthesis and application of silver nanoparticles (Ag NPs) for the prevention of infection in healthcare workers.* International journal of molecular sciences, 2019. **20**(15): p. 3620.
237. Deng, H., et al., *Mechanistic study of the synergistic antibacterial activity of combined silver nanoparticles and common antibiotics.* Environmental science & technology, 2016. **50**(16): p. 8840-8848.
238. Patra, J.K. and K.-H. Baek, *Antibacterial activity and synergistic antibacterial potential of biosynthesized silver nanoparticles against foodborne pathogenic bacteria along with its anticandidal and antioxidant effects.* Frontiers in microbiology, 2017. **8**: p. 167.
239. Niyonshuti, I.I., et al., *Polydopamine surface coating synergizes the antimicrobial activity of silver nanoparticles.* ACS applied materials & interfaces, 2020. **12**(36): p. 40067-40077.
240. Guo, A., et al., *Mussel-inspired green synthesis of Ag-coated polydopamine microspheres for selective antibacterial performance.* Micro & Nano Letters, 2019. **14**(4): p. 394-398.
241. Luo, H., et al., *Facile synthesis of novel size-controlled antibacterial hybrid spheres using silver nanoparticles loaded with poly-dopamine spheres.* Rsc Advances, 2015. **5**(18): p. 13470-13477.
242. Liu, Z. and Y. Hu, *Sustainable antibiofouling properties of thin film composite forward osmosis membrane with rechargeable silver nanoparticles loading.* ACS applied materials & interfaces, 2016. **8**(33): p. 21666-21673.
243. Yang, Z., et al., *In situ reduction of silver by polydopamine: A novel antimicrobial modification of a thin-film composite polyamide membrane.* Environmental science & technology, 2016. **50**(17): p. 9543-9550.
244. Tang, L., K.J. Livi, and K.L. Chen, *Polysulfone membranes modified with bioinspired polydopamine and silver nanoparticles formed in situ to mitigate biofouling.* Environmental Science & Technology Letters, 2015. **2**(3): p. 59-65.
245. Neethu, S., et al., *Surface functionalization of central venous catheter with mycofabricated silver nanoparticles and its antibiofilm activity on multidrug resistant Acinetobacter baumannii.* Microbial pathogenesis, 2020. **138**: p. 103832.
246. Gao, C., et al., *Antibacterial activity and osseointegration of silver-coated poly (ether ether ketone) prepared using the polydopamine-assisted deposition technique.* Journal of Materials Chemistry B, 2017. **5**(47): p. 9326-9336.
247. Singh, I., et al., *Recent advances in a polydopamine-mediated antimicrobial adhesion system.* Frontiers in microbiology, 2021. **11**: p. 607099.
248. Yu, X., G. Cheng, and S.-Y. Zheng, *Synthesis of self-assembled multifunctional nanocomposite catalysts with highly stabilized reactivity and magnetic recyclability.* Scientific reports, 2016. **6**(1): p. 25459.
249. Martínez-Castañon, G.-A., et al., *Synthesis and antibacterial activity of silver nanoparticles with different sizes.* Journal of nanoparticle research, 2008. **10**: p. 1343-1348.
250. Verma, P. and S.K. Maheshwari, *Preparation of sliver and selenium nanoparticles and its characterization by dynamic light scattering and scanning electron microscopy.* Journal of microscopy and ultrastructure, 2018. **6**(4): p. 182-187.

251. Carvalho, P.M., et al., *Application of light scattering techniques to nanoparticle characterization and development.* Frontiers in chemistry, 2018. **6**: p. 237.
252. Boughbina-Portolés, A., et al., *Study of the stability of citrate capped agnps in several environmental water matrices by asymmetrical flow field flow fractionation.* Nanomaterials, 2021. **11**(4): p. 926.
253. Taboada-López, M.V., et al., *AF4-UV-ICP-MS for detection and quantification of silver nanoparticles in seafood after enzymatic hydrolysis.* Talanta, 2021. **232**: p. 122504.
254. Ricardo, A.I.C., et al., *Rapid assessment of silver nanoparticle migration from food containers into food simulants using a qualitative method.* Food Chemistry, 2021. **361**: p. 130091.
255. Thota, R. and V. Ganesh, *Simple and facile preparation of silver–polydopamine (Ag–PDA) core–shell nanoparticles for selective electrochemical detection of cysteine.* Rsc Advances, 2016. **6**(55): p. 49578-49587.
256. Wang, X., et al., *Effects of Polydopamine Microspheres Loaded with Silver Nanoparticles on Lolium multiflorum: Bigger Size, Less Toxic.* Toxics, 2021. **9**(7): p. 151.
257. Jiang, X., Y. Wang, and M. Li, *Selecting water-alcohol mixed solvent for synthesis of polydopamine nano-spheres using solubility parameter. Sci Rep 4: 6070*. 2014.
258. Ma, Y., et al., *One-step synthesis of silver/dopamine nanoparticles and visual detection of melamine in raw milk.* Analyst, 2011. **136**(20): p. 4192-4196.
259. Boanini, E., et al., *A new multifunctionalized material against multi-drug resistant bacteria and abnormal osteoclast activity.* European Journal of Pharmaceutics and Biopharmaceutics, 2018. **127**: p. 120-129.
260. Reschiglian, P., et al., *On-line hollow-fiber flow field-flow fractionation-electrospray ionization/time-of-flight mass spectrometry of intact proteins.* Analytical chemistry, 2005. **77**(1): p. 47-56.
261. Dou, H., et al., *Study on steric transition in asymmetrical flow field-flow fractionation and application to characterization of high-energy material.* Journal of Chromatography A, 2013. **1304**: p. 211-219.
262. Some, D. and C. Johann, *Characterization of Nanopharmaceuticals with Field-Flow Fractionation and Light Scattering (FFF-MALS-DLS).* Wyatt Technology: Santa Barbara, CA, USA, 2021.
263. Wang, F., et al., *Construction of polydopamine/silver nanoparticles multilayer film for hydrogen peroxide detection.* Journal of Electroanalytical Chemistry, 2013. **706**: p. 102-107.
264. Gevorgyan, S., R. Schubert, and M. Yeranosyan, *Antibacterial activity of royal jelly-mediated green synthesized silver nanoparticles. AMB Express 11: 51*. 2021.
265. Maldonado-Camargo, L., M. Unni, and C. Rinaldi, *Magnetic characterization of iron oxide nanoparticles for biomedical applications.* Biomedical Nanotechnology: Methods and Protocols, 2017: p. 47-71.
266. Shubayev, V.I., T.R. Pisanic II, and S. Jin, *Magnetic nanoparticles for theragnostics.* Advanced drug delivery reviews, 2009. **61**(6): p. 467-477.
267. Wankhede, M., et al., *Magnetic nanoparticles: an emerging technology for malignant brain tumor imaging and therapy.* Expert review of clinical pharmacology, 2012. **5**(2): p. 173-186.
268. Lin, Y., et al., *Magnetic nanoparticles applied in targeted therapy and magnetic resonance imaging: crucial preparation parameters, indispensable pre-treatments, updated research*

advancements and future perspectives. Journal of Materials Chemistry B, 2020. **8**(28): p. 5973-5991.
269. Laurent, S., et al., *Magnetic fluid hyperthermia: focus on superparamagnetic iron oxide nanoparticles.* Advances in colloid and interface science, 2011. **166**(1-2): p. 8-23.
270. Wong, R.S., *Apoptosis in cancer: from pathogenesis to treatment.* Journal of experimental & clinical cancer research, 2011. **30**: p. 1-14.
271. Samanta, B., et al., *Protein-passivated Fe 3 O 4 nanoparticles: low toxicity and rapid heating for thermal therapy.* Journal of materials chemistry, 2008. **18**(11): p. 1204-1208.
272. Patsula, V., et al., *Synthesis and modification of uniform PEG-neridronate-modified magnetic nanoparticles determines prolonged blood circulation and biodistribution in a mouse preclinical model.* Scientific reports, 2019. **9**(1): p. 10765.
273. Mosafer, J. and M. Teymouri, *Comparative study of superparamagnetic iron oxide/doxorubicin co-loaded poly (lactic-co-glycolic acid) nanospheres prepared by different emulsion solvent evaporation methods.* Artificial cells, nanomedicine, and biotechnology, 2018. **46**(6): p. 1146-1155.
274. Cox, A., et al., *Evolution of nanoparticle protein corona across the blood–brain barrier.* ACS nano, 2018. **12**(7): p. 7292-7300.
275. Marassi, V., et al., *FFF-based high-throughput sequence shortlisting to support the development of aptamer-based analytical strategies.* Analytical and Bioanalytical Chemistry, 2022. **414**(18): p. 5519-5527.
276. Hayashi, K., et al., *Facile synthesis, characterization of various polymer immobilized on magnetite nanoparticles applying the coprecipitation method.* Journal of Applied Polymer Science, 2022. **139**(5): p. 51581.
277. Mylkie, K., et al., *Polymer-coated magnetite nanoparticles for protein immobilization.* Materials, 2021. **14**(2): p. 248.
278. Anbarasu, M., et al., *Synthesis and characterization of polyethylene glycol (PEG) coated Fe3O4 nanoparticles by chemical co-precipitation method for biomedical applications.* Spectrochimica Acta Part A: Molecular and Biomolecular Spectroscopy, 2015. **135**: p. 536-539.
279. Sah, H., et al., *Concepts and practices used to develop functional PLGA-based nanoparticulate systems.* International journal of nanomedicine, 2013: p. 747-765.
280. Danhier, F., et al., *PLGA-based nanoparticles: an overview of biomedical applications.* Journal of controlled release, 2012. **161**(2): p. 505-522.
281. Tombácz, E., et al., *Adsorption of organic acids on magnetite nanoparticles, pH-dependent colloidal stability and salt tolerance.* Colloids and Surfaces A: Physicochemical and Engineering Aspects, 2013. **435**: p. 91-96.
282. Han, M., et al., *Amyloid protein-biofunctionalized polydopamine nanoparticles demonstrate minimal plasma protein fouling and efficient photothermal therapy.* ACS Applied Materials & Interfaces, 2022. **14**(11): p. 13743-13757.
283. Wang, X. and W. Zhang, *The Janus of Protein Corona on nanoparticles for tumor targeting, immunotherapy and diagnosis.* Journal of Controlled Release, 2022. **345**: p. 832-850.
284. Bychkova, A., et al., *Interaction between blood plasma proteins and magnetite nanoparticles.* Colloid journal, 2010. **72**: p. 696-702.
285. Dell'Orco, D., et al., *Modeling the time evolution of the nanoparticle-protein corona in a body fluid.* PloS one, 2010. **5**(6): p. e10949.

286. Xiao, Q., et al., *The effects of protein corona on in vivo fate of nanocarriers.* Advanced Drug Delivery Reviews, 2022. **186**: p. 114356.
287. Mourdikoudis, S., R.M. Pallares, and N.T. Thanh, *Characterization techniques for nanoparticles: comparison and complementarity upon studying nanoparticle properties.* Nanoscale, 2018. **10**(27): p. 12871-12934.
288. Reschiglian, P., D.C. Rambaldi, and A. Zattoni, *Flow field-flow fractionation with multiangle light scattering detection for the analysis and characterization of functional nanoparticles.* Analytical and bioanalytical chemistry, 2011. **399**(1): p. 197-203.
289. Ventouri, I.K., et al., *Field-flow fractionation for molecular-interaction studies of labile and complex systems: A critical review.* Analytica chimica acta, 2022. **1193**: p. 339396.
290. Thielking, H. and W.M. Kulicke, *Determination of the structural parameters of aqueous polymer solutions in the molecular, partially aggregated, and particulate states by means of FFFF/MALLS.* Journal of Microcolumn Separations, 1998. **10**(1): p. 51-56.
291. D'Elios, M.M., et al., *Myelin-specific T cells carry and release magnetite PGLA–PEG COOH nanoparticles in the mouse central nervous system.* RSC advances, 2018. **8**(2): p. 904-913.
292. Marassi, V., et al., *Hollow-fiber flow field-flow fractionation and multi-angle light scattering as a new analytical solution for quality control in pharmaceutical nanotechnology*. Microchemical Journal, 2018. **136**: p. 149-156.
293. Wassel, R.A., et al., *Dispersion of super paramagnetic iron oxide nanoparticles in poly (d, l-lactide-co-glycolide) microparticles.* Colloids and Surfaces A: Physicochemical and Engineering Aspects, 2007. **292**(2-3): p. 125-130.
294. Liu, X., et al., *Synthesis and characterization of highly-magnetic biodegradable poly (d, l-lactide-co-glycolide) nanospheres.* Journal of Controlled Release, 2007. **119**(1): p. 52-58.
295. Ortelli, S., et al., *TiO2@ BSA nano-composites investigated through orthogonal multi-techniques characterization platform.* Colloids and Surfaces B: Biointerfaces, 2021. **207**: p. 112037.
296. Marassi, V., et al., *An ultracentrifugation–hollow-fiber flow field-flow fractionation orthogonal approach for the purification and mapping of extracellular vesicle subtypes.* Journal of Chromatography A, 2021. **1638**: p. 461861.
297. Marassi, V., et al., *Tracking heme-protein interactions in healthy and pathological human serum in native conditions by miniaturized FFF-multidetection.* Applied Sciences, 2022. **12**(13): p. 6762.
298. Kennedy, D., et al., *Human serum albumin stabilizes aqueous silver nanoparticle suspensions and inhibits particle uptake by cells.* Environmental Science: Nano, 2018. **5**(4): p. 863-867.
299. Free, P., C.P. Shaw, and R. Lévy, *PEGylation modulates the interfacial kinetics of proteases on peptide-capped gold nanoparticles.* Chemical communications, 2009(33): p. 5009-5011.
300. Boulos, S.P., et al., *Nanoparticle–protein interactions: a thermodynamic and kinetic study of the adsorption of bovine serum albumin to gold nanoparticle surfaces.* Langmuir, 2013. **29**(48): p. 14984-14996.
301. Nicoară, R., et al., *Quantification of the PEGylated gold nanoparticles protein corona. Influence on nanoparticle size and surface chemistry.* Applied Sciences, 2019. **9**(22): p. 4789.

302. Nosrati, H., et al., *Bovine Serum Albumin (BSA) coated iron oxide magnetic nanoparticles as biocompatible carriers for curcumin-anticancer drug.* Bioorganic chemistry, 2018. **76**: p. 501-509.
303. Choi, J., et al., *Separation and zeta-potential determination of proteins and their oligomers using electrical asymmetrical flow field-flow fractionation (EAF4).* Journal of Chromatography A, 2020. **1633**: p. 461625.
304. Cabri, W., et al., *Therapeutic peptides targeting PPI in clinical development: Overview, mechanism of action and perspectives.* Frontiers in Molecular Biosciences, 2021. **8**: p. 697586.
305. Craik, D.J., et al., *The future of peptide-based drugs.* Chemical biology & drug design, 2013. **81**(1): p. 136-147.
306. Al Shaer, D., et al., *2021 FDA TIDES (peptides and oligonucleotides) harvest.* Pharmaceuticals, 2022. **15**(2): p. 222.
307. Herrero, E.P., M.J. Alonso, and N. Csaba, *Polymer-based oral peptide nanomedicines.* Therapeutic delivery, 2012. **3**(5): p. 657-668.
308. Sharma, P., S. Bansal, and A. Banik, *Noninvasive routes of proteins and peptides drug delivery.* Indian journal of pharmaceutical sciences, 2011. **73**(4): p. 367.
309. Tiwari, M.K., et al., *Computational approaches for rational design of proteins with novel functionalities.* Computational and structural biotechnology journal, 2012. **2**(3): p. e201204002.
310. Mrsny, R.J., *Strategies for targeting protein therapeutics to selected tissues and cells.* Expert Opinion on Biological Therapy, 2004. **4**(1): p. 65-73.
311. Walsh, C.T., R.V. O'Brien, and C. Khosla, *Nonproteinogenic amino acid building blocks for nonribosomal peptide and hybrid polyketide scaffolds.* Angewandte Chemie International Edition, 2013. **52**(28): p. 7098-7124.
312. Ferrazzano, L., et al., *Sustainability in peptide chemistry: current synthesis and purification technologies and future challenges.* Green Chemistry, 2022. **24**(3): p. 975-1020.
313. De Luca, C., et al., *Downstream processing of therapeutic peptides by means of preparative liquid chromatography.* Molecules, 2021. **26**(15): p. 4688.
314. Patel, P., *Preformulation studies: an integral part of formulation design.* Pharmaceutical Formulation Design-Recent Practices, 2019. **9**.
315. Vilegave, K., G. Vidyasagar, and P. Chandankar, *Preformulation studies of pharmaceutical new drug molecule and products: An Overview.* The American Journal of Pharmacy, 2013. **1**(3): p. 1-20.
316. Chi, E.Y., et al., *Physical stability of proteins in aqueous solution: mechanism and driving forces in nonnative protein aggregation.* Pharmaceutical research, 2003. **20**: p. 1325-1336.
317. Akash, M.S.H., et al., *Development of therapeutic proteins: advances and challenges.* Turkish Journal of Biology, 2015. **39**(3): p. 343-358.
318. Chincholkar, A., D. Khobragade, and S. Pathak, *US FDA Regulatory Framework for Generic Peptides Referring to rDNA Origin Reference Products.* Journal of Pharmaceutical Research International, 2022. **34**(41A): p. 44-49.
319. Wang, W., *Protein aggregation and its inhibition in biopharmaceutics.* International journal of pharmaceutics, 2005. **289**(1-2): p. 1-30.
320. Mahler, H.-C., et al., *Protein aggregation: pathways, induction factors and analysis.* Journal of pharmaceutical sciences, 2009. **98**(9): p. 2909-2934.

321. Carpenter, J.F., et al., *Potential inaccurate quantitation and sizing of protein aggregates by size exclusion chromatography: essential need to use orthogonal methods to assure the quality of therapeutic protein products.* Journal of pharmaceutical sciences, 2010. **99**(5): p. 2200-2208.
322. Ladenheim, E.E., *Liraglutide and obesity: a review of the data so far.* Drug design, development and therapy, 2015: p. 1867-1875.
323. Pabreja, K., et al., *Molecular mechanisms underlying physiological and receptor pleiotropic effects mediated by GLP-1R activation.* British Journal of Pharmacology, 2014. **171**(5): p. 1114-1128.
324. Wang, Y., et al., *Transformation of oligomers of lipidated peptide induced by change in pH.* Molecular pharmaceutics, 2015. **12**(2): p. 411-419.
325. Zapadka, K.L., et al., *A pH-induced switch in human glucagon-like peptide-1 aggregation kinetics.* Journal of the American Chemical Society, 2016. **138**(50): p. 16259-16265.
326. Trier, S., et al., *Acylation of Glucagon-like peptide-2: interaction with lipid membranes and in vitro intestinal permeability.* PLoS One, 2014. **9**(10): p. e109939.
327. Steensgaard, D.B., et al. *The molecular basis for the delayed absorption of the once-daily human GLP-1 analoge, liraglutide*. in *Diabetes*. 2008. AMER DIABETES ASSOC 1701 N BEAUREGARD ST, ALEXANDRIA, VA 22311-1717 USA.
328. Guryanov, I., et al., *Innovative chemical synthesis and conformational hints on the lipopeptide liraglutide.* Journal of peptide Science, 2016. **22**(7): p. 471-479.
329. Frederiksen, T.M., et al., *Oligomerization of a glucagon-like peptide 1 analog: bridging experiment and simulations.* Biophysical journal, 2015. **109**(6): p. 1202-1213.
330. Mildner, R., et al., *Improved multidetector asymmetrical-flow field-flow fractionation method for particle sizing and concentration measurements of lipid-based nanocarriers for RNA delivery.* European Journal of Pharmaceutics and Biopharmaceutics, 2021. **163**: p. 252-265.
331. ISO, I., *TS 21362: 2018 Nanotechnologies—Analysis of nano-objects using asymmetrical-flow and centrifugal field-flow fractionation.* International Organization for Standardization, Geneva, Switzerland, 2018.
332. Marassi, V., et al., *Perspectives on protein biopolymers: miniaturized flow field-flow fractionation-assisted characterization of a single-cysteine mutated phaseolin expressed in transplastomic tobacco plants.* Journal of Chromatography A, 2021. **1637**: p. 461806.
333. Striegel, A.M. and P. Sinha, *Absolute molar mass determination in mixed solvents. 1. Solving for the SEC/MALS/DRI "trivial" case.* Analytica chimica acta, 2019. **1053**: p. 186-195.
334. Ventouri, I.K., et al., *Characterizing Non-covalent Protein Complexes Using Asymmetrical Flow Field-Flow Fractionation On-Line Coupled to Native Mass Spectrometry.* Analytical chemistry, 2023. **95**(19): p. 7487-7494.

Acknowledgements

First and foremost, I would like to express my deepest gratitude to my supervisor, Prof. Pierluigi Reschiglian, and my co-supervisor, Dr. Valentina Marassi, for their mentorship, dedication, and support. Their guidance has been instrumental in navigating the complexities of my project and elevating the quality of my work. I am equally grateful to Professors Andrea Zattoni and Barbara Roda, whose invaluable assistance helped me to achieve the goals of my PhD project. I extend my sincere thanks to all our collaborators who provided essential technical support. Special thanks also go to byFlow Srl., for making me use their instrumentation and introducing me to a new and stimulating working environment, and to Marco Polo funding. This financial support allowed me to spend 3 months at the Raman & SEM group at the Institute of Water Chemistry, Technical University of Munich (TUM). This made me find excellent mentorship and a very stimulating, international environment. Finally, I would like to thank my family for their endless love and support throughout this journey.